

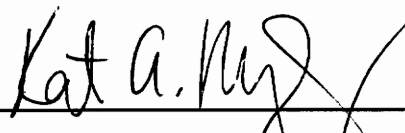
A Dual Wavelength Fiber Optic Strain Sensing System

by


Asif Malik

Thesis submitted to the Faculty of the
Virginia Polytechnic Institute and State University
in partial fulfillment of the requirements for the degree of
MASTER OF SCIENCE
in
Electrical Engineering

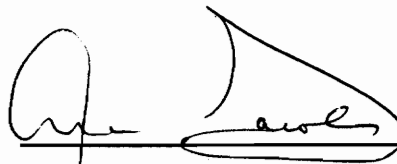
APPROVED:



Kent A. Murphy, Chairman



Richard O. Claus



Ira Jacobs

April, 1996
Blacksburg, Virginia

Keywords: Fiber Optic Sensors, Interferometer, Signal Reconstruction

LD
5655
V855
1996
M355
c.2

A Dual Wavelength Fiber Optic Strain Sensing System

by

Asif Malik

Kent A. Murphy, Chairman

Electrical Engineering

Abstract

The extrinsic Fabry-Perot interferometer (EFPI) has been extensively used as a strain sensor in various applications. However, like other interferometric sensors, the EFPI suffers from ambiguity in detecting directional changes of the applied perturbation, when the operating point is at a maxima or a minima on the transfer function curve. Different methods, or sensor configurations have been proposed to solve this problem. This thesis investigates the use of dual wavelength interferometry to overcome this limitation.

Possible systems configurations based on dual wavelength interferometry were considered, and the comprehensive design and implementation of a dual laser time division multiplexed (TDM) system based is presented. The system operates by alternately pulse modulating two laser diodes, which are closely spaced in center wavelength. Although the strain rate measurement capability of the system is dependent primarily on the speed of its hardware and the accuracy of its software, it is shown that it can be considerably enhanced by employing digital signal processing techniques.

Acknowledgments

I would like to thank Dr. Kent A. Murphy for his constant encouragement, guidance, but most of all, for his unwavering friendship over the past three years. He has been truly instrumental in my academic and personal development during my stay at Virginia Tech. I am extremely grateful to Dr. Richard O. Claus for giving me the opportunity to work at the Fiber & Electro-Optics Research Center and for serving on my committee. I would like to express my gratitude to Dr. Ira Jacobs for all his advice, and for going through the pain of reviewing this thesis while recuperating from surgery at the hospital.

I am greatly indebted to Vikram Bhatia and Mark Jones for their help through every step of this research. Moreover, the two of you have been true friends, and I thank you for that. I would like to acknowledge Paul Duncan and Shah Musa for their support in writing the acquisition software.

I thank the students and staff of FEORC for making it such a great place to work, study, and have fun. Special thanks to Rajat Dhawan, Dave Forbis, Jennifer Grace, Mike Gunther, Anjana Nagarajan, Mallika Sen, Nirmal Velayudhan, and Veeru Vuppala for their friendship.

Finally, and most importantly, I am grateful to my parents, Fatima and Malik, my sister, Priyani, and my uncle, Ghazi, who have unselfishly sacrificed throughout their lives so that I can achieve my dreams. Thank you for all your love and support.

Table of Contents

Title Page	<i>i</i>
Abstract	<i>ii</i>
Acknowledgments	<i>iii</i>
Table of Contents	<i>iv</i>
List of Illustrations	<i>vi</i>
Chapter 1 - Introduction	1
1.1 Classification of Fiber Optic Sensors	1
1.1.1 Intensity Based Sensors	1
1.1.2 Interferometric Sensors	3
1.1.2.1 Mach-Zender Interferometer	4
1.1.2.2 Michelson Interferometer	6
1.1.2.3 Fabry-Perot Interferometer	8
1.2 Thesis Statement and Overview	8
Chapter 2 - Extrinsic Fabry-Perot Interferometer	10
2.1 Theory and Fabrication	10
2.2 Advantages of the EFPI	15
2.3 Limitations of the EFPI	16
2.4 Existing EFPI Based Sensor Systems	18
2.4.1 Quadrature Phase Shifted EFPIs	18
2.4.2 Absolute EFPIs	18
2.4.2.1 Constant Wavelength Technique	20
2.4.2.2 Constant Phase Technique	20
Chapter 3 - Dual Wavelength Extrinsic Fabry Perot Interferometer	22
3.1 Theory and Motivation	22
3.2 Determining Dynamic Range	25
3.3 Possible System Topologies	26
3.3.1 Dual Laser CW System	26
Table of Contents	<i>iv</i>

3.3.2 Dual Laser TDM System	29
3.3.3 Single Laser TDM System	29
3.3.4 Choosing System Topology	30
3.4 System Component Design	32
3.4.1 Transmitter	32
3.4.2 Receiver	37
3.4.3 Data Acquisition	41
Chapter 4 - Derivation of System Parameters	44
4.1 Power Budget	44
4.2 Noise Mechanisms in the System	47
4.2.1 Transmitter Noise	47
4.2.1.1 Intensity Noise	47
4.2.2 Receiver Noise	48
4.2.2.1 Shot Noise	48
4.2.2.2 Thermal Noise	49
4.2.3 SNR at the Detector	50
4.2.4 Quantization Noise	50
4.2.5 Overall SNR	51
4.3 Determining Strain Range	51
4.3.1 Effect of Laser Wavelength Instability on Strain Range	52
4.4 Determining Strain Rate and Resolution	52
4.4.1 Signal Reconstruction by Plotting DAQ Samples	53
4.4.2 Signal Reconstruction Through Interpolation	54
4.4.2.1 Filter Design and Practical Considerations	59
Chapter 5 - Experimental Setup, Results and Discussion	69
Chapter 6 - Conclusions and Future Directions	80
References	81
Vita	84

List of Illustrations

Chapter 1 - Introduction	1-9
Figure 1.1: A typical configuration of an intensity sensor	2
Figure 1.2: Experimental variation of the ratio R with gap length d	2
Figure 1.3: A fiber Mach-Zender interferometer	5
Figure 1.4: Intensity versus phase difference for a Mach-Zender Interferometer.....	5
Figure 1.5: Configuration of a fiber Michelson Interferometer	7
Figure 1.6: Intrinsic Fabry-Perot Interferometer (IFPI)	7
Chapter 2 - Extrinsic Fabry-Perot Interferometer	10-21
Figure 2.1: The Extrinsic Fabry-Perot Interferometer (EFPI) with details of the sensor system	11
Figure 2.2: Fabry-Perot cavity with multiple reflections	13
Figure 2.3: Fabry-Perot transfer functions.....	13
Figure 2.4: Variation of EFPI output intensity with increasing gap length	14
Figure 2.5: Sensitivity variation of an EFPI along its transfer function curve	14
Figure 2.6: (a) Example of distinct EFPI turn around point (b) Example of ambiguous EFPI output	17
Figure 2.7: Two proposed configurations of quadrature phase-shifted EFPIs	19
Figure 2.8: Setup for the absolute EFPI (AEFPI) system	19
Chapter 3 - Dual Wavelength Extrinsic Fabry-Perot Interferometer	22-43
Figure 3.1: Interferometric output response with dual wavelength operation	24
Figure 3.2: Lead-lag relationship between EFPI output waveforms	24

Figure 3.3: Block diagram of dual laser CW topology	27
Figure 3.4: Block diagram of dual laser TDM topology	27
Figure 3.5: Configuration of single laser TDM topology	28
Figure 3.6: Optical emission spectrum of Mitsubishi 7781A LD. (a) and (b) are the spectrum of the LD for the same drive current at two different time instants	31
Figure 3.7: Optical emission spectrum of Mitsubishi 7011R LDs at a drive current of 20 mA. (a) LD whose peak wavelength is at 1291.93 nm (b) LD whose peak wavelength is at 1294.65 nm	33
Figure 3.8: Schematics of the transmitters designed for the dual laser TDM system. (a) transmitter that is in phase with the clock (b) transmitter that is out of phase with the clock	35
Figure 3.9: Oscilloscope traces of the output wave forms of the transmitters monitored across a 47Ω load, at a switching speed of 100 kHz. (a) and (b) are respectively the outputs for in phase and out of phase transmitters relative to the input clock	36
Figure 3.10: Illustration of analog-to-PAM conversion for a duty cycle of $d = 1/3$	38
Figure 3.11: Schematic of the designed two stage receiver circuit	39
Figure 3.12: Oscilloscope traces of the PAM waveforms at the detector at a switching speed of 100 Hz. (a) detected signal when LD that has a peak wavelength of 1291.93 is on (b) detector output when LD with peak wavelength at 1294 is being operated	42

Chapter 4 - Derivation of System Parameters 44-68

Figure 4.1: Power output versus forward current for Mitsubishi 7011R LDs. (a) LD with peak wavelength at 1291.93 nm (b) LD with peak wavelength at 1294.65 nm	45
Figure 4.2: An interpolation system to increase sampling rate by L	56
Figure 4.3: Time domain illustration of interpolation. (a), (b), and (c) represent the input sequence $x[n]$, the expander output $x_e[n]$, and the desired output $x_i[n]$ respectively	57

Figure 4.4: Frequency domain illustration of interpolation	58
Figure 4.5: Frequency response of a typical low pass filter	61
Figure 4.6: Oversampled signal with sinusoidal components of 100 Hz and 150 Hz	61
Figure 4.7: Discrete-time waveform of signal sampled at 400 sps	63
Figure 4.8: Reconstructed waveform of signal using an interpolation factor of 6	63
Figure 4.9: Frequency response of low pass filter used in interpolation example	64

Chapter 5 - Experimental Setup, Results and Discussion 69-79

Figure 5.1: Experimental setup for dual wavelength EFPI sensing system	70
Figure 5.2: Raw sensor output with source at 1294.6 nm displaying distinct turn around point while source at 1291.9 nm showing ambiguity	71
Figure 5.3: Raw sensor output with source at 1291.9 nm displaying distinct turn around point while source at 1291.6 nm showing ambiguity	71
Figure 5.4: Raw sensor output with both sources displaying distinct turn around point	72
Figure 5.5: Filtered sensor output with source at 1294.6 nm displaying distinct turn around point while source at 1291.9 nm showing ambiguity	72
Figure 5.6: Filtered sensor output with source at 1294.9 nm displaying distinct turn around point while source at 1291.6 nm showing ambiguity	73
Figure 5.7: Raw sensor output with both sources displaying distinct turn around point	73
Figure 5.8: Frequency response of low pass filter used to filter the raw sensor output	74
Figure 5.9: Schematic of the beam-motor mechanism	74
Figure 5.10: Filtered sensor output for the 1291.9 nm source in response to the applied sinusoidal strain function. The data acquisition rate is 2500 sps	75
Figure 5.11: Spectrum of the sensor output signal for the 1291.9 nm source	75
Figure 5.12: Sensor output for the 1291.9 nm source in response to the applied sinusoidal strain function. The data acquisition rate is 140 sps	77

Figure 5.13: Reconstructed sensor output using interpolation with $L = 8$ for 1291.9 nm source. Actual data acquisition rate is 140 sps	77
Figure 5.14: Frequency response of low pass filter used for interpolation	78
Figure 5.15: Filtered sensor output for the 1291.9 nm source in response to the applied sinusoidal strain function. Data acquisition rate is 833 sps	79

Chapter 1 - Introduction

The advances in fiber optic technology, driven largely by the telecommunications industry, in combination with low cost opto-electronic components and improvements in optical signal processing, have made fiber optic sensors very attractive for many industrial and commercial applications. As a result, recently these sensors have found increased use in such areas as aerospace, defense, manufacturing, medicine, and civil structures. Optical fibers offer numerous advantages over conventional sensors. Optical fibers are passive, small, light weight, and immune to electromagnetic interference (EMI). They offer better resolution, larger bandwidth, and increased sensitivity over existing sensing techniques. They are also environmentally rugged and have a large dynamic range of measurements [1]. Strain, displacement, temperature, pressure, vibration, damage, and current are among the different parameters that can be measured using fiber optic sensors [2].

1.1 Classification of Fiber Optic Sensors

Fiber optic sensors can be classified on the basis of location of sensing region (inside or outside the fiber), or principle of operation. On the basis of location of sensing region, optical fiber sensors can be classified either as "extrinsic" or "intrinsic". In an "extrinsic" sensor, light is guided to the point where the sensing takes place. The light then exits the fiber and is modulated in a separate zone. It is then relaunched into either the same or different fiber. In an "intrinsic" sensor, light is modulated by the measurand within the fiber itself [2]. Based on operating principle, fiber optic sensors can be divided into either intensity or interferometric sensors. These are discussed in more detail in the next section.

1.1.1 Intensity Based Sensors

Intensity based sensors are simple to construct, and require only a modest amount of support electronics and signal processing. Multimode fibers are usually used to construct intensity based sensors since light can be easily coupled into these fibers. A typical intensity based sensor is shown in Figure 1.1. It consists of an LED, a 2X2 coupler, an air-gap (comprising the fiber in one arm of the coupler and another multimode fiber inside a hollow core tube), and two photodetectors. Light travels along the coupler arm comprising the sensor head and illuminates the air-gap. The effects of an external perturbation modulate the air-gap. The intensity of the light reflected by the second fiber, I_{ref} , is then

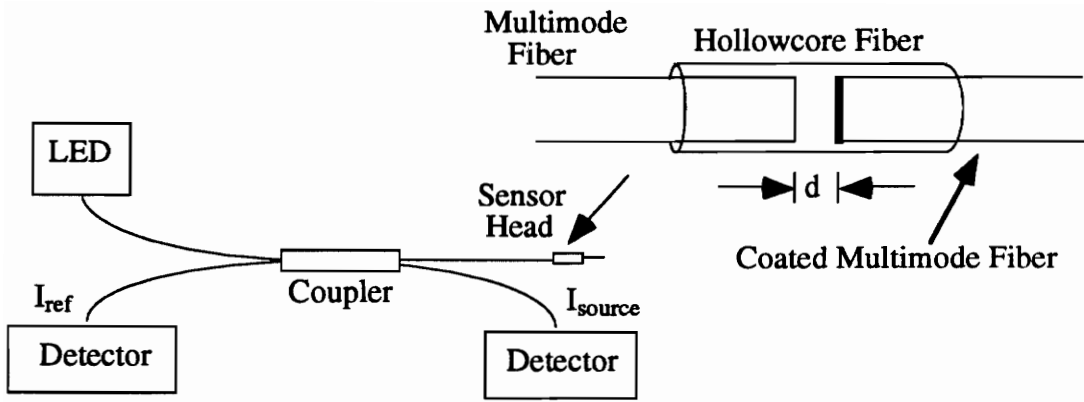


Figure 1.1 A typical configuration of an intensity based sensor [3].

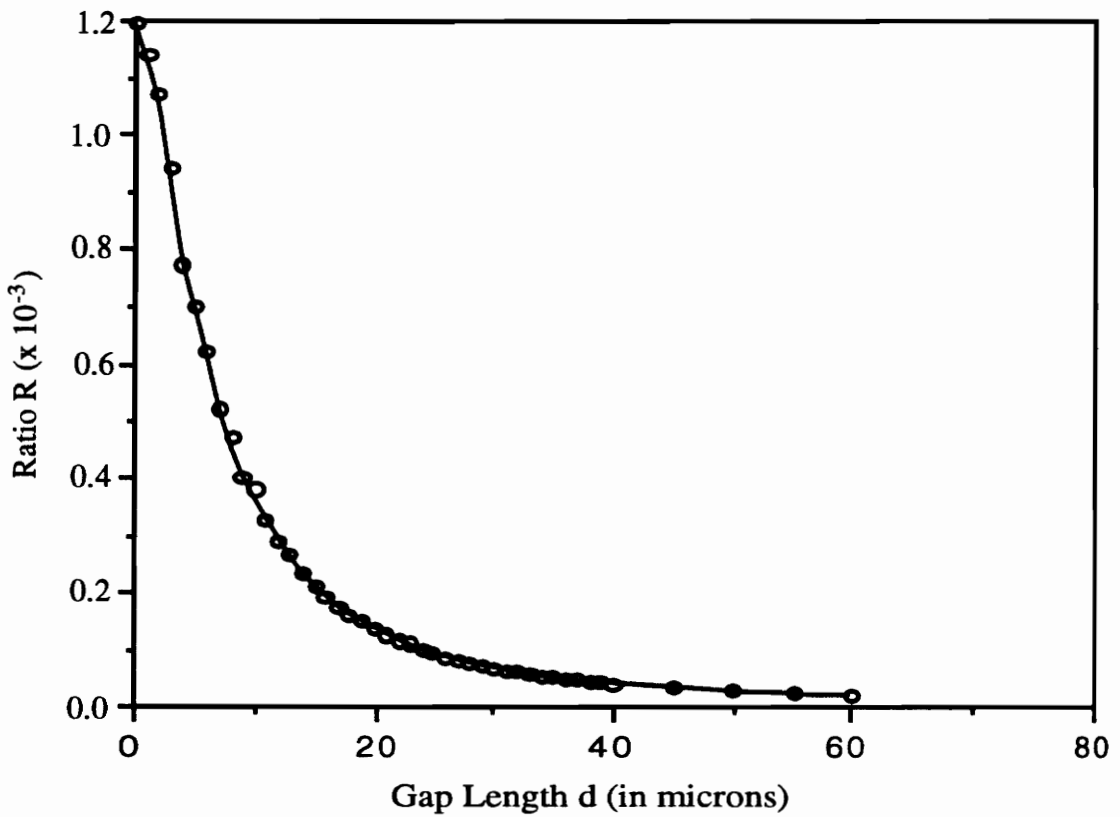


Figure 1.2 Experimental variation of ratio R versus gap length d [3].

monitored by one of the two photodetectors. The other photodetector is used to monitor the source intensity, I_{source} . The effect of source fluctuation is accounted for by taking the ratio R of I_{ref} and I_{source} , $R = I_{\text{ref}} / I_{\text{source}}$. The monotonic relationship between gap length, d , and intensity ratio, R , can be used to determine d . A plot of R versus d is shown in Figure 1.2 based on data obtained from an intensity based sensor experimental setup [3].

Although intensity based sensors are simple to construct and less expensive than interferometric sensors, they also suffer from poor sensitivity. These sensors are also susceptible to erroneous results due to fiber losses in the coupler arms other than the input arm. Moreover, each sensor has to be separately calibrated due to different shapes of the R versus d curve arising from different end face angles of the reflecting surface.

1.1.2 Interferometric Sensors

Optical fiber interferometric sensors are based on the principle of interference between two coherent light waves. An interferometer splits the optical signal from the source into two signals, induces a phase difference between the signals by introducing a path difference, combines the signals after the applied perturbation has been sensed and detects the intensity of the recombined signal. The two interfering signals are known as the reference and sensing signals. The fiber carrying the reference signal is kept isolated while the applied perturbation changes the phase of the sensing signal. The phase difference between the two signals modulates the intensity of the recombined signal. Thus, the detected intensity is a function of the applied perturbation. The combined signals interfere only if the path difference, ΔL , is less than the coherence length, L_c , of the source [1]. The coherence length, L_c , is roughly given by

$$L_c \approx \frac{\lambda^2}{\Delta\lambda}, \quad (1.1)$$

where, λ and $\Delta\lambda$ are respectively the center wavelength and 3 dB linewidth of the source.

The optical phase difference (in radians), ϕ , of light passing through a fiber is given by [1]

$$\phi = nkL, \quad (1.2)$$

where n is the refractive index of the core, $k = 2\pi/\lambda$ is the wavenumber in vacuum, and L is the physical length of the fiber. Small variations in phase delay can be found by differentiating Equation (1.2).

Therefore,

$$\frac{d\phi}{\phi} = \frac{dL}{L} + \frac{dn}{n} + \frac{dk}{k}. \quad (1.3)$$

The first two terms relate physical changes in the fiber caused by the perturbation. Therefore, they describe the mechanism by which fibers act as sensors. In general, the dL and dn terms represent changes in temperature, pressure and magnetic field. The last term represents any wavelength variations in the source.

Interferometric sensors are very sensitive and hence offer excellent resolution. These sensors also require complicated signal processing techniques to recover the information regarding the measurand [1]. Some of the different types of fiber optic interferometers in use today are: 1) Mach-Zender, 2) Michelson, and 3) Fabry-Perot. These interferometric sensors are discussed in the next section.

1.1.2.1 Mach-Zender Interferometer

A typical Mach-Zender interferometer is shown in Figure 1.3. A monochromatic source emitting at wavelength λ launches light into one of the input arms of a 2X2 singlemode coupler. Since the fiber supports only one mode at the operating wavelength, the electric field inside the fiber can be treated as a plane wave [1]. The coupler splits the optical signal into its two output arms. One of these arms act as the reference arm, while the other forms the sensing arm of the interferometer. Let us assume that the original length of both arms is L . Then, an applied perturbation will change the length of the sensing arm by ΔL . The light traveling in the reference arm does not experience this change. Thus, the perturbation induces an optical path difference of ΔL between the two optical signals. These signals are then combined by the second 2X2 coupler, and one of the output arms of the coupler is fed to a photodetector. The path difference, ΔL , between the two signals must be less than the coherence length, L_c , of the source.

The electric fields in the reference and sensing fibers of an interferometer are given by [2]

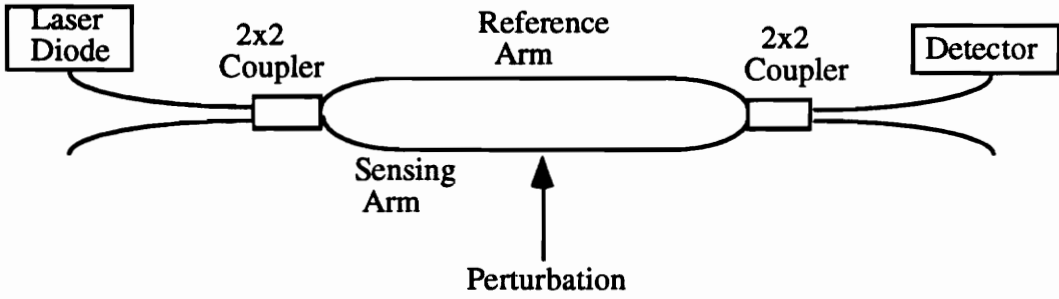


Figure 1.3 A fiber Mach-Zender interferometer [3].

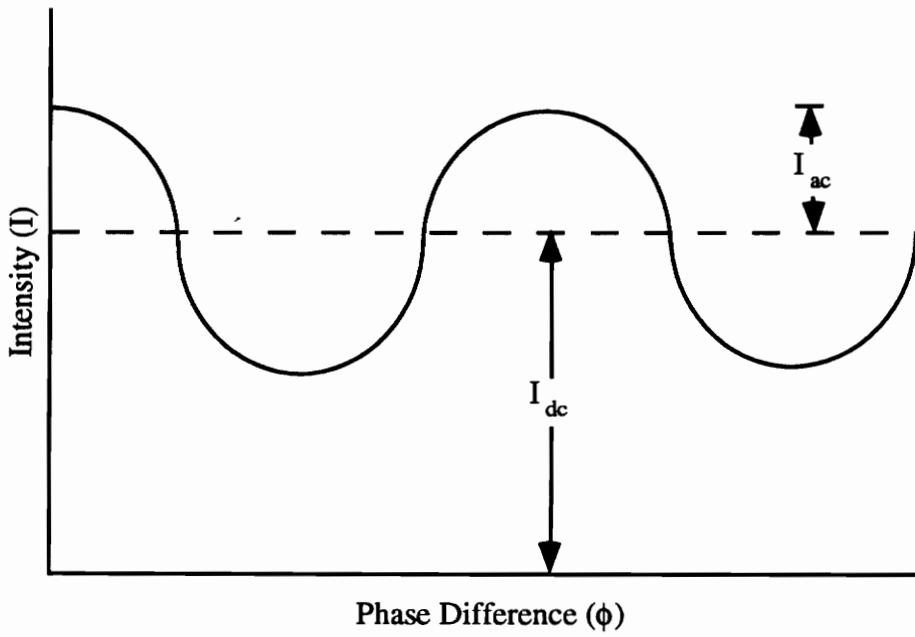


Figure 1.4 Intensity versus phase difference for a Mach-Zender Interferometer [3].

$$E_r = E_o \alpha_1 \cos(\omega t + \phi_r), \quad (1.4)$$

and

$$E_s = E_o \alpha_2 \cos(\omega t + \phi_s), \quad (1.5)$$

where E_o is the amplitude of the input field, α_1 and α_2 are the loss coefficients, while ϕ_1 and ϕ_2 are the phase terms associated with the two paths. If we assume that there is no initial (before perturbation) phase difference between the reference and sensing fields, then the phase difference between the two signals due to the perturbation is

$$\Delta\phi = \phi_r - \phi_s. \quad (1.6)$$

The output intensity at the photodetector is then given by

$$I = \langle E_r^2 \rangle + \langle E_s^2 \rangle + 2\langle E_r E_s \rangle, \quad (1.7)$$

or,

$$I = I_{dc} + I_{ac} \cos(\Delta\phi), \quad (1.8)$$

where, I_{dc} and I_{ac} correspond to the DC and AC components, respectively, of the output intensity. Figure 1.4 shows a typical output of such an interferometer with respect to increasing phase difference. The phase difference, $\Delta\phi$, between the reference and sensing arms is due to the elongation of the sensing fiber. Thus, it can be expressed as

$$\Delta\phi = \frac{2\pi \Delta L}{\lambda}. \quad (1.9)$$

We can determine the phase difference by counting the number of sine wave periods, called fringes (Figure 1.4). A fringe is defined as the change of intensity, I , between two consecutive maxima or two consecutive minima. The exact value of the measurand can be calculated from this information. The fringes appear only when the perturbation is active. Therefore, if there is no change in ΔL , the output will be a DC signal.

1.1.2.2 Michelson Interferometer

The configuration of a Michelson interferometer is shown in Figure 1.5. In this type of an interferometer, a single coupler is used to both split as well as recombine the two optical signals. At first, the coupler splits the light from the source into the reference and sensing arms. The signals are then reflected back through the same arms by the mirrors at the end of each arm. The reflected signals are then recombined by the same coupler. Since the

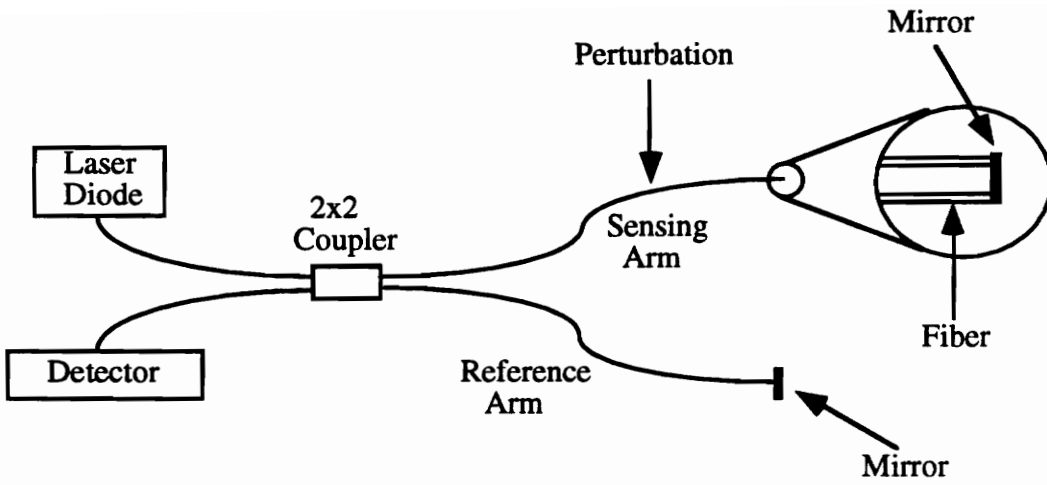


Figure 1.5 Configuration of a fiber Michelson interferometer [1].

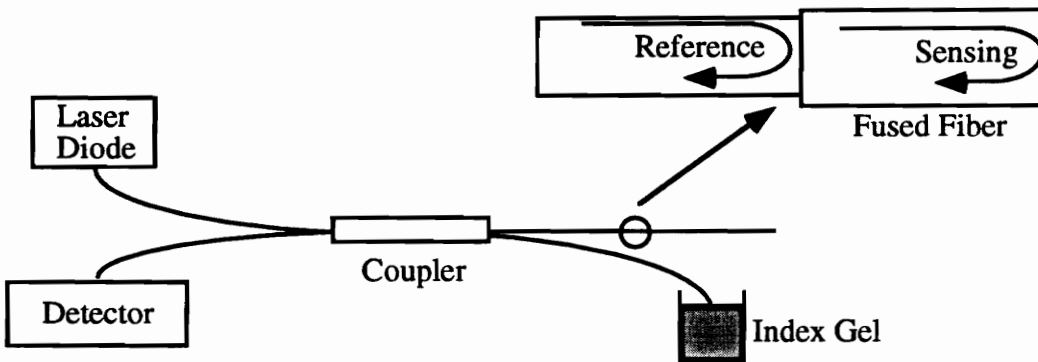


Figure 1.6 Intrinsic Fabry-Perot interferometer (IFPI) [3].

signals traverse the length of the fibers twice, in a Michelson interferometer the optical phase shift per unit length between the sensing and reference signals is doubled [4].

1.1.2.3 Fabry-Perot Interferometer

The Fabry-Perot interferometer is an example of a multibeam interferometer. The sensing fiber has two reflective surfaces at the ends. The air gap enclosed by these reflective surfaces is known as the Fabry-Perot cavity. Due to the high reflectivity of these reflective surfaces, the light bounces back and forth within the cavity and experiences phase delay in the cavity many times. These multiple reflections increase the sensitivity of the sensor [1]. The Fabry-Perot interferometer has two basic configurations known as "intrinsic" and "extrinsic". The configuration of the intrinsic Fabry-Perot interferometer (IFPI) is shown in Figure 1.6. A small length of a singlemode fiber is fused at the end of one of the arms of the 2X2 bi-directional coupler to form the Fabry-Perot cavity. The reference and sensing signals are reflected from the two ends of this cavity. The coupler then recombines these signals, and the intensity of this recombined signal is monitored to detect any variations in the length or refractive index of the Fabry-Perot cavity. The IFPI suffer from some inherent drawbacks. The gage length of the sensor cannot be changed once the reflecting fiber is fused onto the input fiber. Also, if the perturbation changes the refractive index as well as the length of the cavity it would cause the phase difference between the reference and sensing signal to have a non-linear dependence on the applied perturbation. To overcome these problems, Murphy *et al.* proposed the extrinsic Fabry-Perot interferometer (EFPI) [5]. A detailed analysis of the EFPI is presented in the following chapter.

1.2 Thesis Statement and Overview

Although the EFPI offers numerous advantages over the IFPI, it also suffers from the same limitations as other interferometric sensors. One of these limitations is known as the 'turn around point' ambiguity, which is explained in greater detail in the next chapter. This thesis investigates the use of two wavelength interferometry to overcome the 'turn around point ambiguity' in EFPIs. It describes the issues involved in designing an EFPI based dual wavelength strain sensing system and presents a complete system design. Chapter 2 contains a detailed analysis of the EFPI, its advantages and limitations, and current techniques used at the Fiber & Electro-Optics Research Center (FEORC) to resolve some of its limitations. Chapter 3 discusses the theory behind two wavelength interferometry in Fabry-Perot cavities and describes the system and component designs adopted to implement

the two wavelength EFPI strain sensing system. The theoretical analysis behind the derivations and calculations of the different system parameters is given in Chapter 4. Chapter 5 involves the description of the experimental setup and results. Conclusions of this research, and suggested future work are presented in Chapter 6.

Chapter 2 - Extrinsic Fabry-Perot Interferometer

In this chapter we present a detailed analysis of the extrinsic Fabry-Perot interferometer (EFPI). We discuss its advantages and limitations, and describe the two main EFPI based sensing systems that have been developed to overcome its limitations.

2.1 Theory and Fabrication

When an electromagnetic wave propagating in an dielectric medium encounters another dielectric medium with a different refractive index (or intrinsic impedance), a portion of the wave is reflected and a portion is transmitted [6]. Fabry-Perot interferometers, such as the EFPI, operates on the principle of interference between two or more light beams generated by such phenomena and uses optical path length difference between two signals to measure strain. Interference between the beams can be constructive or destructive. Constructive interference occurs when the optical path length difference between the beams is an even multiple of the wavelength. At such instances the signal from the interferometer is at a maximum. On the other hand, destructive interference arises when the path length is an odd multiple of half wavelength. The interferometer signal at such instances is at a minimum.

The construction of the EFPI is shown in Figure 2.1. The sensor comprises a Fabry-Perot cavity or air gap, formed by a singlemode fiber and a multimode fiber. The fibers are placed inside a hollow-core fiber, which is a glass capillary tube that serves to align the fibers. The single mode fiber is used as the input-output fiber, whereas the multimode fiber is used solely as a reflector. If the fiber ends are uncoated, a 4% Fresnel reflection occurs at both ends of the cavity. The first reflection is at the glass-air interface at the front of the air gap. This reflection is known as the reference reflection and is independent of the applied perturbation. The second reflection occurs at the air-glass interface at the far end of the air gap. This is called the sensing reflection. The sensing reflection is dependent on the length of the cavity, d . When the sensor is strained, the length of the cavity changes, which in turn causes a change in phase difference between the reference and sensing signals. These two reflections then interfere in the input-output fiber as long as $2d$ is less than the coherence length, L_c , of the source. The other end of the multimode fiber is usually shattered and index-matching gel is used to prevent reflections from this end.

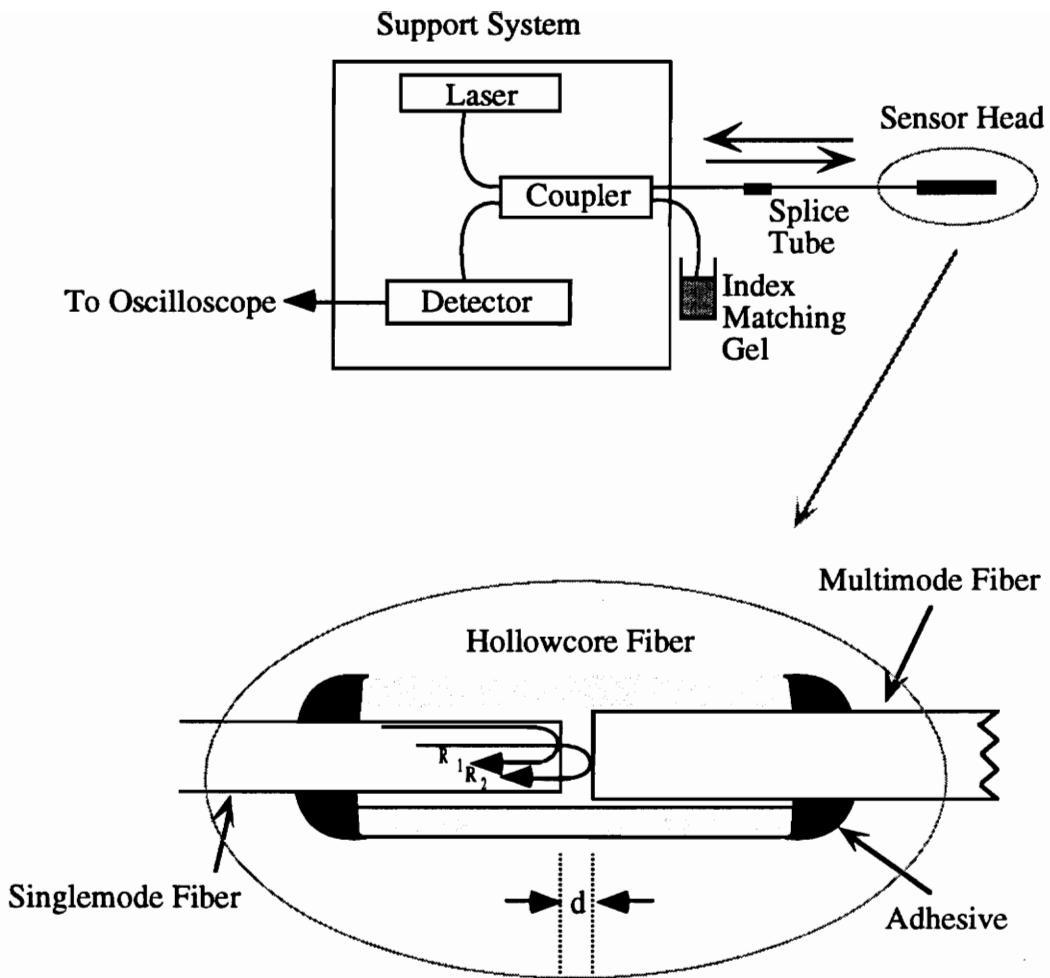


Figure 2.1 The extrinsic Fabry-Perot interferometer (EFPI) with details of the sensor system [3].

As mentioned earlier, Fabry-Perot interferometers are multibeam interferometers. Hence, in the EFPI, multiple reflections occur within the Fabry-Perot cavity. The effect of the reflections subsequent to the ones mentioned above is negligible. In order to prove this, first let us consider the Fabry-Perot cavity shown in Figure 2.2. Assuming normal incidence, the ratio of the reflected light intensity, I_r , to the incident intensity I_i , for the interferometer with equal interface reflectivities can be expressed as [7]

$$\frac{I_r}{I_i} = \frac{2R(1-\cos(\phi))}{1 - 2R\cos(\phi) + R^2} \quad (2.1)$$

where, ϕ is the round trip phase shift, and R is the reflectivity at each interface. The phase shift, ϕ , is given by

$$\phi = \frac{4\pi d}{\lambda} \quad (2.2)$$

Therefore, if the wavelength and reflectivity at the interfaces are constant, the reflected intensity is simply a function of the gap displacement, d .

If the index of refraction of the glass is assumed to be 1.46, then the reflectivity, $R = 0.035$. If we neglect the terms containing R^2 and expand equation 2.1 using

$$\frac{1}{1-x} \approx 1+x, \quad (2.3)$$

we get,

$$\frac{I_r}{I_i} \approx 2R(1 - \cos(\phi)) \quad (2.4)$$

$$= I_{dc} + I_{ac}\cos(\phi). \quad (2.5)$$

It can be seen that Equation (2.5) is the interference of only two waves, and resembles the output from a Mach-Zender interferometer. A plot of the multibeam and the two beam intensity transfer functions versus phase is shown in Figure 2.3. A maximum error of 6.5% occurs when

$$\phi = 2\pi\left(m + \frac{1}{2}\right), \quad (2.6)$$

where m is an integer [8]. The small error between the two beam and multibeam transfer functions can be considered negligible, and the two beam approximation is usually used [9].

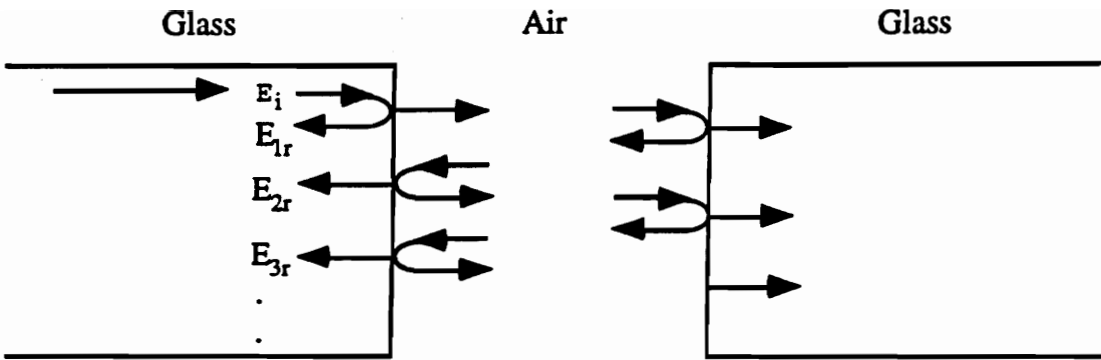


Figure 2.2 Fabry-Perot cavity with multiple reflections [3].

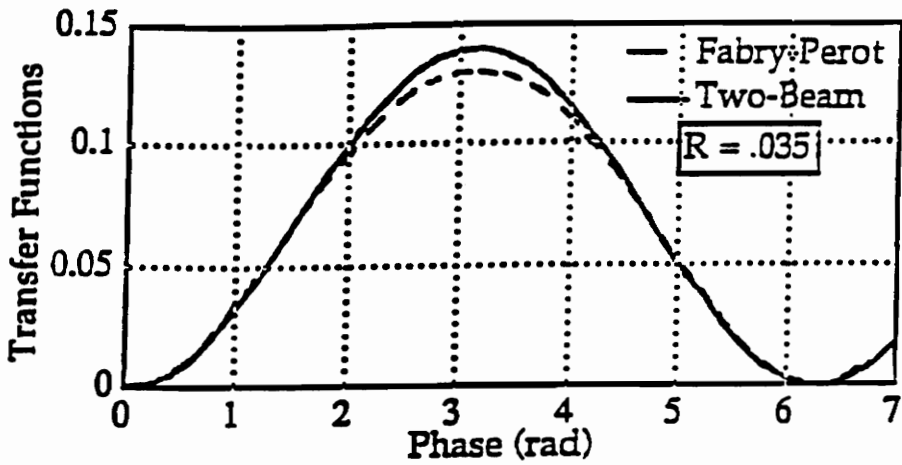


Figure 2.3 Fabry-Perot transfer functions [8].

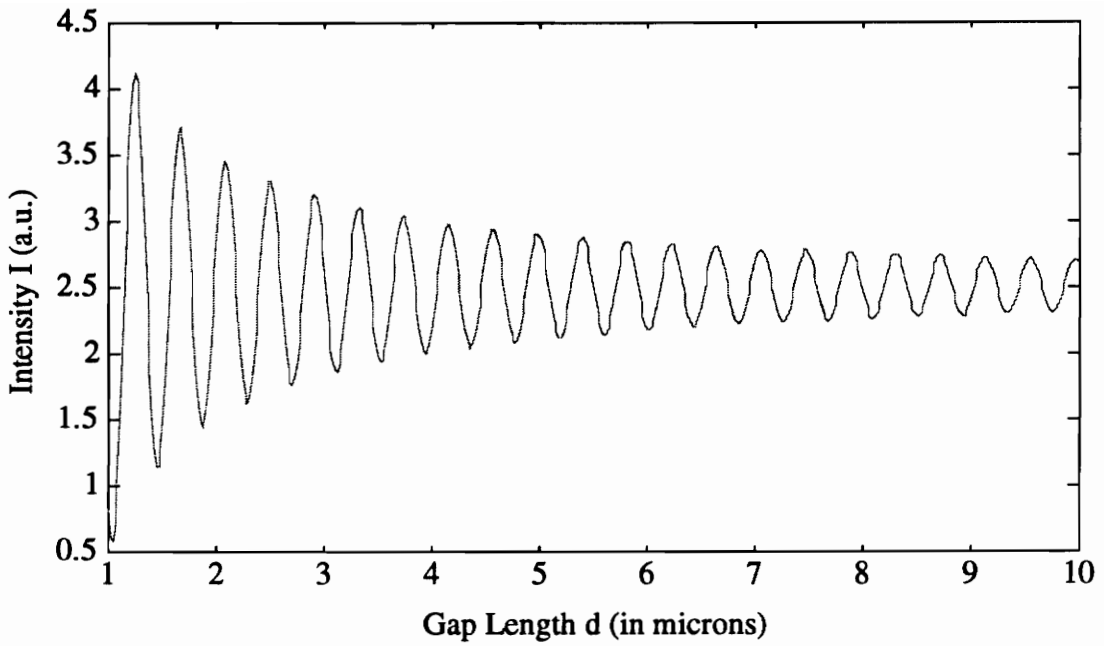


Figure 2.4 Variation of EFPI output intensity with increasing gap length.

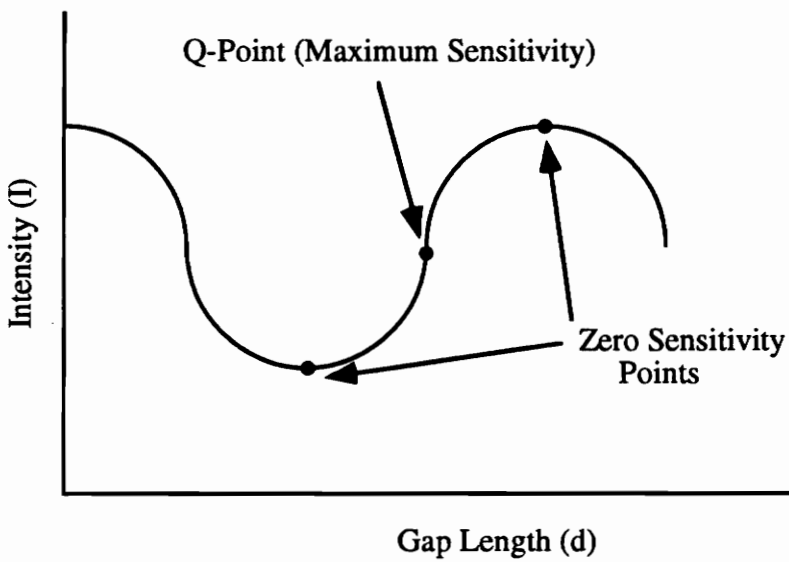


Figure 2.5 Sensitivity variation of an EFPI along its transfer function curve [3].

If the output of the EFPI is assumed to be the interference between two plane waves, it can be represented in terms of its complex amplitude $U_i(x, z, t)$, and is given by [10]

$$U_i(x, z, t) = E_i \exp(j\phi_i), \quad i=1,2. \quad (2.7)$$

The reference and sensing reflections are denoted by the subscripts $i=1, 2$ respectively. If we express the sensing reflection coefficient, E_2 , in terms of the reference reflection coefficient E_1 , we get [10]

$$E_2 = E_1 \left[\frac{ta}{a + 2d \tan(\sin^{-1}(NA))} \right], \quad (2.8)$$

where 'a' is the radius of the core of the fiber, 't' is the transmission coefficient of the air-glass interface, 'd' is the gap length, and NA is the numerical aperture of the singlemode fiber. The quantity NA is given by [10]

$$NA = \sqrt{n_1^2 - n_2^2}, \quad (2.9)$$

where, n_1 and n_2 are the refractive indices of the core and cladding, respectively. The intensity at the detector is then given by [10]

$$I_{\text{det}} = |U_1 + U_2|^2 = |E_1|^2 + 2E_1E_2 \cos(\phi_1 - \phi_2) + |E_2|^2, \quad (2.10)$$

or,

$$I_{\text{det}} = E_1^2 \left[1 + \frac{2ta}{a + 2d \tan[\sin^{-1}(NA)]} \cos\left(\frac{4\pi d}{\lambda}\right) + \left(\frac{ta}{a + 2d \tan[\sin^{-1}(NA)]} \right)^2 \right]. \quad (2.11)$$

From Equation (2.11), we find that the low-finesse EFPI has a sinusoidal response to a linear strain field. Moreover, it can also be seen that as the air gap, d, between the single mode and multimode fibers is increased, the relative intensity of the sensing reflection reduces with respect to the reference reflection. Hence, a decaying envelope is imposed on this sinusoidal response. The envelope limits the dynamic range of the sensor, since the signal-to-noise ratio (SNR) of the detected signal degrades as the relative intensity of the sensing reflection decreases. Figure 2.4 shows a simulation of the variation in the output intensity of an EFPI with increasing gap length.

2.2 Advantages of the EFPI

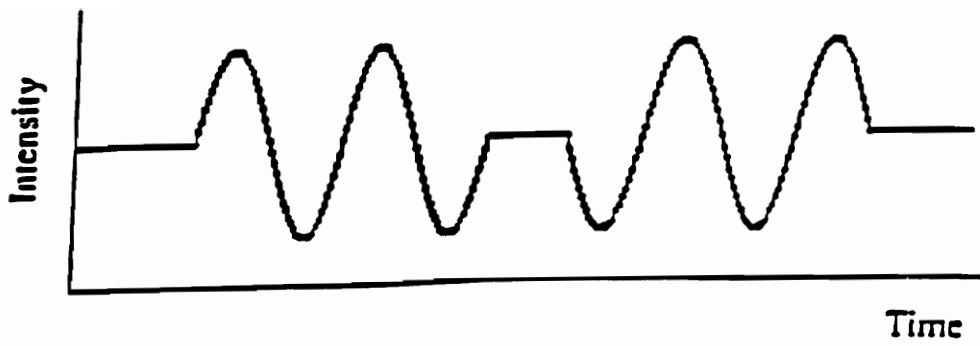
The EFPI offers significant advantages over other types of phase sensors. Due to its small interaction length, it has the ability of being a point sensor. Thus, it can easily be bonded onto different materials for effectively monitoring strain, temperature, and vibration. Typical specifications for the EFPI are a gage length of 2 mm-4 mm and an

initial air gap separation of about 40 μm -50 μm [4]. The EFPI is easy to construct, and its small size and weight make it very easy to work with. These features allow it to be easily embedded in composite materials. Unlike the intrinsic Fabry-Perot Interferometer (IFPI), the EFPI senses strain only along its axis. It therefore, is an ideal candidate for smart structures and skins applications. It also has a wide frequency response. Limitations on the frequency range are due to the signal processing electronics at the detector end.

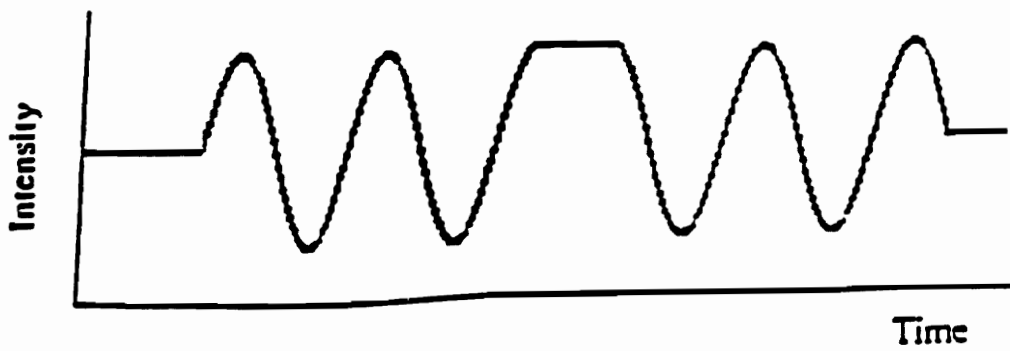
2.3 Limitations of the EFPI

The EFPI suffers from the same limitations as other interferometric sensors. Figure 2.5 shows the transfer function curve as a function of the gap length for an EFPI. The Q-point or the quiescent-point, is the point in the middle of the linear region of the curve. If the sensor is operated at the Q-point it is extremely sensitive to minute variations in applied perturbation. On the other hand, the sensitivity of the sensor reduces drastically if the operating point is at a peak or trough of the curve (only a quarter of a fringe away on both sides). Thus, sensitivity is a function of the gap length. The reduced sensitivity of the EFPI at the peak and trough of the transfer curve also gives rise to the 'turn around point' effect, i.e. when the gap length of the EFPI changes direction due to a change in the direction of the perturbation. If this directional change takes place in the linear region of the transfer function, the turn around point in the output is very distinct which can be seen in Figure 2.6 (a). However, if this change occurs when at the maxima or a minima of the curve, the sensor fails to correctly distinguish the turn around point. This ambiguity is illustrated in Figure 2.6 (b). In this type of a situation, it is unclear whether the sensor was strained in a particular direction and then released, or if it was strained in one direction, held, and then strained once again in that same direction [11].

Another inherent drawback of the EFPI and other interferometric sensors is that they are differential measurement systems. The sensor does not have the capability to retain information about the perturbation after the system is powered off and turned on again.



(a)



(b)

Figure 2.6 (a) Example of distinct EFPI turn around point (b) Example of ambiguous EFPI output [11].

2.4 Existing EFPI Based Sensor Systems

2.4.1 Quadrature Phase Shifted EFPIs

If two signals can be obtained which are always in quadrature (90° out of phase with each other), for the same perturbation, there would be at least one signal which is not at the minimum sensitivity point on the transfer function curve. The directional change of the measurand, can then be unambiguously detected. The quadrature phase-shifted EFPI (QPS-EFPI), proposed by Murphy *et al.* [10], is based on this idea. The QPS-EFPI requires two EFPI cavities in close proximity to obtain two signals in quadrature. The sensor arrangement is shown in Figure 2.7. If d_1 and d_2 are the lengths of the top and bottom cavities respectively, then the phase difference between the two signals is given by

$$\Delta\phi = \frac{4\pi}{\lambda}d_1 - \frac{4\pi}{\lambda}d_2. \quad (2.12)$$

The two signals will be in quadrature if $\Delta\phi$ is an odd multiple of $\pi/2$,

$$\frac{4\pi}{\lambda}(d_1 - d_2) = (2n + 1)\frac{\pi}{2}, \quad (2.13)$$

or,

$$d_1 - d_2 = \frac{(2n + 1)\lambda}{8}. \quad (2.14)$$

However, just like the conventional EFPI, the QPS-EFPI is also a differential measurement system. Also, the difference between d_1 and d_2 can only be fixed, discrete values, which makes the sensor fabrication difficult.

In the next section another EFPI based sensor system also developed at the Fiber & Electro-Optics Research Center (FEORC), called the absolute EFPI (AEFPI), has been discussed.

2.4.2 Absolute EFPIs

The AEFPI overcomes nearly all the basic limitations of an EFPI. In addition to eliminating the directional change ambiguity, the AEFPI also offers the ability to make absolute, real-time measurements of the cavity length, d . Therefore, the system can be deactivated and reactivated without losing any information during down-time. However,

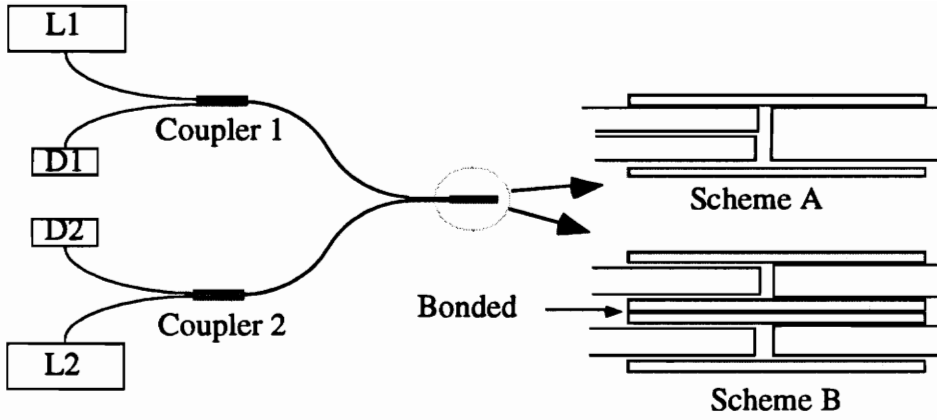


Figure 2.7 Two proposed configurations of quadrature phase-shifted EFPIs [3].

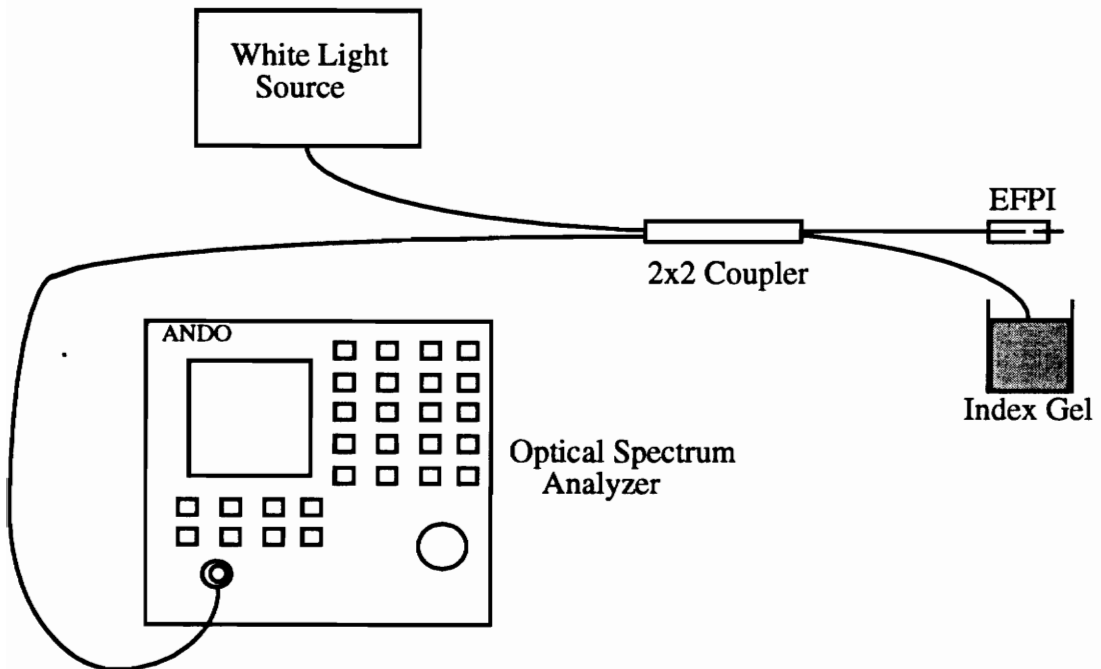


Figure 2.8 Setup for the absolute EFPI (AEFPI) system [3].

the speed of the current demodulation technique employed in such a system is extremely slow. Therefore, it is not a viable system for dynamic strain measurements.

The AEFPI uses the concept of white light interferometry [12]. In this setup, the sensor head is interrogated with a broadband source (instead of a laser diode), that injects many wavelengths into the fiber. At the detecting end, the photodetector unit of an EFPI system is replaced with an optical spectrum analyzer (OSA), which measures the light intensity for a given cavity length as a function of input wavelengths. The phase difference, $\Delta\phi$, between two fixed wavelengths, λ_1 and λ_2 is given by

$$\Delta\phi = \frac{4\pi d}{\lambda_1} - \frac{4\pi d}{\lambda_2} . \quad (2.15)$$

The basic configuration of this system using an EFPI is shown in Figure 2.8. The signal processing for such a system can be done either by the constant wavelength or by the constant phase technique [13].

2.4.2.1 Constant Wavelength Technique

If the phase difference, $\Delta\phi$, between two fixed wavelengths, λ_1 and λ_2 , is resolved, the absolute cavity length, d , can be determined. We can derive the expression for the cavity length, d , by manipulating equation 2.15 to get

$$d = \frac{\lambda_1 \lambda_2}{4\pi(\lambda_1 - \lambda_2)} \Delta\phi . \quad (2.16)$$

2.4.2.2 Constant Phase Technique

In white light interferometry, usually the constant phase technique is employed for demodulation, since it is cumbersome to compute the exact phase difference between any two fixed wavelengths. In the constant phase technique, a phase difference value (generally 2π or its multiples) is fixed such that

$$\Delta\phi = 2n\pi = \frac{4\pi}{\lambda_1} d - \frac{4\pi}{\lambda_2} d , \quad (2.17)$$

or,

$$d = \frac{n(\lambda_1 \lambda_2)}{2(\lambda_2 - \lambda_1)} , \quad (2.18)$$

where, n is an integer. For $n=1$, equation 2.18 reduces to

$$d = \frac{(\lambda_1 \lambda_2)}{2(\lambda_2 - \lambda_1)}. \quad (2.19)$$

Thus, if we can determine two wavelengths corresponding to two successive maxima or minima on the OSA, we can measure the absolute gap of the cavity.

Chapter 3 - Dual Wavelength Extrinsic Fabry-Perot Interferometer

In this chapter we investigate the application of two wavelength interferometry in Fabry-Perot cavities to solve the directional ambiguity problem associated with the extrinsic Fabry-Perot interferometer (EFPI). A system design to implement a two wavelength strain sensing system using the EFPI is also proposed.

3.1 Theory and Motivation

As mentioned in the previous chapters, interferometric fiber sensors exhibit extremely high sensitivity to a range of different measurand fields. Unfortunately, due to the periodic nature of their transfer functions, the output of these sensors are intrinsically ambiguous. When the applied perturbation changes its polarity, phase sensors are not able to detect this change if the switch in direction takes place at the maximum or the minimum of the transfer function curve. Various authors have shown that two wavelength interferometry can be used to extend the range of unambiguity and increase the measurement sensitivity in optical path length and surface profile measurements [14], [15]. A temperature sensor based on dual-wavelength interrogation of a sensing Mach-Zender and receiving Michelson interferometer has also been reported [16].

In the preceding chapter, we described an EFPI based sensing technique, called the quadrature phase-shifted EFPI (QPS-EFPI), that can be used to unambiguously detect directional changes of dynamically varying strain. The QPS-EFPI requires the use of two Fabry-Perot cavities. However, often there is a need for sensors that are suitable for embedding in structures or for sensing in harsh environments, where minimizing the size of the sensor head is important to obtain highly localized measurements, to reduce the cross sensitivity to other measurands, and to minimize potential damage to the sensor itself. Under such circumstances, the use of QPS-EFPI will not be appropriate. The size of the sensor head becomes a particularly important issue in smart structures and smart skins applications. The absolute EFPI (AEFPI) strain sensing system offers the ability to detect the cavity length absolutely, and also eliminates the need for fringe counting. However, this technique cannot be employed for dynamic strain measurements because of its extremely slow demodulation process. Therefore, in this chapter we propose the design of another EFPI based sensor system, based on two wavelength interferometry,

that unambiguously detects directional changes of a dynamically varying strain field utilizing only one Fabry-Perot cavity.

In phase sensors, if the phase difference between the reference and sensing reflections varies sinusoidally with time, and the peak-to-peak variation is large enough to push the sensor out of the linear range, we observe fringes at the output of the detector [10]. For a dynamic strain measurement system, the basic principle of operation can be described by considering two sinusoidal transfer functions which are out of phase with each other due to the interrogation of the cavity by two different wavelengths. This dual-wavelength interrogation of the sensor can be used to overcome the turn around point ambiguity associated with an interferometric sensor if the upper and lower bounds of the sensor range are known. The difference in the phase shift measured at each wavelength is a function of the path difference, d , which, depending on the wavelengths used and their difference, can correspond to numerous individual interferometer fringes. Operation of the sensor within this range allows unambiguous detection in the change of polarity of the induced strain [1].

For an EFPI illuminated by two coherent sources, λ_1 and λ_2 , and having a gap length, d , the phase differences between the reference and sensing signals at each wavelength are given by

$$\Delta\phi_1 = \frac{4\pi d}{\lambda_1}, \quad (3.1)$$

and,

$$\Delta\phi_2 = \frac{4\pi d}{\lambda_2}. \quad (3.2)$$

Therefore, the relative phase difference between the two fringe patterns is,

$$\Delta\Phi = \frac{4\pi d \Delta\lambda}{\lambda_1 \lambda_2}, \quad (3.3)$$

where $\Delta\lambda$ is the wavelength difference, $\lambda_1 - \lambda_2$. The unambiguous range in cavity length, d , is determined by $0 < \Delta\Phi < \pi$ radians. Figure 3.1 shows a simulated EFPI response with dual-wavelength operation for $\lambda_1 = 670$ nm and $\lambda_2 = 720$ nm. It can be seen from the plot that within the range described above, the zero sensitivity points (maxima or minima) of the output for one wavelength do not correspond to the zero sensitivity

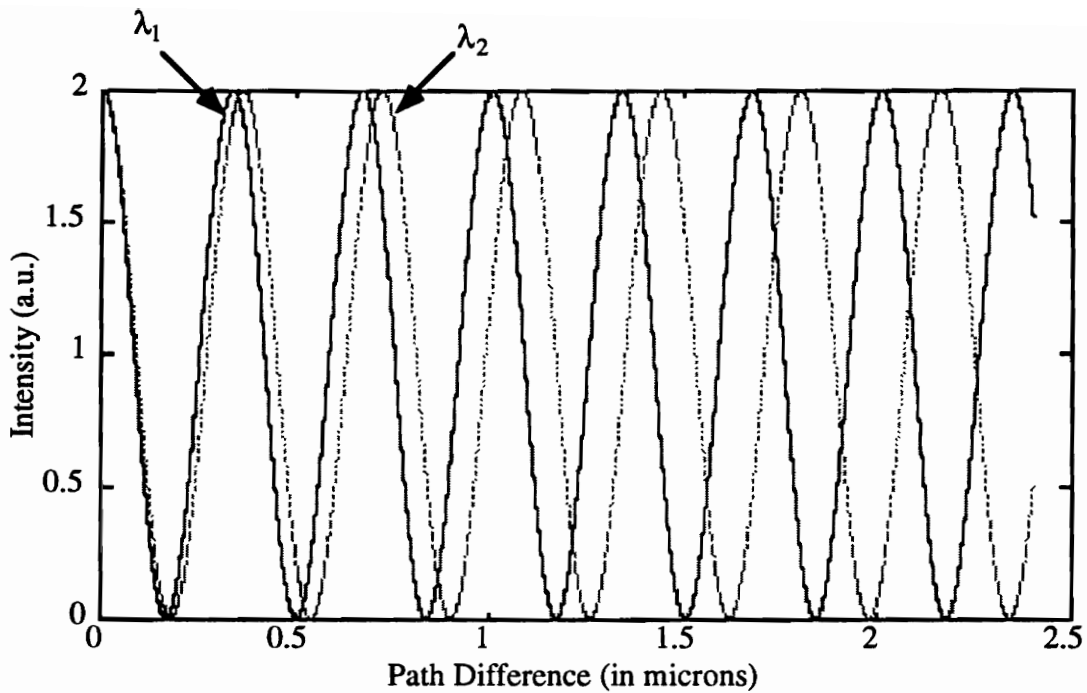


Figure 3.1 Interferometric output response with dual wavelength operation.

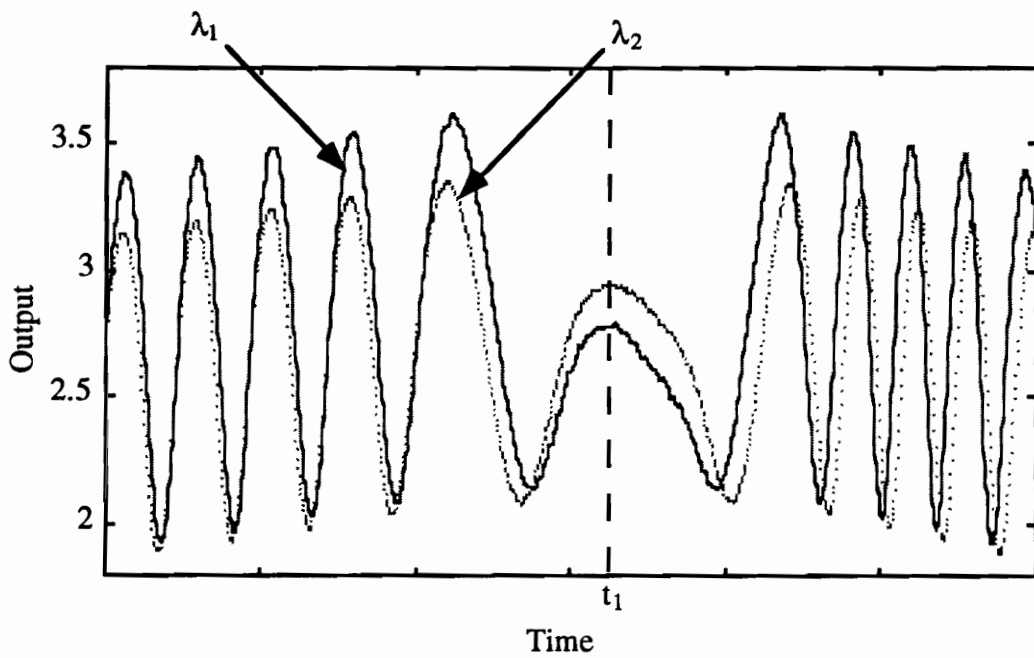


Figure 3.2 Lead-lag relationship between EFPI output waveforms.

points of the output for the other wavelength. Thus, within this range, the turn around point will be detected in at least one of the two fringe patterns.

Keeping track of the lead-lag phenomenon between the two output wave forms also gives us unambiguous information about the relative direction of the strain. The phenomenon can be seen in Figure 3.2. The figure shows actual experimental data from an EFPI that was interrogated with two LDs operating at $\lambda_1 = 1291.93$ nm and $\lambda_2 = 1294.65$ nm. Initially the output wave form for the first wavelength, λ_1 , leads that of the second wavelength λ_2 , until time t_1 . At time t_1 , the phase difference, $\Delta\Phi$, changes direction (because of a change in direction of the strain) and the output wave forms switch their lead-lag properties. We observe that the output for λ_2 now leads that for λ_1 .

3.2 Determining Dynamic Range

The dynamic range of a sensor is the total range of the sensor from minimum to maximum. Equation (3.3) also helps us to determine the maximum dynamic range of the dual-wavelength EFPI system, in term of gap length, in any one direction (tension or compression) from the original gap length (bias point) of the sensor. If we start from a gap of zero and elongate the cavity, the maximum gap length, d_{\max} , for which unambiguous detection is possible occurs when $\Delta\Phi$ is π radians, where

$$d_{\max} = \frac{\lambda_1 \lambda_2}{4\Delta\lambda}. \quad (3.4)$$

Therefore, to achieve equal dynamic range for both tension and compression, $\Delta\Phi$ cannot exceed 0.5π radians or 90° in any one direction from the bias point. By manipulating equation (3.3), we find that equal and therefore optimum dynamic range of the sensor in both directions is realized when the bias point is set at

$$d_{\text{bias}} = \frac{(2n + 1)\lambda_1 \lambda_2}{8\Delta\lambda}, \quad (3.5)$$

where $n = 0, 1, 2, 3, \dots$. It is important to note that as n becomes larger, the cavity length increases. The losses in the cavity also increase, and the signal to noise ratio of the output signal for both wavelengths deteriorates. Thus, to achieve a satisfactory signal to noise ratio, a small value for n should be chosen.

If the bias point is set according to Equation (3.5), the operating range of the sensor, in terms of gap length, becomes

$$(d_{\text{bias}} - \Delta d_{\text{max}}) < \text{range} < (d_{\text{bias}} + \Delta d_{\text{max}}), \quad (3.6)$$

where,

$$\Delta d_{\text{max}} = \frac{\lambda_1 \lambda_2}{8\Delta\lambda}. \quad (3.7)$$

The quantity, Δd_{max} , is the maximum displacement of the Fabry-Perot cavity from the bias point in any one direction

For example, let us set the bias point, d_{bias} , of an EFPI that is to be interrogated by two wavelengths, $\lambda_1=1.30 \mu\text{m}$ and $\lambda_2=1.31 \mu\text{m}$, at $63.86 \mu\text{m}$ ($n=1$). The sensor will be able to measure induced strain as well as detect directional change as long as the change in gap length (due to the strain) does not exceed $21.28 \mu\text{m}$ in any direction from the bias point. Therefore, the operating range of the sensor is in between displacements of 42.58 and $85.14 \mu\text{m}$.

From Equation (3.7) it can be seen that the dynamic range of the system increases for longer operating wavelengths and/or a smaller wavelength difference between them. However, as the wavelength difference between the sources is decreased, it also becomes more difficult to detect changes in direction at the two extremes of the operating range, i.e. when $\Delta\Phi$ approaches 0 or π radians. Also, Equation (3.7) gives the dynamic range of the sensor for a noise free system. In reality, the different noise mechanisms in a practical system will reduce the operating range of the sensor.

3.3 Possible System Topologies

There are a number of ways a dual-wavelength EFPI sensing system can be implemented. We, however, considered the three following system topologies: a dual laser continuous wave (CW) system, a dual laser time division multiplexed (TDM) system, and a single laser TDM system.

3.3.1 Dual Laser CW System

In this scheme, two different laser diodes (LDs) are used as the two wavelength sources. Each laser is operated in the CW mode, where the drive current for each LD is held constant throughout the time of operation. The back reflection from the sensor

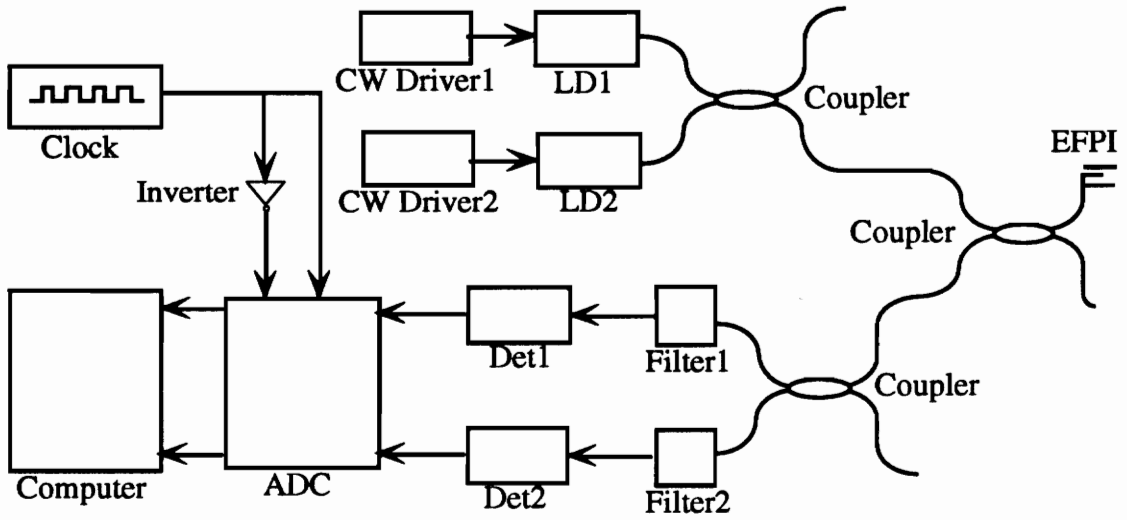


Figure 3.3 Block diagram of dual laser CW topology.

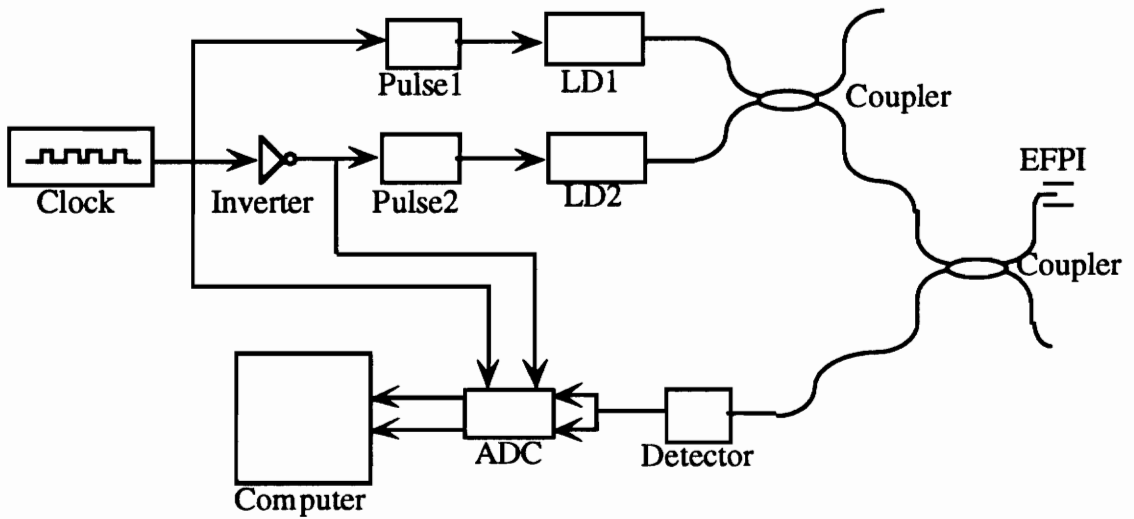


Figure 3.4 Block diagram of dual laser TDM topology.

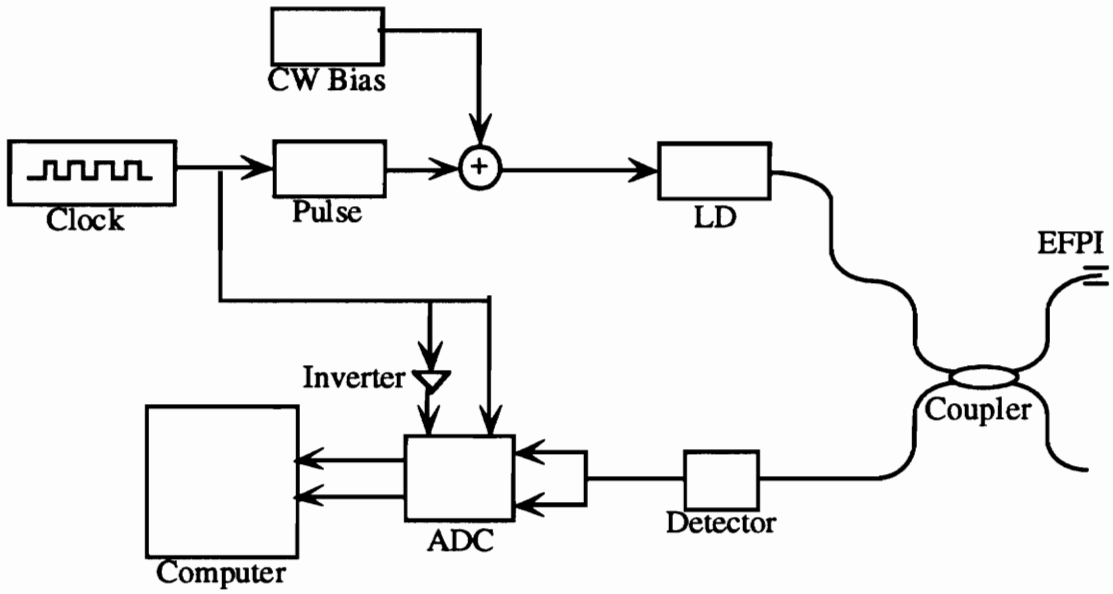


Figure 3.5 Configuration of single laser TDM topology.

simultaneously contains the phase information for both wavelengths, and is split into two separate signals by means of a 2X2 coupler. The sensor output for λ_1 is obtained after the signal in one coupler arm is passed through a narrow band optical filter centered at λ_1 , while the sensor output for λ_2 is detected after the signal in the other arm is passed through another narrow band filter centered at λ_2 . The analog signals for both wavelengths then are sampled, digitized, and uploaded in the computer.

The CW scheme is very easy to implement. The laser driver circuits are simple and no complex synchronization technique between the transmitting and receiving ends is necessary. It is also the costliest, since it requires two narrow band optical filters in addition to two laser diodes. Moreover, the transmission losses at the filters also impose an additional power penalty on the system. The imposed power penalty increases the probability of having to use lasers with higher power ratings and/or receivers with better sensitivity. The block diagram of this system topology is shown in Figure 3.3.

3.3.2 Dual Laser TDM System

The TDM scheme is realized by alternately pulse modulating (turning on and off) the two light sources. The back reflection from the sensor sequentially carries the phase information for the two wavelengths. To implement this system, the speed at which the lasers are switched must be much faster than the rate of change of the Fabry-Perot cavity due to the applied perturbation. Otherwise, the correct value of the phase difference, $\Delta\Phi$, between the fringe patterns cannot be obtained. Also, precise synchronization between the two transmitters and the receiver, and between the receiver and analog to digital converter (ADC) is necessary for proper implementation of this technique.

The nature of digital modulation and multiplexing requires this scheme to have relatively complex designs for the transmitters and receiver. However, it is also cheaper to implement than the CW system since optical filters are no longer required. The omission of optical filters also improves the power budget of the system. Figure 3.4 illustrates the configuration for this system.

3.3.3 Single Laser TDM System

In this scheme, the drive current of a single LD is switched between two levels. Unlike the other two systems, where the drive circuit supplies either a constant current (DC) or a

pulsed current, this system requires the drive circuitry to supply both. The value of the DC component should be above the threshold current of the laser. The pulsed input then should be used to switch the laser current between this state and a higher state. A bias-tee network can be used to combine the DC and pulsed current sources. The bias-tee network is a T filter specifically designed to combine RF and DC supplies. Since the output wavelength of a semiconductor laser diode depends on the drive current, this action forces the same laser diode to alternately emit radiation of two different wavelengths. Thus, this scheme achieves the same goal as the dual laser TDM system.

The single laser TDM system allows the use of only one LD. Laser diode modules that are to be used in a dual-wavelength EFPI sensing scheme are very costly since they need to be optically isolated and pigtailed. Thus, the biggest advantage of implementing such a system is cost efficiency. However, the electronic circuitry that need to employed in this scheme is the most complex among the three proposed schemes. The system block diagram for this scheme is shown in Figure 3.5.

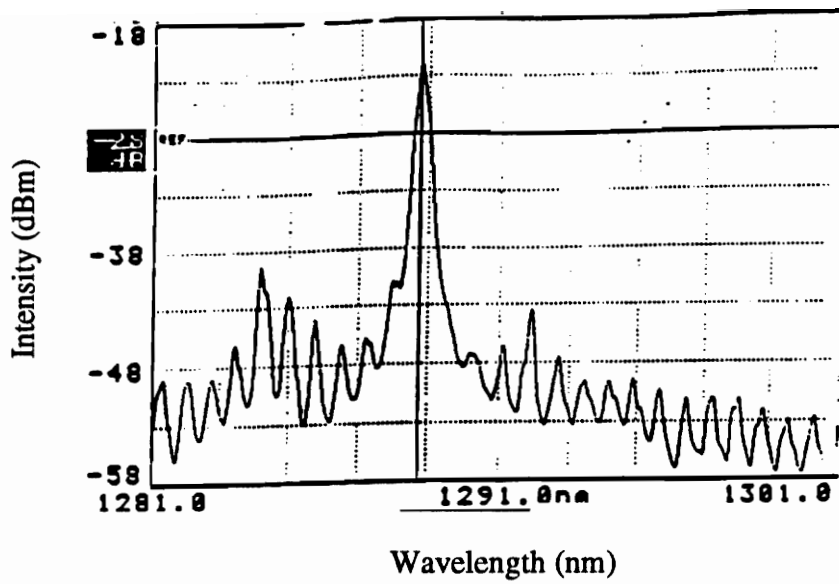
3.3.4 Choosing System Topology

The cost advantage of the single laser TDM system made it the most attractive scheme for implementation. A significant amount of research was conducted in the laboratory to investigate its feasibility.

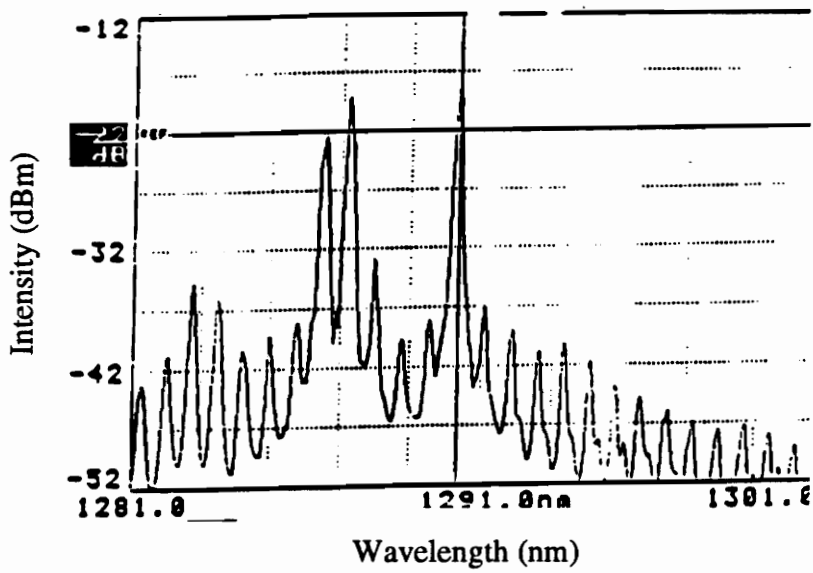
We designed and fabricated a DC current source using a Mitsubishi 55610P laser diode driver chip. This chip is capable of supplying up to 120 mA of drive current. It also has a feedback system that protects the laser diode from overcurrent damage. A pulsed current source, capable of a switching speed of up to 100 kHz, was also fabricated. A bias-tee network was used to combine the DC and pulsed current sources.

The laser module for the single laser TDM system must have the capability of significantly shifting the center wavelength of its emission spectrum as the drive current through the laser is varied. At the same time, it should have a stable emission spectrum that maintains a narrow linewidth and does not show any mode hopping characteristics.

At the laboratory, we used the optical spectrum analyzer (OSA) to analyze the emission spectrum of three types of LDs at different drive currents. These were Sharp AC 9550,



(a)



(b)

Figure 3.6 Optical emission spectrum of Mitsubishi 7781A LD. (a) and (b) are the spectrum of the LD for the same drive current at two different time instants.

Mitsubishi 7781A, and Mitsubishi 7011R. The first one is a 830 nm module, while the latter ones are both 1300 nm modules.

The AC 9550 showed no significant shift in peak wavelength (less than 0.5 nm) as the drive current was varied over a wide range. The Mitsubishi 7781A displayed such a shift, but its output spectrum was found to be unstable. Even for the same drive current, the shape of the spectrum changed considerably with respect to time. Figure 3.6 shows the optical emission spectrum of the laser at two different time instants for a drive current of 15.1 mA.

The Mitsubishi 7011R LD had a stable emission spectrum throughout the range of operating drive current. For drive currents just below the suggested operating current, I_{op} , the laser appeared to be single moded, with a distinct dominant mode. However, as the drive current was increased, some of the other non-dominant modes became prominent. As the drive current surpassed I_{op} , these modes also became equally significant and at that point the LD displayed multiple emission wavelengths. Thus, this LD was also deemed unsuitable for use in a single laser TDM system.

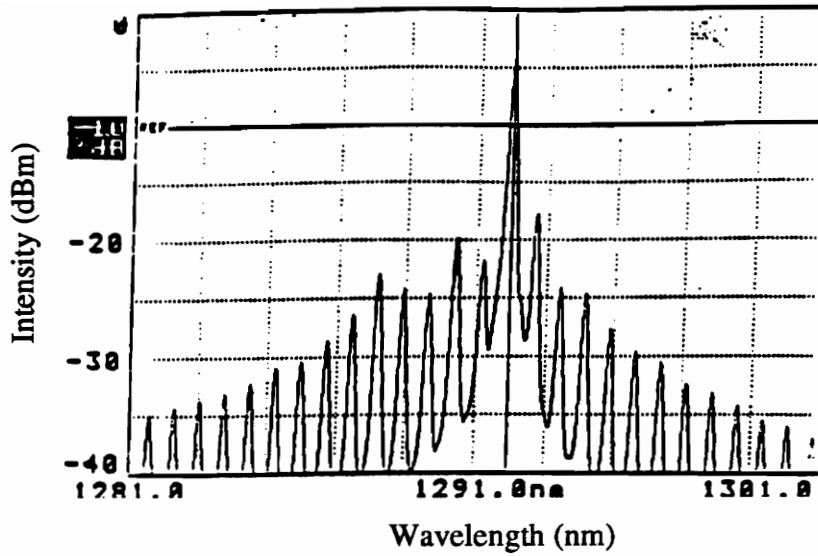
The unsuccessful attempt to modulate an LD to emit two distinct but closely spaced wavelengths led to the implementation of the dual laser TDM topology.

3.4 System Component Design

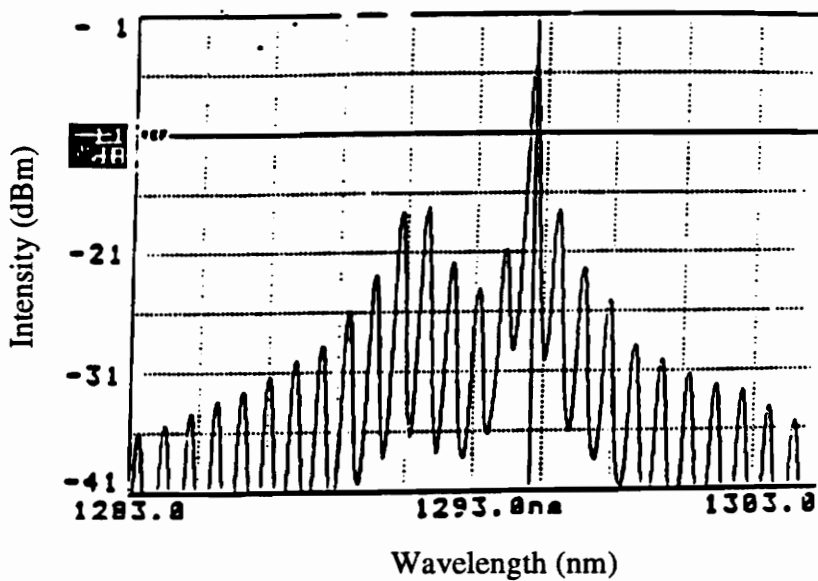
The block diagram of the dual laser TDM EFPI sensing system is illustrated in Figure 3.4. The electronic hardware developed has been designed to support real time interrogation of the Fabry-Perot cavity at a switching speed of up to 100 kHz. The electronic circuits were fabricated using breadboards. To minimize the effects of noise, the circuits should be mounted on printed circuit boards. The three basic components are the transmitter, the receiver, and the data acquisition circuit. This section presents an overview of different issues involving the design and selection of these components.

3.4.1 Transmitter

Each transmitter consists of a laser diode module and its drive circuitry. Two Mitsubishi



(a)



(b)

Figure 3.7 Optical emission spectrum of Mitsubishi 7011R LDs at a drive current of 20 mA. (a) LD whose peak wavelength is at 1291.93 nm (b) LD whose peak wavelength is at 1294.65 nm.

7011R LDs were selected as the optical sources for the system. Each LD was pulsed at a drive current where it appeared to behave like a singlemode LD with one distinct dominant peak. Coincidentally, this drive current turned out to be around 20 mA for both LDs. At this operating current, the peak wavelength for one laser was 1291.93 nm and the dominant mode was roughly 14 dB higher than the second most prominent mode. The peak wavelength of the other laser was observed at 1294.65 nm and the dominant mode was around 12 dB higher than the most significant side lobe. The emission spectrum of the two LDs are shown in Figure 3.7.

In the dual-laser TDM system, each source is pulsed and made to interrogate the sensor at distinct time instants. The time separation between the sources is achieved by alternately switching the sources on and off. If the optical signal produced by the two LDs, due to the on off keying (OOK) modulation are denoted as $S_1(t)$ and $S_2(t)$ respectively, then mathematically they can be written as

$$S_1(t) = \sum_{k=-\infty}^{\infty} \Pi \left[\frac{t - \left(\frac{\tau}{2} + kT_s \right)}{\tau} \right], \quad (3.8)$$

and,

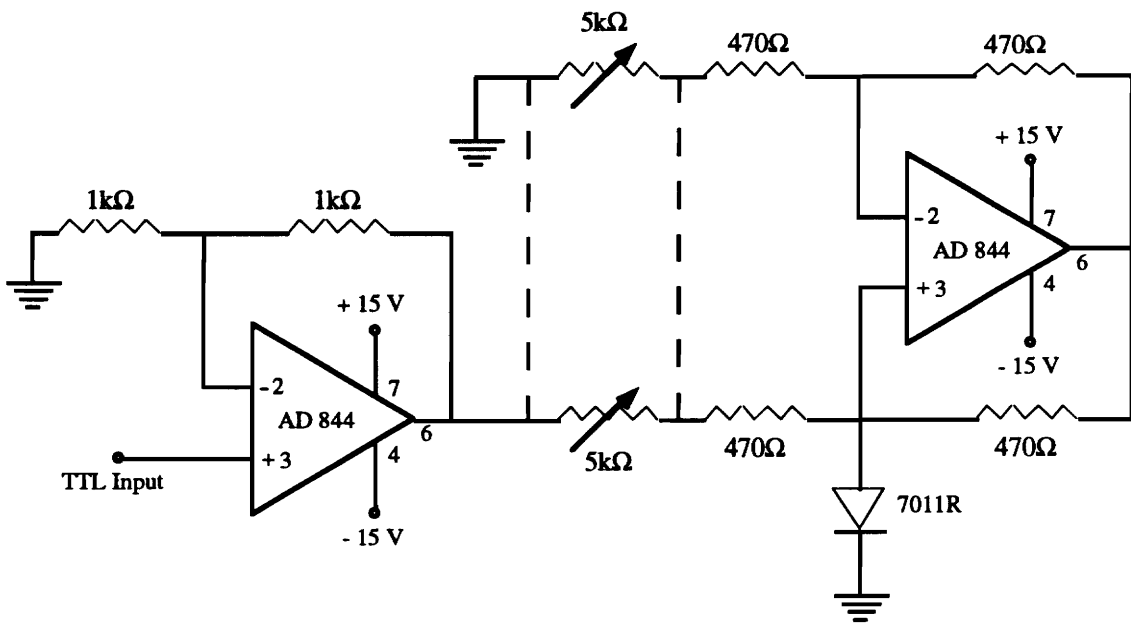
$$S_2(t) = \sum_{k=-\infty}^{\infty} \Pi \left[\frac{t - \left(\frac{3\tau}{2} + kT_s \right)}{\tau} \right], \quad (3.9)$$

where, τ is the pulse width, and T_s is the switching period. The quantity d , called the duty cycle, is a measure of the duration of the pulse with respect to the switching period. This is given by

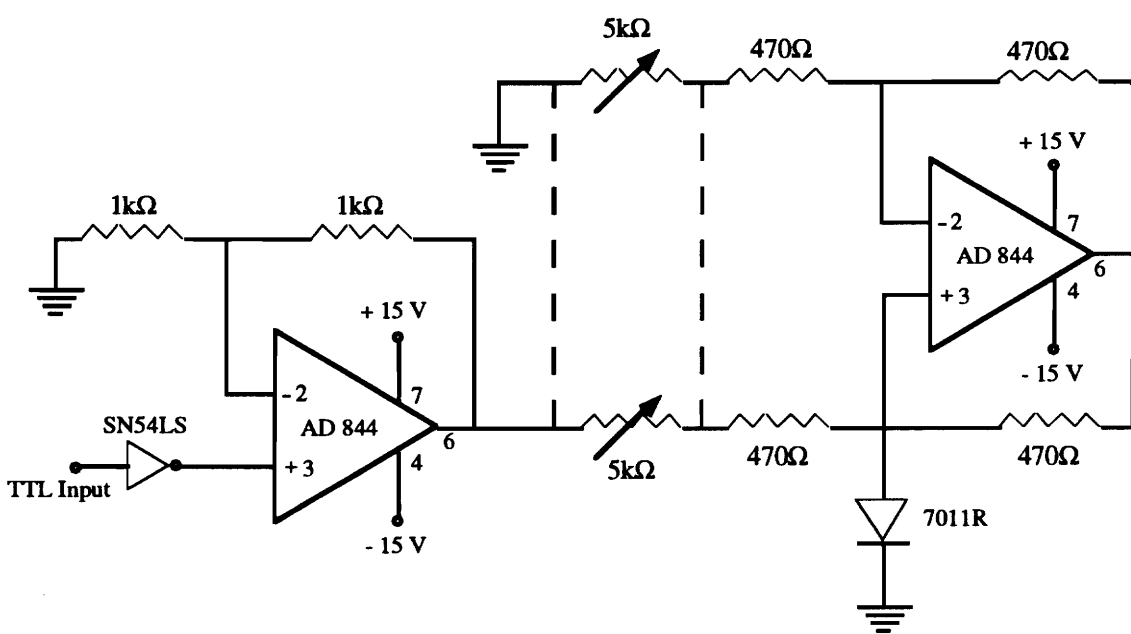
$$d = \frac{\tau}{T_s}. \quad (3.10)$$

For this system, the value for d was chosen as 1/2. Therefore, at each switching cycle (inverse of switching speed) each LD is alternately on for 1/2 the time.

The dual laser system requires two transmitter circuits, one for each source. Initially, the Mitsubishi 55610P laser driver chip, which is recommended for driving Mitsubishi R type LDs, was used to pulse the lasers. The chip turns the laser on and off corresponding to the high and low states of a TTL level input signal. Unfortunately, it was observed that the chip does not completely turn off its current source during the low state of the input, but supplies a current of around 10 mA to the source. This value is greater than the

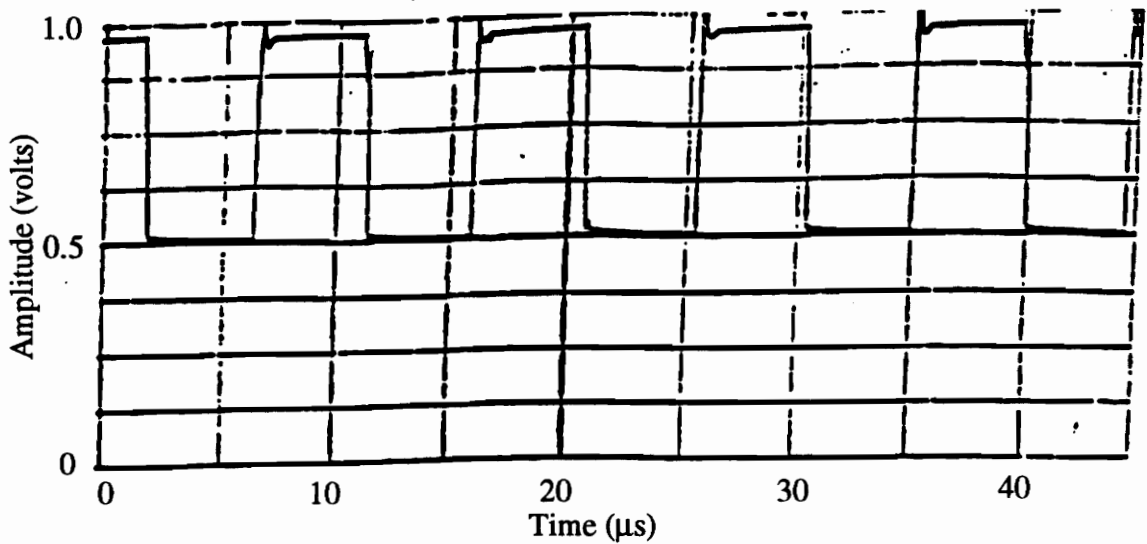


(a)

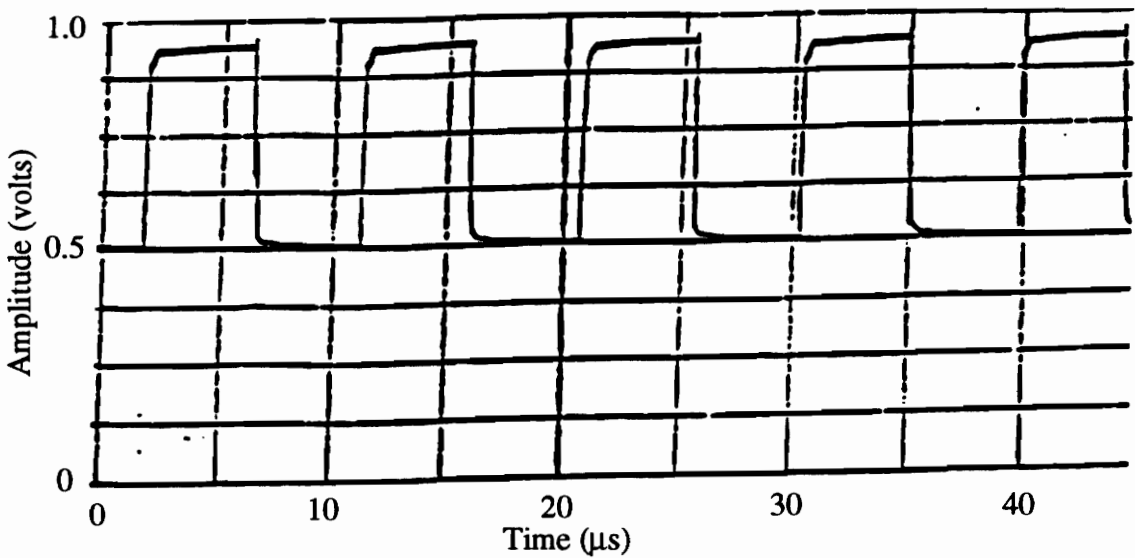


(b)

Figure 3.8 Schematics of the transmitters designed for the dual-laser TDM system. (a) transmitter that is in phase with the clock (b) transmitter that is out of phase with the clock.



(a)



(b)

Figure 3.9 Oscilloscope traces of the output wave forms of the transmitters monitored across a 47Ω load, at a switching speed of 100 kHz. (a) and (b) are respectively the outputs for the in phase and out of phase transmitters relative to the input clock.

threshold level for both 7011R lasers and it was not possible to alternately turn the LDs on and off with this chip. Therefore, we had to design our own driver circuit to modulate the lasers. A balanced bridge Howland current source was designed for this purpose. The current source requires a pulsed 10V input signal and provides pulsed output current of 2 mA to 20 mA that can be switched up to a speed of 100 kHz. To maintain proper synchronization between the transmitter and the analog to digital converter at the receiving end, the input signal to each driver circuit is provided by the data acquisition/timing circuit. This circuit can be configured to provide up to a 5V TTL signal. Thus, amplification of the reference signal is necessary before it can be supplied to the Howland circuit as input. One of the transmitter circuits, therefore, consists of two stages. The first stage is a non-inverting amplifier that amplifies the reference TTL level signal. The second stage of the circuit is the Howland current source. The other transmitter is comprised of three stages. The first stage is a NOT circuit that reverses the order of the on and off states of the reference input signal, ensuring the two lasers will be alternately modulated when the transmitters are excited by the reference signal. The second and third stages of this transmitter consists of the non-inverting amplifier and the Howland current source respectively. Figure 3.8 illustrates the schematics of the transmitter circuits.

The Analog Devices AD 844 monolithic operational amplifier (op-amp) was used to design both the Howland current sources and the non-inverting amplifiers. The features of this chip - wide bandwidth, high output slewrate, and high output drive current - makes it ideal for high speed current supply applications. The output wave forms of these circuits monitored across a 47 Ω resistive load (used to simulate an LD) is shown in Figure 3.9 at a switching speed of 100 kHz

3.4.2 Receiver

The output of the EFPI sensor is an analog signal. At the same time, the transmitters of the dual laser TDM system emit pulses to interrogate the EFPI sensor cavity. As a result, for each wavelength, the analog sensor output is converted into a pulse-type signal where the amplitude of the pulse denotes the analog information. The conversion results in a gated pulse amplitude modulation (PAM) of the sensor output. The analog-to-PAM conversion process is illustrated in Figure 3.10.

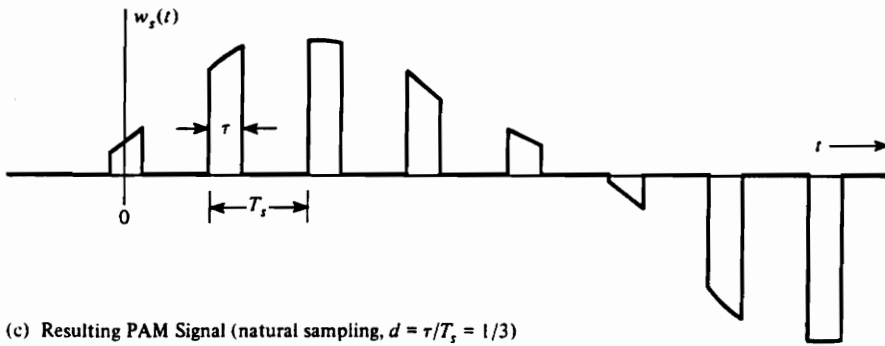
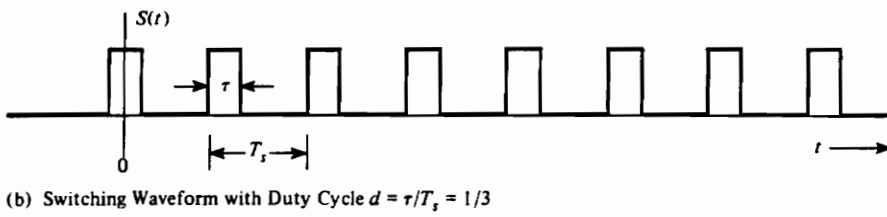
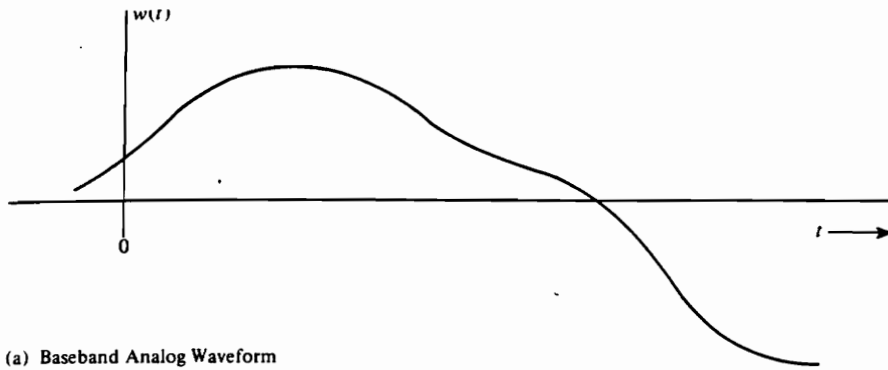


Figure 3.10 Illustration of analog-to-PAM conversion for a duty cycle of $d = 1/3$ [17].

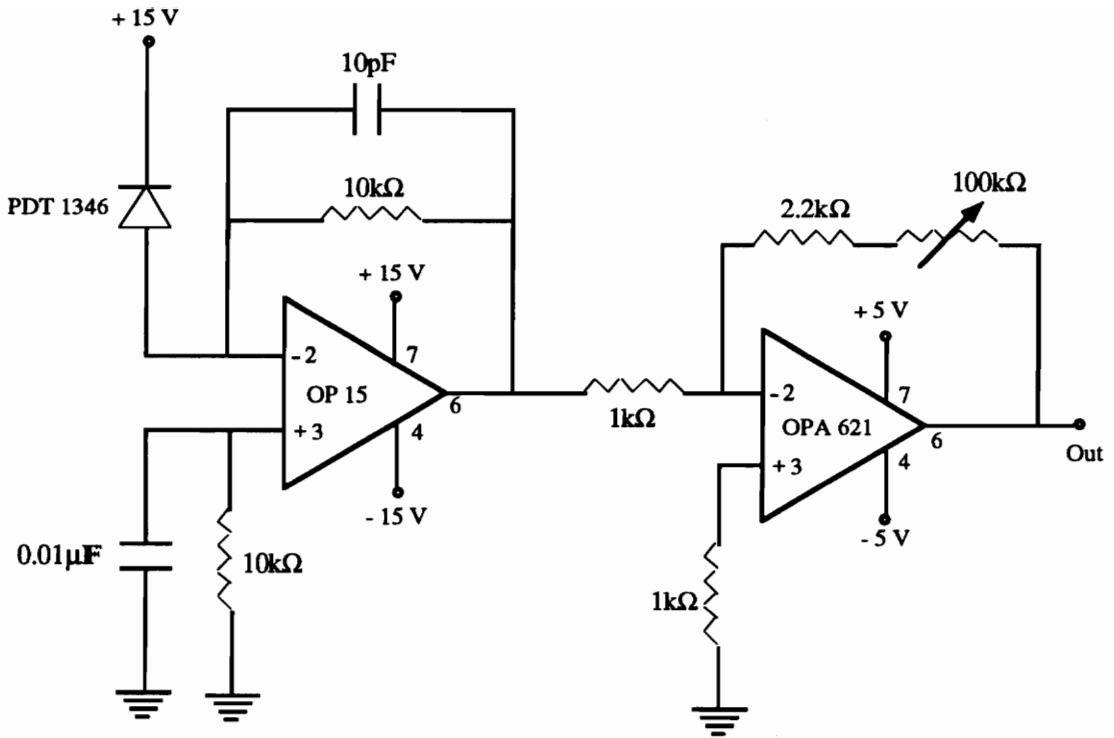


Figure 3.11 Schematic of the designed two stage receiver circuit.

Mathematically, if $w(t)$ is the EFPI output waveform, the PAM signal at the detector for each wavelength is given by [17]

$$w_{s1}(t) = w(t)S_1(t), \quad (3.11)$$

and,

$$w_{s2}(t) = w(t)S_2(t), \quad (3.12)$$

where $S_1(t)$ and $S_2(t)$ have been defined in Equations (3.8) and (3.9).

The spectrum of the PAM signal is found by taking the Fourier transform of Equation (3.11) or (3.12) and is given by [17]

$$W_{si}(f) = \frac{\tau}{T_s} \sum_{n=-\infty}^{\infty} \frac{\sin(\pi nd)}{\pi nd} W\left(f - \frac{n}{T_s}\right), \quad (3.13)$$

where $W_{si}(f)$, $W(f)$, and $S(f)$ are the Fourier transforms of $w_{si}(t)$, $w(t)$, and $S_i(t)$ respectively, and $i = 1, 2$.

Equation (3.13) implies that the bandwidth of the PAM wave form is much wider than that of the analog sensor output. Therefore, the receiver circuit must have a much wider bandwidth than those used in regular EFPI systems. The bandwidth of the PAM signal is governed by the first zero crossing of the expression in Equation (3.13). The zero crossing occurs at $1/\tau$. Thus, the receiver bandwidth in the dual laser TDM system should be

$$B_{rec} > \frac{1}{\tau}. \quad (3.14)$$

The pulse width of the system for the maximum switching speed of 100 kHz is 5 μ s. Thus, the receiver bandwidth should be much greater than 200 kHz.

A two stage receiver circuit was designed and fabricated for this system. The schematic of the receiver is shown in Figure 3.11. The bandwidth of the receiver is inversely proportional to the junction capacitance of the photodiode. Therefore, low junction capacitance photodiodes are required to design wideband receivers. A Hewlett Packard PDT 1346 pigtailed InGaAs pin photodiode has been used in the photoconductive mode. This photodiode has a low junction capacitance of 1.1 pf and a responsivity of 0.7 A/W. The first stage of the receiver is the transimpedance stage. The PDT 1346 needs to see a high input impedance. An Analog Devices FET-Input OP 15 op-amp, which has an input impedance in the order of $10^{12} \Omega$ has been used at this stage. The small bias current

(± 15 pA) of the op-amp helps to achieve the highest sensitivity. A small amount of capacitance (10 pf) across the feedback resistor (the 10 k Ω resistor across OP 15) is required to suppress oscillations and to ensure loop stability, although it affects bandwidth. The second stage is used to increase the gain of the circuit. A Burr Brown OPA 621 wide band precision op-amp is used in an inverting voltage amplifier configuration. The op-amp is frequency compensated. It has an extremely high unity gain bandwidth of 500 MHz, and is stable for gains ≥ 2 V/V. The design of the receiver involves a tradeoff between gain (or sensitivity) and bandwidth. A high gain is required to amplify the low power optical signal, while a high bandwidth is required to accommodate the fast rise and fall times of PAM. Although the receiver consists of two stages, the bandwidth is governed by the transimpedance stage, and is given by

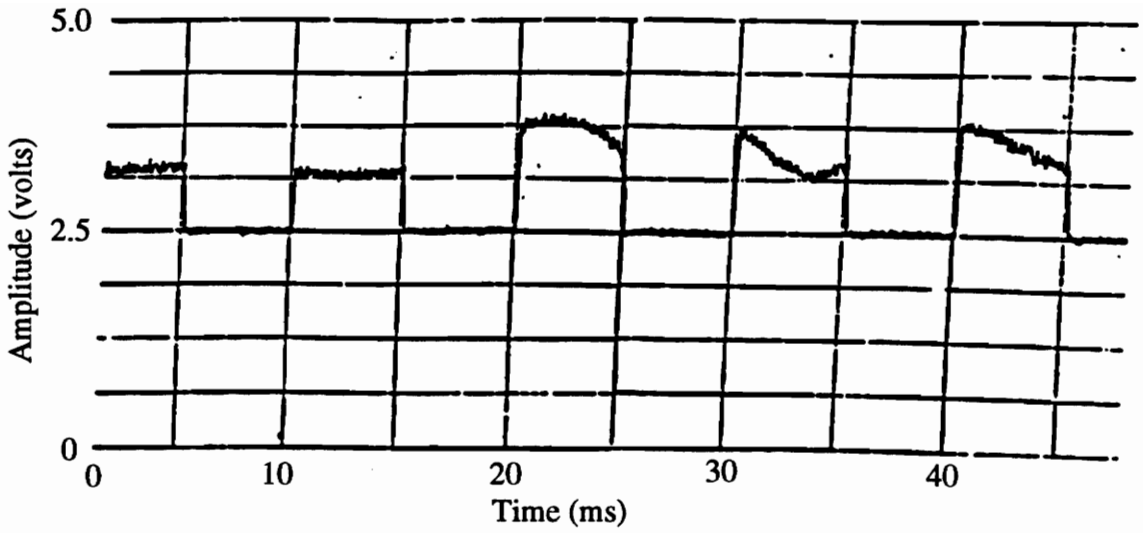
$$B_{\text{rec}} = \frac{1}{2\pi RC}, \quad (3.15)$$

where $R = 10$ k Ω and $C = 10$ pf. Thus, the receiver bandwidth is 1.6 MHz. The gain of the circuit is 7.0×10^5 V/W. The output PAM waveforms for $\lambda_1 = 1291.93$ and $\lambda_2 = 1294.65$ is shown in Figure 3.12(a) and (b) respectively for switching speed of 100 Hz. In actuality the two wave forms appear as a TDM signal at the detector. These plots were taken with only one laser being operated at a time, so that the phenomenon of the analog sensor output modulating the transmitter pulse for that laser can be seen.

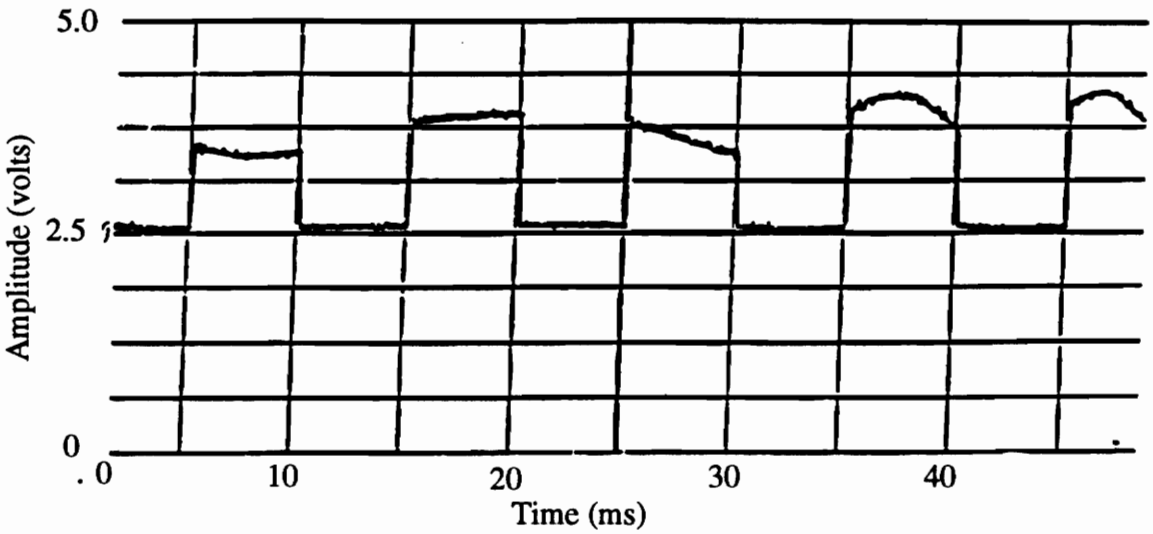
3.4.3 Data Acquisition

The data acquisition component of the system comprises a 486-33 MHz PC and National Instruments' AT-MIO-16E-2 (E2) high-speed data acquisition card. The E2 is a 12-bit data acquisition system (DAQ) which can be configured for a 10V bipolar input. This format provides for 4096 discrete levels with a bit resolution of 2.44 mV/bit (10V/4096). For our application, the card was configured for a 5V input. This configuration reduces the number of discrete levels to 2048, but does not change the resolution (5V/2096). The DAQ software was written in standard ANSI C 32-bit format and is compatible with Microsoft Windows [18].

The E2 card provides functions for outputting the timing signal and data acquisition of two channels. Essentially, the user selects the desired rate of acquisition in samples per second (sps), up to 100 kHz, and the software generates a 5V TTL timing square wave. This is used as the reference input signal to drive the two transmitters. At the same time, data is sampled at the detector output at $0.3 T_s$ and $0.8 T_s$ of the timing square wave,



(a)



(b)

Figure 3.12 Oscilloscope traces of the PAM waveforms at the detector at a switching speed of 100 Hz. (a) detected signal when LD that has a peak wavelength of 1291.93 is on (b) detector output when LD with peak wavelength at 1294.65 is being operated.

where T_s is the switching period. This conversion methodology was selected so that the transients associated with switching the lasers on and off had fallen to negligible levels.. Thus, data is sampled at both the high and low states of the timing signal. The samples for the high state (corresponding to λ_1) is sent to channel one, while the samples for the low state (corresponding to λ_2) is sent to channel two. The user has the option of either having the sensor output displayed on the computer monitor for real time observation, or stored in a data file for post processing. For example, for an acquisition of 2500 sps, the corresponding switching period, T_s , is 400 μ s. If we reference the transition of the input signal from high to low as 0 μ s, then the first sample occurs at $0.3 \times 400 \mu$ s = 120 μ s, and becomes channel 1 data. At $0.8 \times 400 \mu$ s = 320 μ s, data for the second channel is sampled. This process continues until the clock generation is terminated.

Chapter 4 - Derivation of System Parameters

This chapter provides the theoretical analysis used to derive the different parameters of the dual laser TDM sensing system. The performance of any sensing system is judged based on these parameters. The parameters in question are: signal-to-noise ratio (SNR), strain range, strain rate and strain resolution.

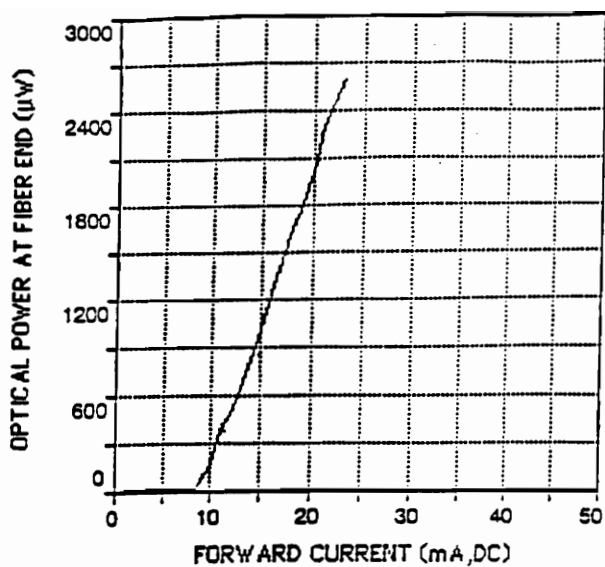
4.1 Power Budget

To calculate the SNR of the system, we must know the optical power due to the interference signal from the extrinsic Fabry-Perot interferometer (EFPI) that is incident on the detector. Since the system employs two sources, a separate power budget analysis can be done for each source. However, we will pick the lower powered laser diode (LD), since this source sets the lower limit on the SNR that can be achieved by the system. Both optical sources used in the system are Mitsubishi 7011R LDs. The characteristic plot of output power versus drive current for both these LDs is shown in Figure 4.1. Characterization tests revealed that the best spectral performance from each source (when the laser displays the best single mode characteristics) is achieved when it is operated at a current of 20 mA. According to Figure 4.1, at 20 mA, the lasers emit around 2.3 and 2.1 mW of power respectively. Thus, the output power of the second laser will be used for calculating the SNR of the system.

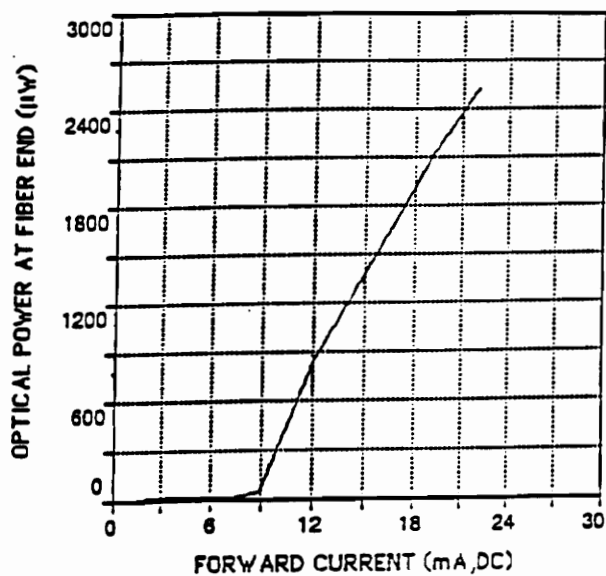
The main contributors to the loss in the system are splice tubes and couplers. We assume that both wavelengths encounter an equal amount of loss from these devices. In the forward path the optical signal from each LD goes through 2 couplers and 3 splice tubes. The sensor output for each wavelength encounters 1 coupler and 2 splice tubes in the reverse path. The fiber losses are not significant for the distances in the system.

A major source for the loss of power in the system is the sensor itself. In this system, the EFPI is used in the reflection mode. The reflection coefficient between the glass-air interface (reference reflection), and the air-glass interface (second reflection) is given by

$$r = \frac{(n_f - 1)^2}{(n_f + 1)^2}, \quad (4.1)$$



(a)



(b)

Figure 4.1 Power output versus forward current for Mitsubishi 7011R LDs. (a) LD with peak wavelength at 1291.93 nm (b) LD with peak wavelength at 1294.65 nm.

where, n_f is the refractive index of the fiber. Using a value of 1.47, the reflection coefficient can be calculated as 0.036 or 3.6 %. Moreover, losses also occur inside the cavity due to the air gap separation of the two end faces.

The detected intensity of an EFPI output is of the form,

$$I_{\text{det}} = I_{\text{dc}} + I_{\text{ac}} \cos(\Delta\phi). \quad (4.2)$$

We will only consider the intensity contribution of the sinusoidal variation to the detected intensity, since this is due to the interference between the reference and sensing reflections. This contribution can be calculated as

$$\Delta I_{\text{det}} = \max I_{\text{det}} - \min I_{\text{det}} = 2I_{\text{ac}}. \quad (4.3)$$

Based on Equation (2.11), we can express this term as

$$\Delta I_{\text{det}} = 2I_{\text{ref}} \left(\frac{2ta}{a + 2d \tan[\sin^{-1}(NA)]} \right), \quad (4.4)$$

where I_{ref} is the optical power of the reference reflection, 'a' is the fiber core radius, 't' is the transmissivity of the interface (1 - r), 'd' is the length of the air gap, and NA is the numerical aperture of the singlemode fiber given by Equation (2.12). For a system without any coupler or connector losses, I_{ref} can be expressed as

$$I_{\text{ref}} = rP_{\text{in}}, \quad (4.5)$$

where P_{in} is the input power launched by the LD. For the worst case scenario, we pick the maximum air gap length permitted in the system. Using Equations (3.5), (3.6), and (3.7) we can express this gap length as

$$d = d_{\text{bias}} + \Delta d_{\text{max}} = \frac{(2n + 2)\lambda_1\lambda_2}{8\Delta\lambda}. \quad (4.6)$$

Using Equations (4.4), (4.5), (4.6) and the following values: $P_{\text{in}} = 2.1$ mW, $a = 9$ μm , $n = 0.036$, $t = 0.964$, $NA = 0.25$, $n = 0$, $\lambda_1 = 1291.9$ nm, and $\lambda_2 = 1294.65$ nm; ΔI_{det} is calculated as 0.029 mW or -15.3 dBm.

The received power at the detector due to the perturbation is then given by

$$P_{\text{rec}} = \Delta I_{\text{det}} - 3l_c - 5l_s, \quad (4.7)$$

where l_c and l_s are coupler and splice tube losses respectively. We assume each coupler has a loss of 4 dB (including excess loss) and each splice tube has a loss of 0.5 dB. The received power, P_{rec} , is then -30 dBm or 1 μW .

The receiver current due to the sensor signal is given by

$$I_p = RP_{rec} , \quad (4.8)$$

where R is the responsivity of the receiver. The PDT 1346 has a responsivity of 0.7. Thus, the receiver current is

$$I_p = 7 \times 10^{-7} \text{ Amp} . \quad (4.9)$$

4.2 Noise Mechanisms in the System

Noise in the dual laser TDM system is caused by various phenomena. All three hardware components - the transmitter, receiver, and data acquisition (DAQ) - contribute to the noise effects of the system. Detailed analysis of transmitter and receiver noise mechanisms is given in [19].

4.2.1 Transmitter Noise

The output of a semiconductor LD exhibits fluctuations in its intensity, phase, and frequency even when its is biased at a constant current. Spontaneous emission and electron-hole recombination (shot noise) are the two fundamental noise mechanisms in a semiconductor laser diode. In general, noise in a semiconductor LD is dominated by spontaneous emission. Intensity fluctuations degrade the signal-to-noise ratio (SNR) whereas phase fluctuations broaden the spectral linewidth of the laser [19].

4.2.1.1 Intensity Noise

Variation of the laser intensity due to spontaneous emission gives rise to relative intensity noise (RIN). Intensity noise at the transmitter causes current fluctuations at the receiver. This adds to the noise generated by the receiver and further degrades SNR. The variance of the RIN can be expressed as

$$\langle i_{RIN}^2 \rangle = r_I^2 I_p^2 , \quad (4.10)$$

where r_I^2 is given by

$$r_I^2 = \frac{1}{2\pi} \int_{-\infty}^{\infty} RIN(\omega) d\omega = r_{in} B_{rec} . \quad (4.11)$$

The RIN of a laser is specified in units of dB/Hz. The quantity r_{in} can be calculated from

$$10 \log_{10}(r_{in}) = RIN . \quad (4.12)$$

The term B_{rec} in Equation (4.11) represents the receiver bandwidth.

The EFPI is a reflection mode sensor where the back reflection from the sensor cavity carries the output information. A portion of the signal may get reflected back into the laser cavity. The reflection is further increased if reflective coatings are deposited on the fiber endfaces. Moreover, in optical systems some light is reflected back into the laser cavity due to discontinuities at the splices. These back reflections convert the inherent phase noise in the laser to intensity noise, or RIN [20]. Therefore, it is necessary to minimize any light reflected back into the laser. RIN may be expected to be as low as -150 dB/Hz if reflections are kept below -50 dB, or as high as -100 dB/Hz for reflections on the order of -20 dB [21]. Using optical isolators at the laser output is a common solution to this problem. Both LDs used in the system are optically isolated and a laser RIN of -130 dB/Hz has been assumed in intensity noise calculations. Using a value of 1.6×10^6 for B_{rec} , and 1×10^{-13} for RIN, the term for RIN is calculated to be

$$\langle i_{RIN}^2 \rangle = 7.84 \times 10^{-20} \text{ Amp}^2. \quad (4.13)$$

4.2.2 Receiver Noise

The receiver used in this system is a pin detector-transimpedance amplifier module. At the receiver, the detected power P_{rec} is transformed through the photodiode into electrical current, is converted to voltage by the transimpedance amplifier stage. Two fundamental noise mechanisms, shot noise and thermal noise, lead to current fluctuations at the detector even for a constant incident optical power at the detector.

4.2.2.1 Shot Noise

Shot noise is generated at the receiver due to the random nature of electrons that make up the detector current. The photodiode current generated in response to a constant optical signal can be expressed as,

$$I(t) = I_p + i_s(t), \quad (4.14)$$

where $i_s(t)$ is the current fluctuation related to shot noise. These current fluctuations is a stationary random process with Poisson statistics which can be approximated by Gaussian statistics [19]. The variance of shot noise is given by

$$\langle i_{sh}^2 \rangle = 2q I_p B_{rec}, \quad (4.15)$$

where q is the charge of an electron. All photodiodes also generate some current in the absence of light known as dark current. Therefore, the accurate representation of shot noise is

$$\langle i_{sh}^2 \rangle = 2q (I_p + I_d) B_{rec}, \quad (4.16)$$

where i_d is the dark current. The PDT 1346 has a rated I_d of 1 nA. The variance of shot noise is then

$$\langle i_{sh}^2 \rangle = 3.59 \times 10^{-19} \text{ Amp}^2. \quad (4.17)$$

4.2.2.2 Thermal Noise

Random thermal motion of electrons in the resistors of the amplifier in the receiver also cause fluctuations in the detector current and give rise to thermal noise. Thermal noise is included by modifying Equation (4.16) as

$$I(t) = I_p + i_s(t) + i_T(t), \quad (4.18)$$

where $i_T(t)$ is the contribution of the thermal noise. It is mathematically modeled as a stationary Gaussian random process that is frequency independent up to 1 THz [19]. The receiver designed for the system has two stages. The receiver thermal noise is given by

$$\langle i_{th}^2 \rangle = \langle i_{th}^2 \rangle_{1st \text{ stage}} + \frac{\langle i_{th}^2 \rangle_{2nd \text{ stage}}}{G}, \quad (4.19)$$

where $\langle i_{th}^2 \rangle_{1st \text{ stage}}$ and $\langle i_{th}^2 \rangle_{2nd \text{ stage}}$ are the current noise referred to the input of the first and second stages respectively, and G is the gain of the first (transimpedance) stage. The second term in Equation (4.19) can be neglected since the gain of the first stage is very high. Therefore, the variance of the thermal noise for the receiver is approximately equal to the thermal noise variance of the transimpedance stage. This is given by

$$\langle i_{th}^2 \rangle = \frac{4kTB_{rec}}{R_e}, \quad (4.20)$$

where k is the Boltzmann's constant, T is the room temperature in Kelvin, and R_e is the effective resistance. We see from Equation (4.20) that thermal noise is additive and is present even in the absence of an optical signal. The noise effects of the amplifier can be accounted for by including a quantity F_n , referred to as the amplifier noise figure. It represents the factor by which thermal noise is enhanced by the amplifier [19]. Equation (4.20) is then rewritten as

$$\langle i_{th}^2 \rangle = \frac{4kTB_{rec}F_n}{R_e}. \quad (4.21)$$

The effective resistance R_e in the transimpedance stage is 10 k Ω , the room temperature is 300 K, and the amplifier noise figure is assumed to be 10 dB or 10. Therefore, the variance of the current fluctuations due to thermal noise is

$$\langle i_{th}^2 \rangle = 2.65 \times 10^{-17} \text{ Amp}^2. \quad (4.22)$$

Note that thermal noise is the dominant source of noise in the system.

4.2.3 SNR at the Detector

The previous sections described the optical power received at the detector and the various noise mechanisms present at the detector. Based on this discussion we can calculate the SNR at the receiver of the system. The SNR is defined as

$$\text{SNR} = \frac{\text{signal power}}{\text{noise power}} = \frac{I_p^2}{\sigma^2}. \quad (4.23)$$

The quantity σ is the noise variance. The total current noise is found by adding the contributions of all the noise sources. The individual current fluctuations are independent random processes with Gaussian statistics. As a result, the total variance of the current fluctuations obtained by simply adding the individual variances [19]. Therefore,

$$\sigma^2 = \langle i_{\text{RIN}}^2 \rangle + \langle i_{\text{sh}}^2 \rangle + \langle i_{\text{th}}^2 \rangle. \quad (4.24)$$

From Equations (4.9), (4.13), (4.17), (4.22), and (4.23) the SNR at the detector is calculated as

$$\text{SNR}_{\text{det}} \cong 42.6 \text{ dB}. \quad (4.25)$$

4.2.4 Quantization Noise

After the receiver, the next stage of the dual laser TDM system is the DAQ. The DAQ samples the pulse amplitude modulated analog sensor output for each wavelength, and converts it to discrete amplitude levels. This procedure is known as quantization. Once quantized, the instantaneous values of the continuous signal can never be reconstructed exactly. The errors introduced are called quantization noise. In contrast to the other noise mechanisms described above, the quantization noise is artificially generated and can be reduced to a desired level by choosing the number and distribution of the quantizing levels. A detailed analysis for computing the SNR due to quantization is given in [22].

The SNR due to quantization is given by

$$\text{SNR}_{\text{quant}} = \frac{E[x^2]}{D}, \quad (4.26)$$

where $E[x^2]$ is the mean-square signal after quantization and D is the measure of the mean-square error by quantization. If the input signal is quantized into n levels, each

spaced by an amplitude increment of a ; and if we assume that the signal has an uniform probability density function, then SNR_{quant} (in dB) can be expressed as [22]

$$SNR_{\text{quant}} = 4.8 + 20\log_{10}(n). \quad (4.27)$$

The AT-MIO-16E-2 is a 12-bit DAQ which can be configured for a 10V bipolar input. Thus, it has $n = 2^{12} = 4096$ levels. However, for our application we configured it for an input of 0 to 5V. As a result, the number of levels is reduced to 2048. Using Equation (4.24) we can compute the SNR_{quant} for the system to be

$$SNR_{\text{quant}} \approx 71 \text{ dB} . \quad (4.28)$$

4.2.5 Overall SNR

The theoretical overall SNR for the worst case scenario then is given by

$$SNR_{\text{out}} = \frac{1}{\frac{1}{SNR_{\text{det}}} + \frac{1}{SNR_{\text{quant}}}} , \quad (4.29)$$

where SNR_{det} and SNR_{quant} are expressed in ratios. Based on Equations (4.25) and (4.28) this is calculated as

$$SNR_{\text{out}} \approx 42 \text{ dB} . \quad (4.30)$$

The rest of this chapter concentrates on deriving expressions for the different system parameters related to strain, namely strain range, strain rate and strain resolution.

4.3 Determining Strain Range

The strain range of the system is directly proportional to the operating range of the sensor in terms of gap length. If the sensor bias point is chosen for equal dynamic range in both directions (tension and compression), then the expression for maximum allowable displacement of the Fabry-Perot cavity, Δd_{max} , from the bias point is given by Equation (3.7). For an EFPI sensor, the relationship between strain, ϵ , and the change in cavity length, Δd , is given by

$$\epsilon = \frac{\Delta d}{g} , \quad (4.31)$$

where g is the gage length of the sensor. The typical gage length of an EFPI is around 4-5 mm.

From Equation (3.7) and (4.31), we can express the strain range of the system as,

$$\epsilon_{\text{range}} = \pm \frac{\Delta d_{\text{max}}}{g} = \pm \frac{\lambda_1 \lambda_2}{8g\Delta\lambda}. \quad (4.32)$$

4.3.1 Effect of Laser Wavelength Instability on Strain Range

A sensing system operating based on dual wavelength interrogation of the Fabry-Perot cavity using two separate sources requires very high stability between the two sources. However, longitudinal modes of a laser diode will change absolute wavelength at the rate of 0.006 nm/°C due to the change of index of refraction and length expansion of the active material with temperature [19]. Moreover, the imposed frequency chirp on the lasers due to intensity modulation will cause the peak emission wavelengths of the lasers to vary. The instability in the emitted peak wavelengths of the LDs results in a change in the strain range of the system. The effect of this instability can be analyzed by assuming that the quantity Δd_{max} in Equation (4.32) changes by $\Delta(\Delta d_{\text{max}})$ due to a change of $\Delta\lambda_1$ and $\Delta\lambda_2$ in laser wavelengths. The change in the strain range, $\Delta\epsilon_{\text{range}}$ can be expressed as

$$\Delta\epsilon_{\text{range}} = \frac{1}{8g} \left[\frac{\Delta\lambda_1 \lambda_2 + \Delta\lambda_2 \lambda_1}{\Delta\lambda_n} \right], \quad (4.33)$$

where $\Delta\lambda_n = |\Delta\lambda_1 - \Delta\lambda_2|$. Since both LDs are of the same type (Mitsubishi 7011R) we can assume that they both experience the same amount of shift in wavelength, i.e. $\Delta\lambda_1 = \Delta\lambda_2 = \Delta\lambda_{\text{shift}}$. Then we can manipulate Equation (4.33) to show that $\Delta\epsilon_{\text{range}}$ is given by

$$\Delta\epsilon_{\text{range}} = \frac{1}{8g} \Delta\lambda_{\text{shift}} \left[\frac{\lambda_1 + \lambda_2}{\Delta\lambda} \right]. \quad (4.34)$$

A negative shift in peak wavelength will reduce the strain range of the sensor. On the other hand, although a positive shift will increase the strain range, it will lead to erroneous calculation of applied strain.

4.4 Determining Strain Rate and Resolution

In this dual wavelength strain sensing system, the detected sensor output for each wavelength is sampled by the DAQ at the same rate as the switching speed of the laser diodes. Thus, the maximum measurable strain rate and the corresponding strain resolution are dependent on the sampling rate and the signal processing techniques that are employed. It is intuitive that the higher the sampling rate, the higher strain rate can be measured by the system. Also, for a given strain rate, the strain resolution can be

improved by increasing the sampling rate. In the following discussion two different methods for calculating the strain rate and strain resolution are presented.

4.4.1 Signal Reconstruction by Plotting DAQ Samples

Equation (4.31) gives us a relationship between strain, ϵ , and the displacement of the cavity from the bias point, Δd . For an EFPI the strain is directly related to the number of fringes that occur when the cavity length is changed. The output intensity goes through a fringe when the path difference between the two reflections is a multiple of the wavelength, λ . The transmitted light at the first interface traverses the length of the cavity twice. Therefore, a fringe occurs whenever there is a $\lambda/2$ change in the cavity length. The total change in gap length, Δd , in any direction can be expressed as [23]

$$\Delta d = \left(\frac{\lambda}{2}\right) \times (\text{number of fringes}). \quad (4.35)$$

For a given strain rate, if we decide to have N samples per fringe, and if our sampling rate is f_s , then we can write

$$f_s = Nf_r, \quad (4.36)$$

where f_r is the fringe rate, i.e. the number of fringes that occur in one second. From Equations (4.31), (4.35), and (4.36) we can derive the relationship between the strain rate, ϵ_{rate} , and sampling rate, f_s , as

$$\epsilon_{\text{rate}} = \frac{f_s \lambda}{2Ng}. \quad (4.37)$$

The strain resolution for the above strain rate in a noise free system is then given by

$$\epsilon_{\text{res}} = \frac{\lambda}{2Ng}. \quad (4.38)$$

If we incorporate the effect of noise then the expression for strain resolution becomes

$$\epsilon_{\text{res}} = \frac{\lambda}{2Ng} + \frac{\left(\frac{\lambda}{2Ng}\right)}{\text{SNR}}, \quad (4.39)$$

It is evident that to directly reconstruct the actual analog sensor output from the sampled PAM wave form, numerous samples must be taken within a fringe.

Equations (4.37) and (4.38) reveal a fundamental trade off between strain rate and strain resolution. For a given sampling rate, the system is capable of measuring a higher strain rate if the number of samples per fringe is lowered. However, lowering the number of samples per fringe will lead to a worsened strain resolution. On the contrary, the strain

resolution can be improved by increasing the number of samples per fringe, at the expense of reducing the maximum measurable strain rate.

4.4.2 Signal Reconstruction Through Interpolation

The method of recovering the sensor output by plotting the DAQ samples relies on oversampling the signal to a degree where the difference between the sampled wave form and the analog output can be considered negligible. However, by employing digital signal processing (DSP) techniques, we can avoid oversampling the detector signal and still reconstruct the output wave form. Avoiding oversampling of the signal implies that for a given sampling rate the measurable strain rate by the system can be increased, without compromising the strain resolution.

The Sampling theorem (also known as Nyquist's theorem) states that a continuous time signal can be completely recovered from its samples if, and only if, the sampling rate is greater than twice the signal bandwidth [24]. If an analog output is bandlimited to B Hz, then the rate at which it should be sampled to prevent aliasing, according to the Sampling theorem is

$$f_s > 2B, \quad (4.40)$$

where $f_s = 1/T_s$. T_s for our system is the switching period of the LDs.

Sampling the analog sensor output at or higher than the Nyquist rate, preserves the original spectrum of the signal. The time domain version of the sampled signal, however, does not look anything like the analog wave form. A technique by which reconstruction of the analog signal is performed from the sampled discrete-time signal is interpolation. Interpolation is a process by which the effective sampling rate of a signal is increased by an integer factor, L. However, instead of increasing the sampling rate at the DAQ, this rate conversion is done entirely by means of DSP after the analog signal is sampled [24]. Extensive analysis of interpolation has been done in [24] and [25]. Here, we will just discuss the significant aspects of the theory behind this procedure.

A method by which a discrete-time representation of a continuous-time signal can be obtained is known as periodic sampling, wherein a sequence of samples $x[n]$ is obtained from a continuous-time signal $x_c(t)$ according to the relation[25]

$$x[n] = x_c(nT_s), \quad -\infty < n < \infty. \quad (4.41)$$

The objective of interpolation is to obtain samples such that the the sampling rate of $x[n]$ is increased by L [25]. This procedure can be expressed as

$$x_i[n] = x_c(nT_s'), \quad (4.42)$$

where $T_s' = T_s/L$.

Figure 4.2 shows the interpolation system. The stage on the left is called a sampling rate expander. Its output is [25]

$$x_e[n] = \begin{cases} x[n/L], & n=0, \pm L, \pm 2L, \dots \\ 0, & \text{otherwise} \end{cases} \quad (4.43)$$

or,

$$x_e[n] = \sum_{k=-\infty}^{\infty} x[k]\delta[n - kL] \quad (4.44)$$

The stage on the right is a low pass discrete-time filter . It has a cut-off frequency of π/L and a gain L .

The operation of interpolation is illustrated in the time domain in Figure 4.3. The input sequence $x[n]$ with sampling rate f_s is depicted by circles in Figure 4.3(a). Figure 4.3(b) shows the output of the expander, $x_e[n]$, for $L = 2$. The desired output, $x_i[n]$, with sample rate $f_s' = 2f_s$ is represented by circles and dots Figure 4.3(c).

Interpolation can be understood better in the frequency domain. Figure 4.4(a) shows the Fourier transform, $X_c(j\Omega)$, of a bandlimited signal, where the bandwidth of the signal is Ω_n . Figure 4.4(b) illustrates the discrete-time Fourier transform, $X_n(e^{j\omega})$, of the sampled signal $x[n]$, where $\Omega_n = \pi/T_s$. The Fourier transform of the expander output signal, $X_e(e^{j\omega})$, is shown in Figure 4.4(c). To get from $X_n(e^{j\omega})$ to $X_e(e^{j\omega})$ we must process $X_n(e^{j\omega})$ as if the sampling rate were $\omega_s' = L\omega_s$, not ω_s . The increase in sampling rate is achieved by inserting $L-1$ zeros ($L = 2$ for this example) between each pair of samples $x[n]$ and $x[n-1]$. This does not change the spectrum $X_n(e^{j\omega})$, but only frequency scales it [24]. Mathematically, the Fourier transform of $x_e[n]$ can be expressed as [25]

$$X_e(e^{j\omega}) = \sum_{n=-\infty}^{\infty} \left(\sum_{k=-\infty}^{\infty} x[k]\delta[n - kL] \right) e^{-j\omega n} \quad (4.45)$$

or,

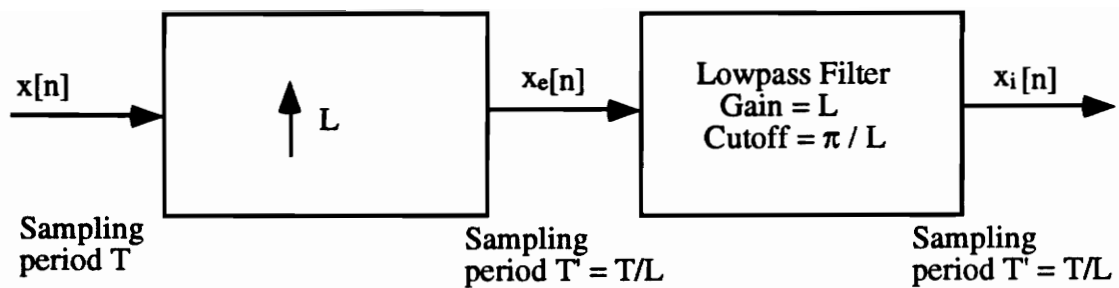
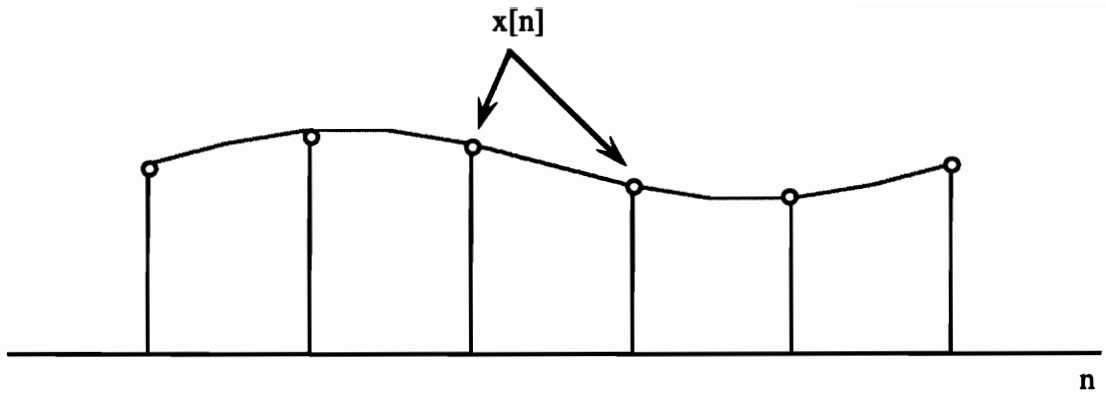
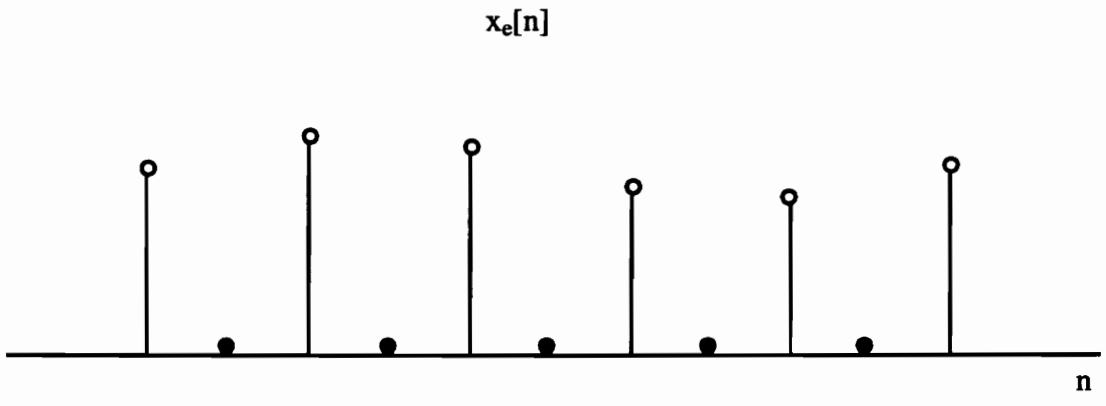


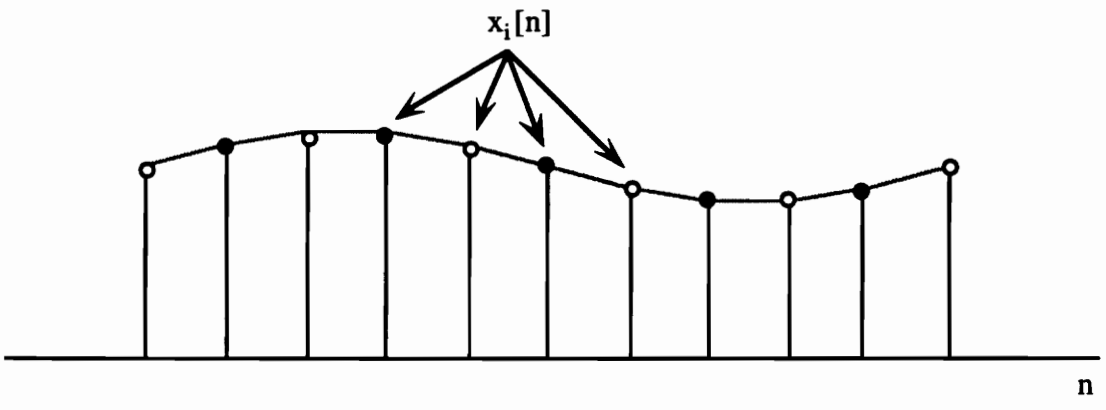
Figure 4.2 An interpolation system to increase sampling rate by L .



(a)



(b)



(c)

Figure 4.3 Time domain illustration of interpolatoin. (a), (b), and (c) represent the input sequence $x[n]$, the expander output $x_e[n]$, and the desired output $x_i[n]$ respectively.

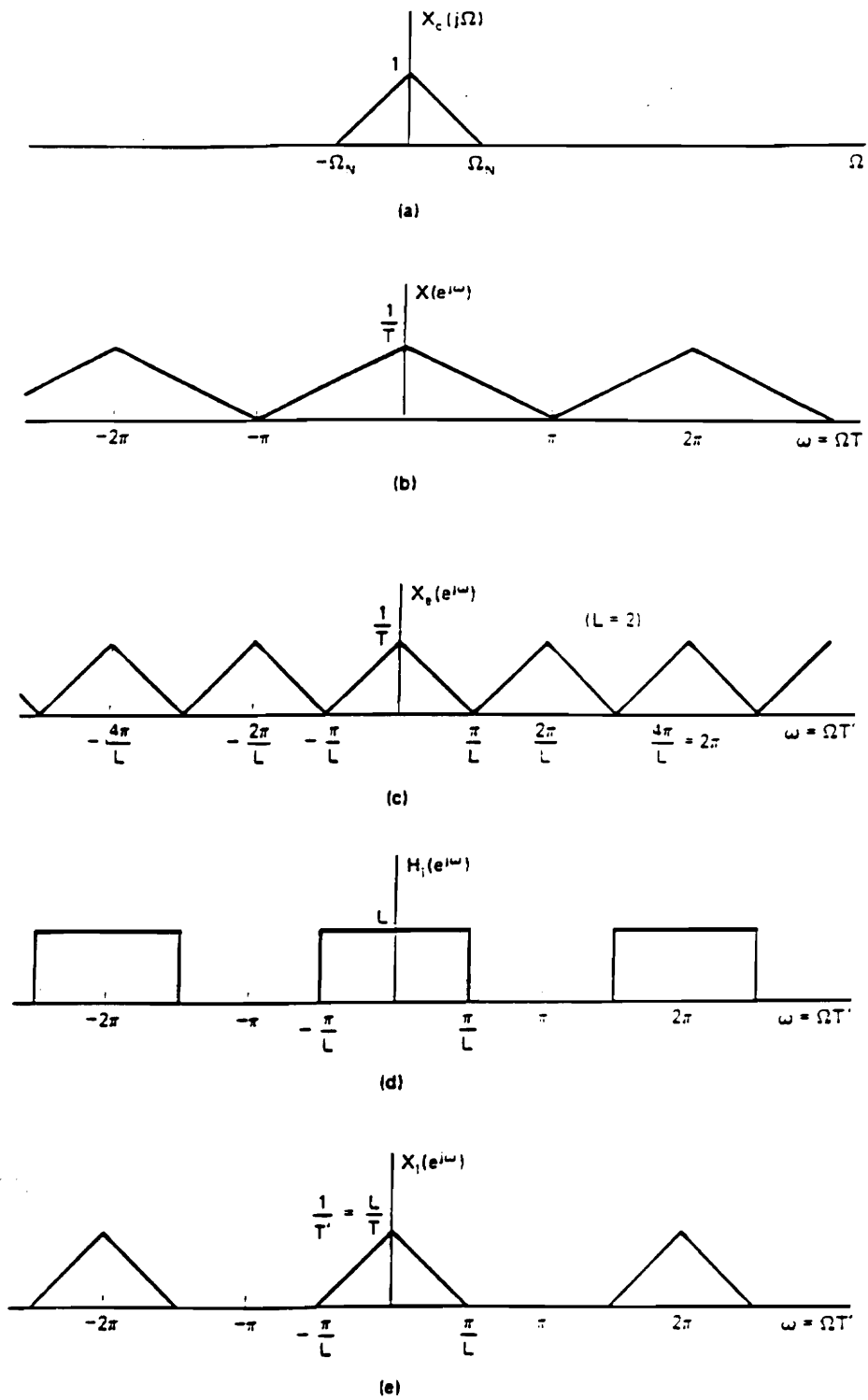


Figure 4.4 Frequency domain illustration of interpolation [25].

$$X_e(e^{j\omega}) = \sum_{k=-\infty}^{\infty} x[k]e^{-j\omega kL} = X(e^{j\omega L}). \quad (4.46)$$

Therefore, the Fourier transform of the expander output is a frequency scaled version of the Fourier transform of the expander input, i.e. in the horizontal axis, ω is replaced by ωL . We can obtain the spectrum, $X_i(e^{j\omega})$, of the interpolated signal from $X_e(e^{j\omega})$ by multiplying the amplitude scale by L and removing all the frequency scaled images of $X_e(j\Omega)$ except at integer multiples of 2π . This operation requires a low pass filter that operates at the new rate, ω_s' , with a gain of L and a cut off frequency of π/L [25]. The frequency response of such a filter is shown in Figure 4.4(d). Figure 4.4(e) shows the spectrum $X_i(e^{j\omega})$ of the interpolated output.

4.4.2.1 Filter Design and Practical Considerations

An important issue in signal reconstruction based on interpolation is the design of the low pass filter. Discrete-time filters can be broadly classified into two categories: 1) infinite impulse response (IIR) filters, and 2) finite impulse response (FIR) filters. Realizable IIR filters are characterized by [25]

$$y(n) = \sum_{k=0}^{\infty} h(k)x(n-k) = \sum_{k=0}^N a_k x(n-k) - \sum_{k=1}^M b_k y(n-k), \quad (4.47)$$

where $h(k)$ is the impulse response of the filter which is theoretically infinite in duration, a_k and b_k are the filter coefficients, and $x(n)$ and $y(n)$ are the input and output to the filter. In IIR filters the current output sample $y(n)$ is a function of past outputs, $y(n-k)$ as well as present and past input samples $x(n-k)$. Therefore, it is a feed back system. The basic FIR filter is characterized by [25]

$$y(n) = \sum_{k=0}^{N-1} h(k)x(n-k), \quad (4.48)$$

where $h(k)$, $k=0,1,\dots, N-1$, are the impulse response coefficients, N is the filter length, and $x(n)$ and $y(n)$ are defined as before. The filter order, M , is given by $M = N+1$. In the case of an FIR filter the current output sample is dependent only on the present and past input samples.

An IIR filter normally requires fewer coefficients than an FIR filter for meeting the same set of specifications. Therefore, IIR filters are usually used when sharp cut off and high throughput are important requirements. IIR filters can become unstable if they are not

designed properly. Also, the phase response of an IIR filter is non-linear. FIR filters, on the contrary, are always stable and are very simple to implement. The most significant advantage of FIR filters is that they have an exactly linear phase response. No phase distortion is introduced in the signal by the filter [25]. It will be shown in later discussion that the sensor output of an EFPI is a phase modulated signal. Therefore, it is necessary to perform the interpolation operation with an FIR filter. Moreover, this also results in a saving in multiplication by a factor of almost half [24].

The ideal low pass interpolation filter is a perfect brickwall filter. The magnitude frequency response of such a filter is shown in Figure 4.4(d). It has no ripples in the pass band, complete attenuation in the stop band, and a transition band of zero width. Unfortunately, real filters do not have such frequency responses. A typical low pass filter has a frequency response shown in Figure 4.5. It can be seen that real filters have ripples in the pass band and stop band, and a monotonically decreasing transition band of finite width in between. Comparing Figures 4.4(d) and 4.5 it is clear that if the original signal is sampled at just the Nyquist rate, interpolation will not be very good since the output of the real filter will contain considerable energy in the band $\pi/L < \omega \leq \pi$. Therefore, sampling just at the Nyquist rate will give rise to aliasing, which will result in a distorted output signal. However, if the finite width transition band is accounted for by choosing a sampling rate that is higher than the Nyquist rate, then interpolation will be more successful in removing the images of $X_c(j\Omega)$. In filter design, the fundamental tradeoff is choosing between the transition bandwidth and stop band attenuation. For the same filter order, a higher stop band attenuation also increases the transition bandwidth. If the filter order is increased, it will result in a greater delay in the output. This delay causes the output to contain unnecessary low frequency components. Moreover, the sampled discrete time wave form of the sensor output is a time-limited wave form. Thus, it is actually band-unlimited, and will contain some energy in the frequency band outside the calculated bandwidth of the signal. Thus, the FIR filter should be capable of meeting all of the following specifications:

- 1) It should have as narrow a transition bandwidth as possible. An increase in the transition bandwidth will result in an increase in the sampling rate.

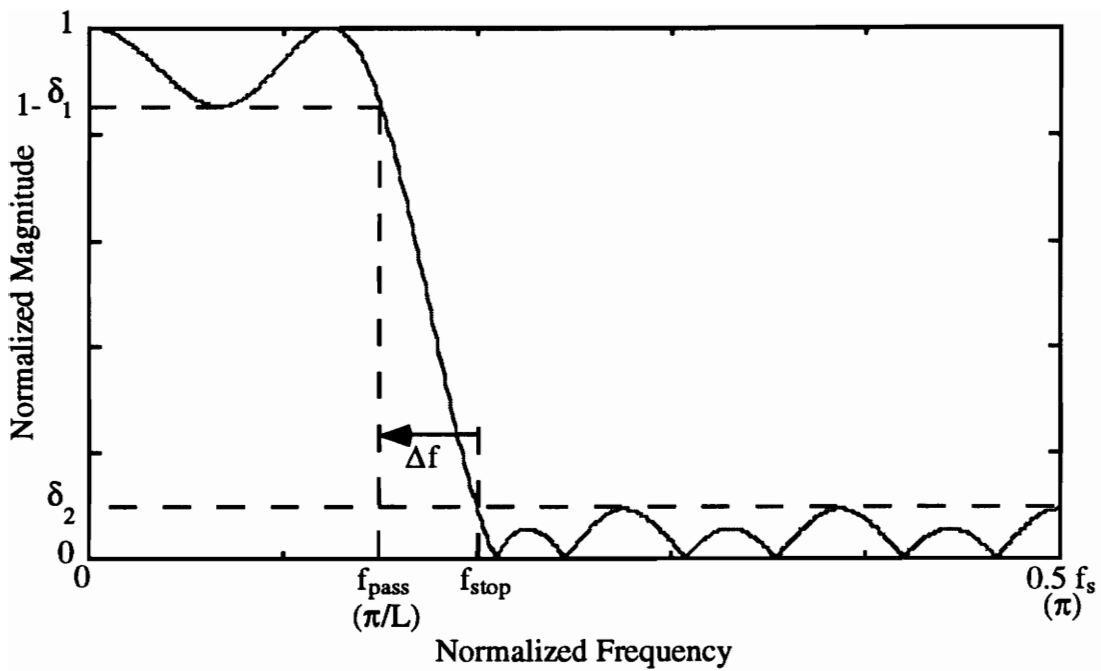


Figure 4.5 Frequency response of a typical low pass filter.

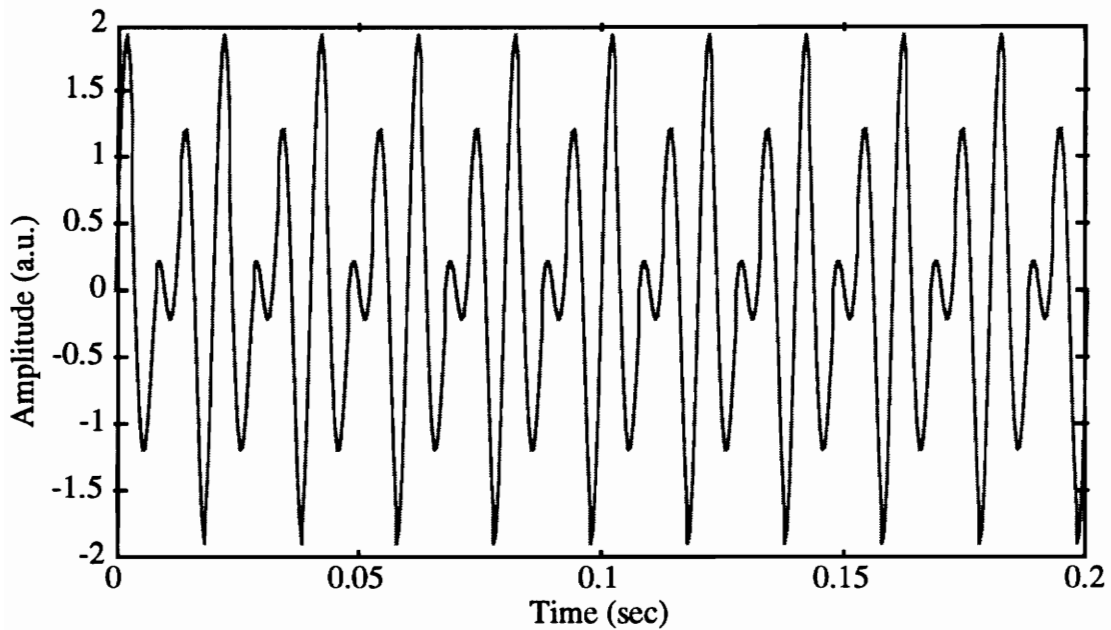


Figure 4.6 Oversampled signal with sinusoidal components of 100 Hz and 150 Hz.

- 2) It should have a stop band attenuation high enough to adequately suppress the frequency components of the sampled wave form which are outside the calculated bandwidth of the analog signal.
- 3) It should have a low enough order as possible so the output signal does not experience a significant delay.

FIR filters can be designed using mainly three approaches: 1) Window-based design, 2) Frequency Sampling design, and 3) Equiripple design. The equiripple design is an iterative computer optimization approach to FIR filter design. In the other techniques the transition region or band edges tend to have the peak ripples. The equiripple design evenly distributes the ripples between the pass and stop bands, and a better approximation of the desired frequency response can be achieved [27]. Therefore, this design technique has been selected to create the filters for interpolation. The Remez exchange algorithm in MATLAB was used to design the equiripple FIR filters. The initial filter order for the Remez algorithm can be found from the following expression [27]

$$M = \frac{-20\log_{10}(\delta_1\delta_2) - 13}{14.6 \Delta\omega}, \quad (4.49)$$

where δ_1 and δ_2 define the pass band and stop band ripples, and $\Delta\omega$ is the normalized transition bandwidth.

It is therefore possible to reconstruct a bandlimited analog signal through interpolation only if it sampled at a rate higher than the Nyquist rate. Even then, this technique offers a significant reduction in sampling rate than the scheme where the signal is recovered by directly plotting the DAQ samples. For example let us consider a signal that has two sinusoidal components, $f_1 = 100$ Hz and $f_2 = 150$ Hz. If we sample this signal at $f_s = 2400$ samples per second (sps), the sampled discrete-time signal looks like a replica of the continuous-time signal, as shown in Figure 4.6. Now let us sample the same wave form at a rate $f_s = 400$ sps which is greater than the Nyquist rate, but less than $f_s = 2400$. The sampled discrete-time wave form is illustrated in Figure 4.7. It is easily seen that this wave form looks very different from the one sampled at the higher rate. However, using interpolation techniques with $L = 6$, it can be seen in Figure 4.8 that the reconstructed wave form is very similar to the one that was obtained with $f_s = 2400$ sps. The frequency response of the low pass filter used for interpolation is shown in Figure 4.9.

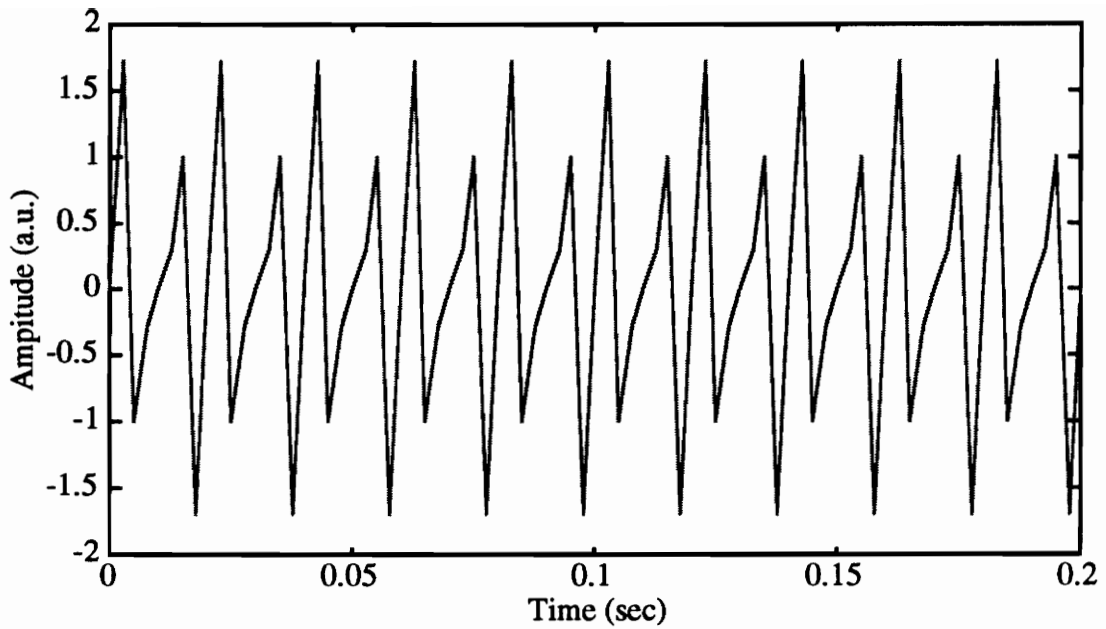


Figure 4.7 Discrete-time waveform of signal sampled at 400 sps.

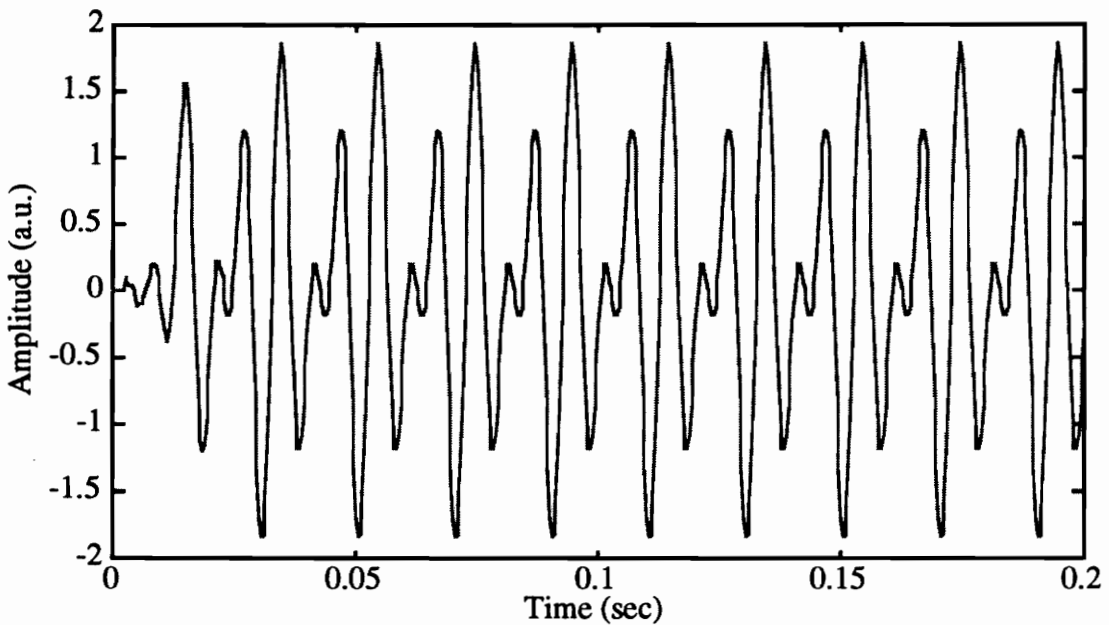


Figure 4.8 Reconstructed waveform of signal using an interpolation factor of 6.

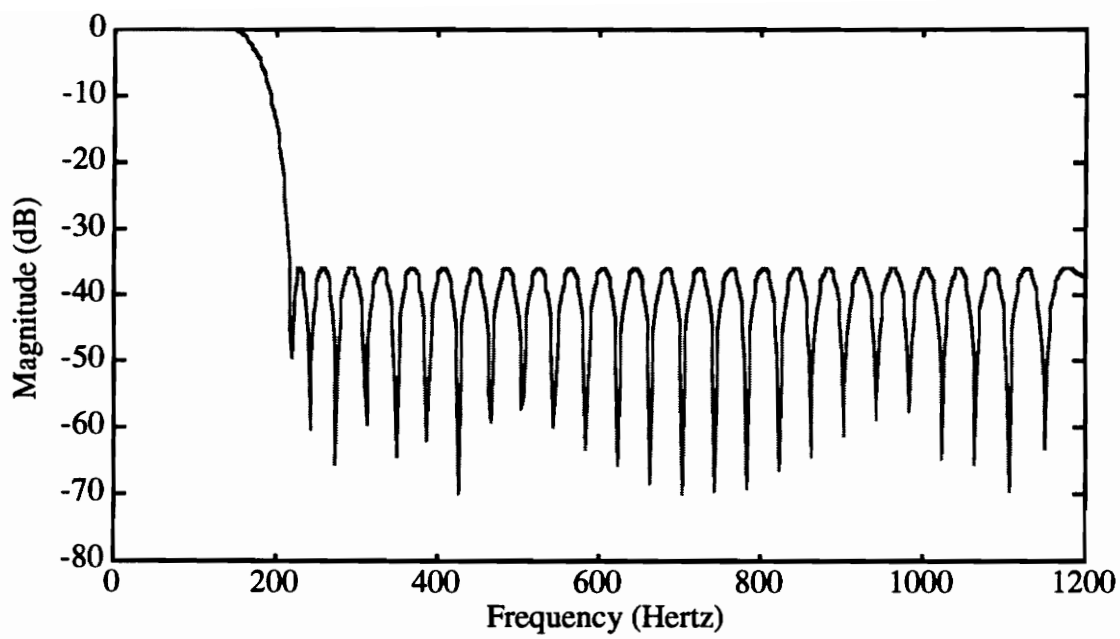


Figure 4.9 Frequency response of low pass filter used in interpolation example.

Since Equation (4.40) determines the relationship between the sampling rate and the bandwidth of a bandlimited signal, before a particular sampling rate can be chosen for a strain field, it is imperative to understand how that field governs the bandwidth of the analog output of the sensor. From Equation (2.11) we see that the strain field phase modulates the output intensity of an EFPI sensor. Thus, an understanding of Phase Modulation (PM) in communication systems gives as an insight into the modulation process involved in EFPI based sensing systems.

In communication systems, phase modulation results when the phase angle, ϕ , of the carrier is made a function of the modulating signal [27]. The unmodulated carrier is given by

$$e_c = \sin(\omega_c t + \phi_0), \quad (4.50)$$

where ω_c is the carrier frequency and ϕ_0 is a constant. When the phase of the carrier is linearly varied with an input signal $f(t)$, we can write[27]

$$\phi(t) = \omega_c t + kf(t) + \phi_0, \quad (4.51)$$

where k is the phase deviation constant.

For this analysis we shall consider a sinusoidal modulating wave form with amplitude a_m and an angular frequency ω_m . Then the expression for the phase modulated signal becomes

$$e = \sin(\omega_c t + ka_m \sin \omega_m t + \phi_0), \quad (4.52)$$

or,

$$e = \sin(\omega_c t + \Delta\phi \sin \omega_m t + \phi_0). \quad (4.53)$$

The quantity $\Delta\phi = ka_m$ is called the peak phase deviation. It is a measure of the change in phase due to the modulation process. The deviation in the phase also causes a deviation in the instantaneous frequency of the signal. The peak frequency deviation, $\Delta\omega$, is related to the peak phase deviation by [22]

$$\Delta\omega = (\Delta\phi)\omega_m. \quad (4.54)$$

Due to the deviation of the instantaneous frequency, the spectrum of a phase modulated carrier with a sinusoidal modulating signal broadens considerably. The spectrum is found to consist of a carrier component and an infinite number of side bands which are harmonics of the modulating frequency. The amplitudes of various spectral components are given by Bessel's Function of the First Kind [22]. We, however, can use Carson's rule

to compute the bandwidth of the signal. According to this rule, the bandwidth of the signal is given by

$$B \approx 2(\Delta f + f_m), \quad (4.55)$$

or,

$$B \approx 2f_m(1 + \Delta\phi), \quad (4.56)$$

where $\Delta f = \Delta\omega/2\pi$ and $f_m = \omega_m/2\pi$. The factor of 2 appears because the spectrum of the signal is double sided centered about the carrier frequency.

In practical systems, the modulating signal will not be a pure sinusoid, but will consist of numerous frequency components. However, we can still extend Carson's rule to that situation and compute the bandwidth of the signal using

$$B \approx 2F_m(1 + \Delta\phi_{\max}), \quad (4.57)$$

where F_m is the highest frequency component in the modulating signal, and $\Delta\phi_{\max}$ is the peak phase deviation due to F_m .

The previous analysis has now laid the groundwork for us to compute the bandwidth of the phase modulated analog output of an EFPI. The phase of the detected signal for an EFPI can be written as

$$\phi(t) = \frac{4\pi}{\lambda} d(t), \quad (4.58)$$

or,

$$\phi(t) = \frac{4\pi}{\lambda} d_{\text{bias}} + \frac{4\pi}{\lambda} \Delta d(t), \quad (4.59)$$

where $\Delta d(t)$ is the time varying change in cavity length induced by the strain field. Comparing Equations (4.51) and (4.58) we notice the only difference between the phase term in the EFPI output and the phase term in a phase modulated signal in a communication system is that the former lacks the carrier term $\omega_c t$. Let us assume that the modulating signal, in terms of gap length is

$$\Delta d(t) = a_m \sin \omega_m t. \quad (4.60)$$

For the dual laser system to work properly, the amplitude of the time varying gap cannot exceed Δd_{\max} . Therefore, it is obvious that the maximum phase deviation for any frequency component in the time varying gap length $\Delta d(t)$ is

$$\Delta\phi_{\max} = \frac{4\pi}{\lambda} \Delta d_{\max}. \quad (4.61)$$

If the maximum frequency component of $\Delta d(t)$ is F_m , it follows from Equations (4.56) and (4.61), the bandwidth occupied by the sensor signal is

$$B \approx F_m \left(1 + \frac{4\pi}{\lambda} \Delta d_{\max} \right). \quad (4.62)$$

The need to multiply the bandwidth by a factor 2 in Equation (4.62) is eliminated since unlike a communication signal, the sensor system does not have a carrier frequency (technically, the carrier is 0 Hz or DC).

Thus, the sampling rate (which is also the switching rate of the lasers) that need to be chosen for a modulating strain with the highest frequency component of F_m is

$$f_s > 2F_m \left(1 + \frac{4\pi}{\lambda} \Delta d_{\max} \right). \quad (4.63)$$

The system employs two LDs which are closely separated in wavelength. The sampling rate should be chosen based on the LD that emits the lower wavelength, since the bandwidth occupied by the sensor signal due to this wavelength is higher.

The strain function that causes a sinusoidal gap length variation with an amplitude of Δd_{\max} , of the Fabry-Perot cavity is given by,

$$\epsilon(t) = \frac{\Delta d_{\max}}{g} \sin \omega_m t. \quad (4.64)$$

The expression for the strain rate then becomes

$$\frac{d\epsilon(t)}{dt} = \frac{\Delta d_{\max}}{g} \omega_m \cos \omega_m t. \quad (4.65)$$

Therefore, the maximum strain rate that can be measured by the system that is being operated at a sampling rate, f_s , given by Equation (4.63) is

$$\epsilon_{\text{rate}} = \left(\frac{d\epsilon(t)}{dt} \right)_{\max} = \frac{2\pi \Delta d_{\max} F_m}{g}. \quad (4.66)$$

If we make the assumption that each fringe due to the highest strain rate is sampled $N' = f_s/B$ times, then the expression for strain resolution in the absence of noise is given by,

$$\epsilon_{\text{res}} = \frac{\lambda}{2LN'g}. \quad (4.67)$$

Therefore, if we also take the effect of noise into account, the expression for strain resolution becomes

$$\epsilon_{\text{res}} = \frac{\lambda}{2LN'g} + \frac{\left(\frac{\lambda}{2LN'g}\right)}{\text{SNR}} \quad (4.68)$$

Equation (4.68) shows that for a given maximum strain rate, an increase in the interpolation factor L results in an improved strain resolution. However, achieving this improved resolution also requires a low pass filter with a sharper cut off which may become very difficult to design.

Chapter 5 - Experimental Setup, Results and Discussion

In this chapter we describe the laboratory experiments conducted using the dual wavelength extrinsic Fabry-Perot Interferometer (EFPI) based strain sensing system and analyze the results.

The basic system setup is shown in Figure 5.1. The center wavelengths of transmitter 1 and transmitter 2 were 1291.9 and 1294.6 nm respectively. The output pin of the AT-MIO-16E-2 data acquisition card was fed into the input pin of each transmitter to provide the timing signal. The receiver output was split into two parallel signals using a T connector. Each signal was fed to an input pin of the data acquisition card. An RS 232 serial link was used to provide the interface between the 486-33 MHz PC and the AT-MIO-16E-2. The PC and the AT-MIO-16E-2 together make up the data acquisition system (DAQ). The EFPI sensor was bonded to a cantilever beam using Miller-Stephenson 907 epoxy. The sensor had a gage length of 11.1 mm and an initial gap of 50 μm .

As mentioned in previous chapters, the electronic hardware designed for this system can support a data acquisition rate of up to 100 kilo samples per second (ksps). However, at present due to the limitations of the data acquisition software, the system is capable of supporting a maximum acquisition rate of 15 ksps. Even at 15 ksps, the data file containing the sensor output became extremely large and slowed down the post processing of the sensor output considerably. Therefore, we limited the operation of the system to 5 ksps to facilitate the processing of the output data.

As an initial experiment, we set the acquisition rate at 5 ksps and applied an arbitrary strain on the beam by manually perturbing it. At first, the sensor output was observed on the computer monitor and then it was recorded on a data file. The raw sensor output for three different situations are shown in Figures 5.2, 5.3, and 5.4. Figure 5.2 illustrates the situation when the sensor output due to transmitter 1 ($\lambda = 1291.9$ nm) is ambiguous while the output due to transmitter 2 ($\lambda = 1294.6$ nm) displays a distinct turn around point. The reverse situation can be seen in Figure 5.3, where the output due to transmitter 1 shows a turn around point, while the output due to the other source is ambiguous. Figure 5.4 illustrates the case when the output from both sources clearly show the turn around point of the sensor. However, the previous figures are based on the raw output data from the sensor

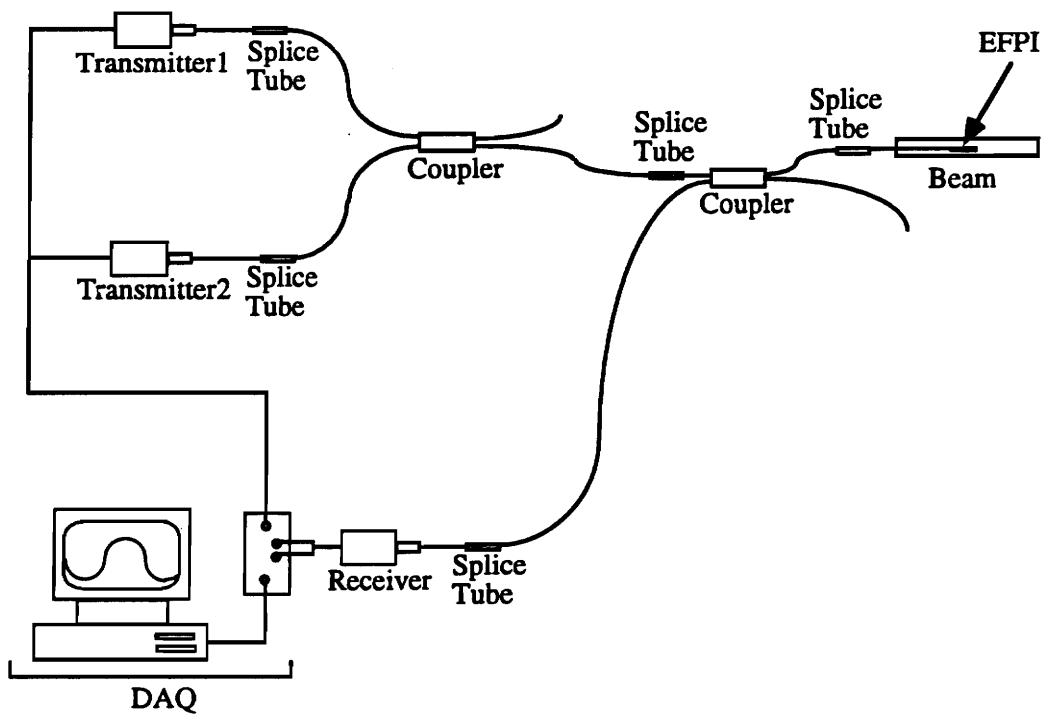


Figure 5.1 Experimental setup for dual wavelength EFPI sensing system.

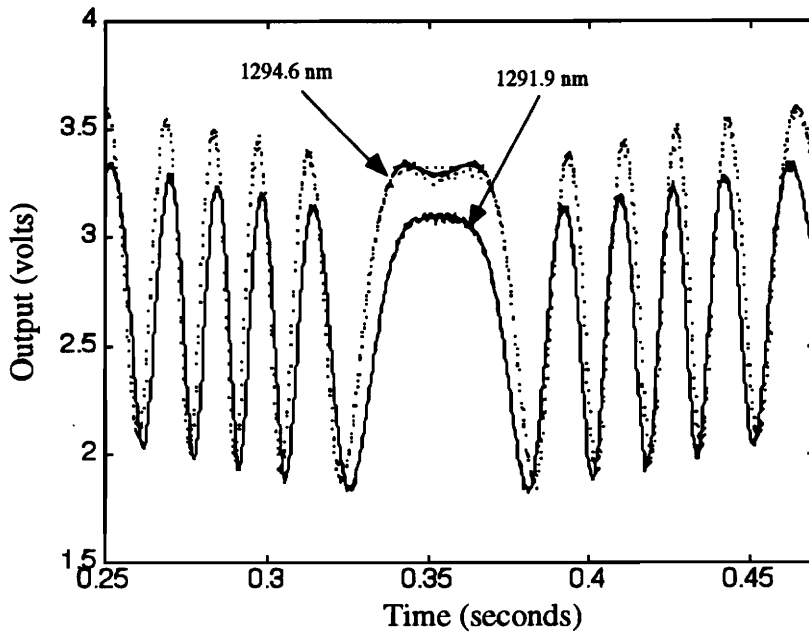


Figure 5.2 Raw sensor output with source at 1294.6 nm displaying distinct turn around point while source at 1291.9 nm showing ambiguity.

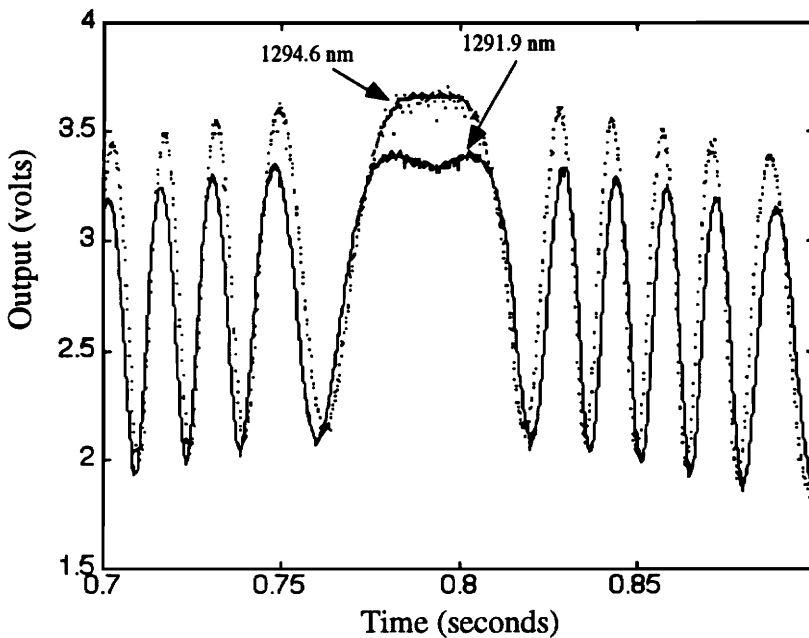


Figure 5.3 Raw sensor output with source at 1291.9 nm displaying distinct turn around point while source at 1294.6 nm showing ambiguity.

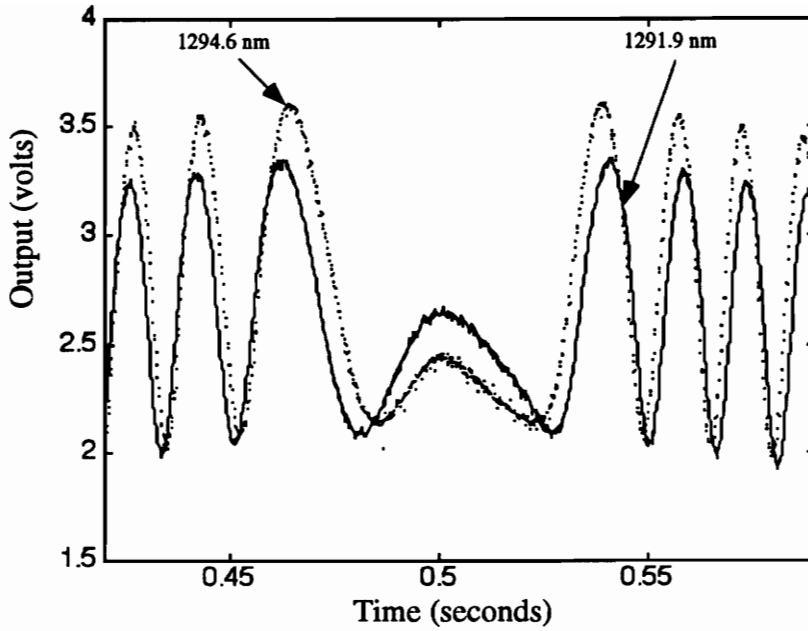


Figure 5.4 Raw sensor output with both sources displaying distinct turn around point.

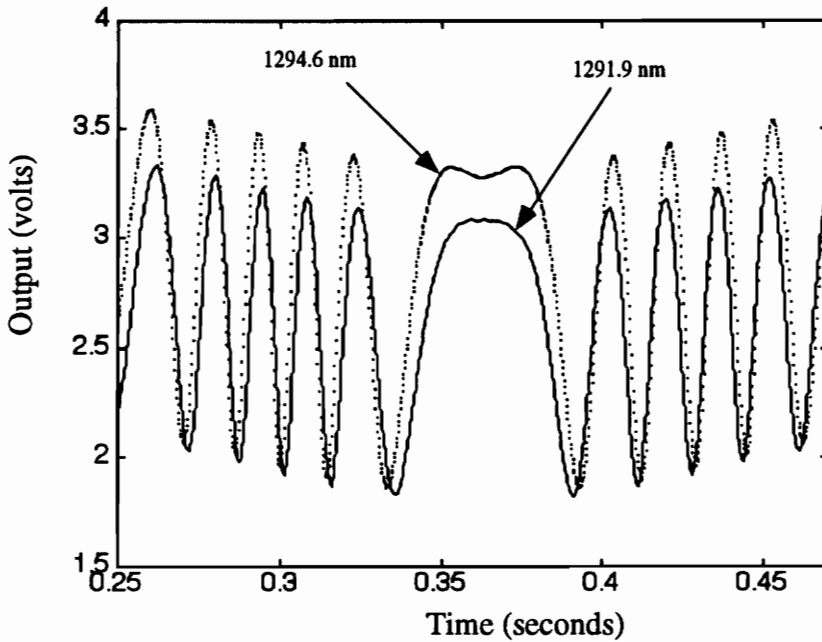


Figure 5.5 Filtered sensor output with source at 1294.6 nm displaying distinct turn around point while source at 1291.9 nm showing ambiguity.

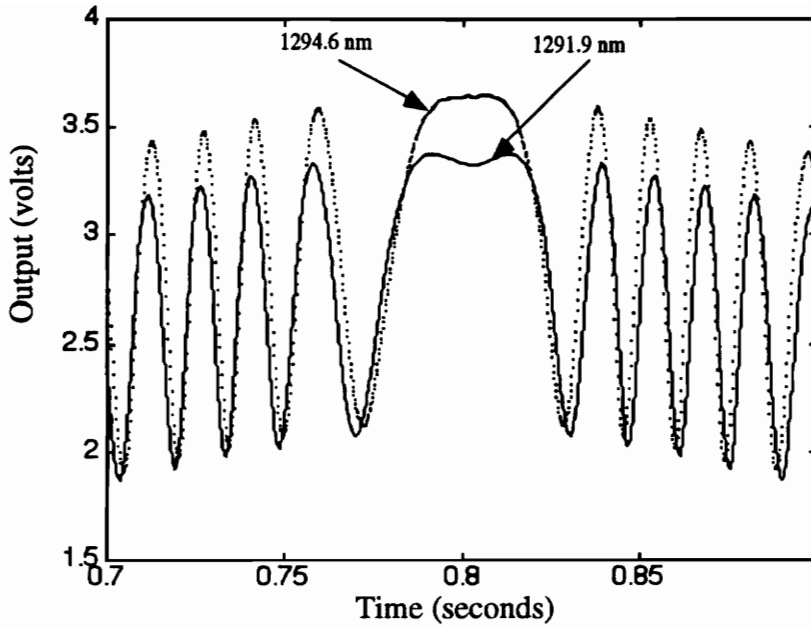


Figure 5.6 Filtered sensor output with source at 1291.9 nm displaying distinct turn around point while source at 1294.6 nm showing ambiguity.

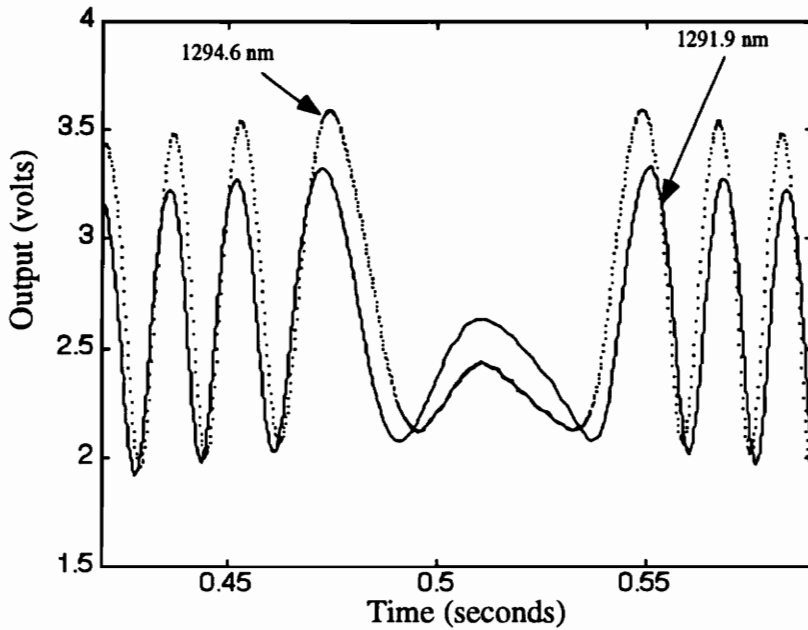


Figure 5.7 Filtered sensor output with both sources displaying distinct turn around point.

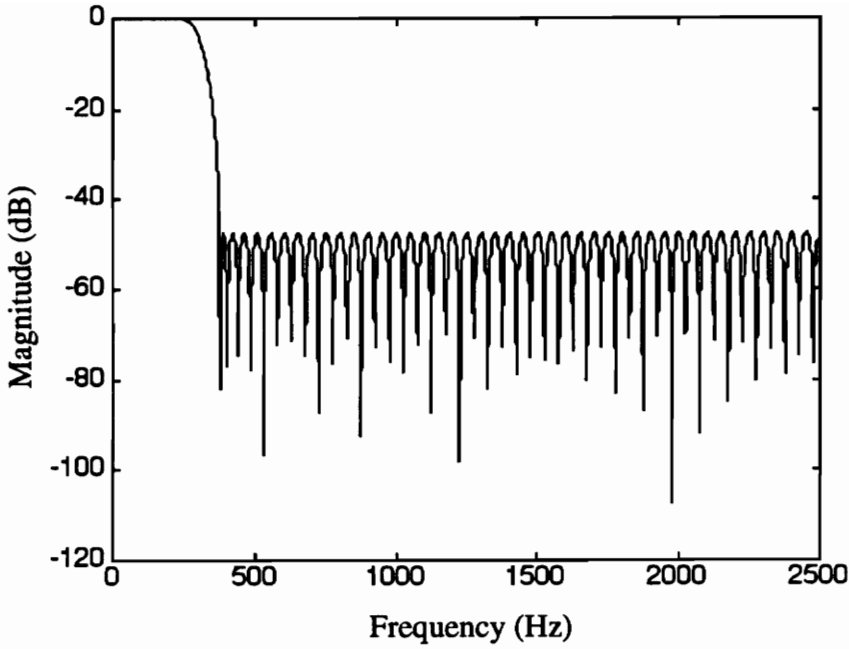


Figure 5.8 Frequency response of low pass filter used to filter the raw sensor output.

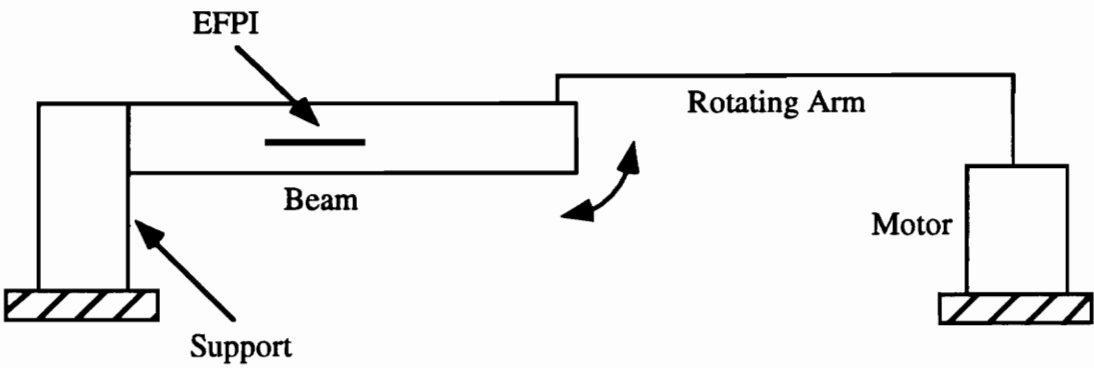


Figure 5.9 Schematic of the beam-motor mechanism.

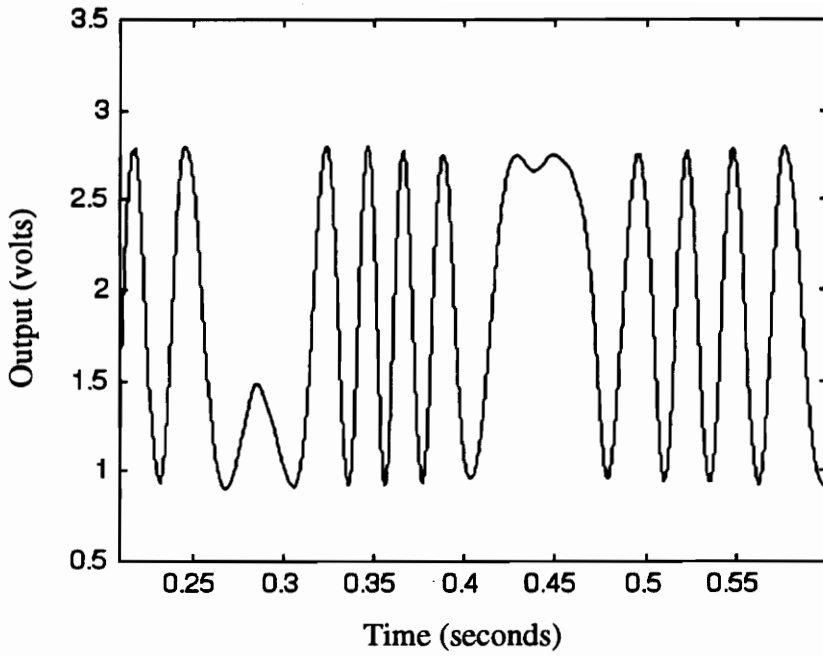


Figure 5.10 Filtered sensor output for the 1291.9 nm source in response to the applied sinusoidal strain function. The data acquisition rate is 2500 sps.

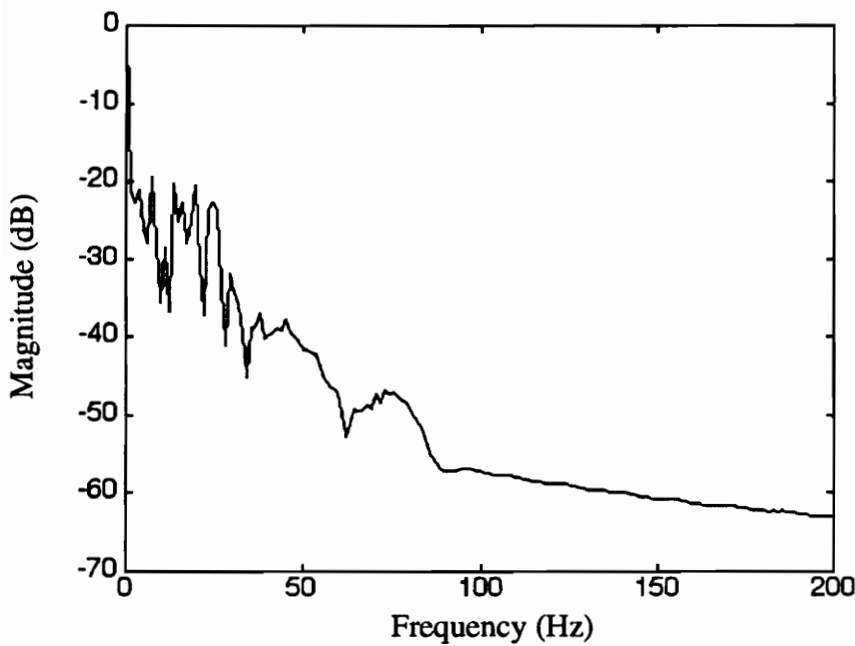


Figure 5.11 Spectrum of the sensor output signal for the 1291.9 nm source.

and appear to be quite noisy. The experimental signal-to-noise ratio (SNR) of the system was calculated to be around 28 dB. The experimental SNR is significantly different from the expected theoretical value of 42 dB calculated earlier. The degradation of the SNR of the system can be attributed to the fact that all the electronic circuits in the system were fabricated using breadboards, which are a major source of additional noise. We hope that the SNR of the system will improve considerably once the circuits are mounted on printed circuit boards. To get rid of the noise, we passed the raw sensor data through a hundredth order low pass filter with a cut off frequency of 250 Hz. The filter was generated in MATLAB using the REMEZ algorithm. Figures 5.5, 5.6, and 5.7 are the filtered versions of the sensor outputs shown in Figures 5.2, 5.3, and 5.4 respectively. The directional changes of the sensor became more distinct after the output is passed through the filter. Figure 5.8 shows the frequency response of the low pass filter.

In the previous experiment we reconstructed the sensor output directly from the samples acquired by the data acquisition system. Our next objective was to prove that by reducing the sampling rate and employing interpolation techniques, we could increase the maximum measurable strain rate of the system. To compare the actual strain rate applied on the beam, and the derived theoretical expression given by Equation (4.66), it was necessary to perturb the beam with a known strain function. We used a motor with a rotating arm to apply a sinusoidal strain on the beam. The rotating arm was attached to the tip of the beam, and the frequency of operation could be controlled by changing the drive voltage of the motor. The beam-motor mechanism is shown in Figure 5.9. We set the drive voltage of the motor at 36 V. At this drive voltage, the frequency of operation was measured to be slightly over 3 Hz.

At first, the sensor output was acquired at 2.5 ksps. Figure 5.10 shows the acquired data for $\lambda = 1291.9$ nm after it was passed through a low pass filter. To calculate the experimental strain rate we measured the elapsed time between a successive peak and trough in the fringe pattern, knowing that the sensor gap length changes by a quarter wavelength or 323 nm within this time period. The elapsed time was measured to be about 0.0135 seconds. Thus, the applied strain rate was calculated to be around 2.2×10^6 $\mu\epsilon/s$. By measuring the number of fringes between two successive turn around points we calculated the maximum gap displacement of the sensor in either direction from the bias point to be

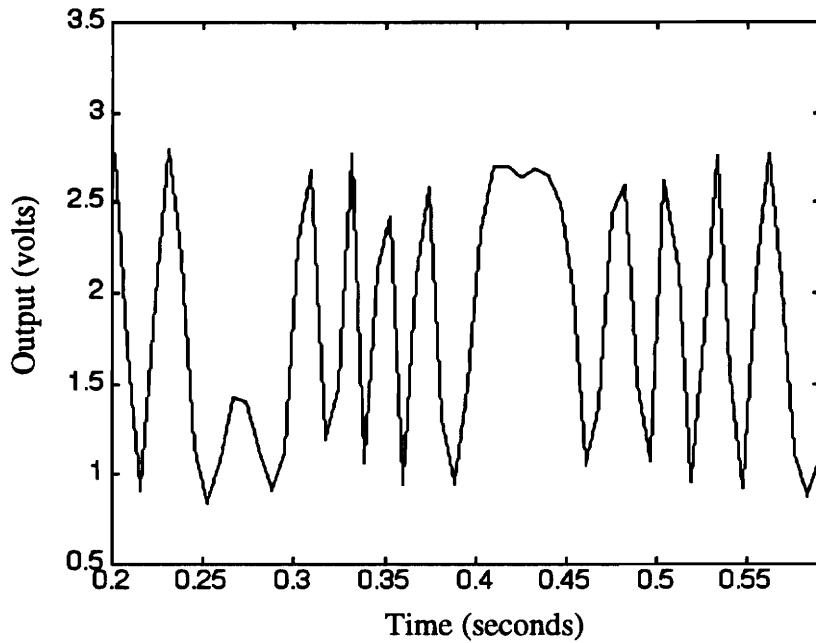


Figure 5.12 Sensor output for the 1291.9 nm source in response to the applied sinusoidal strain function. The data acquisition rate is 140 sps.

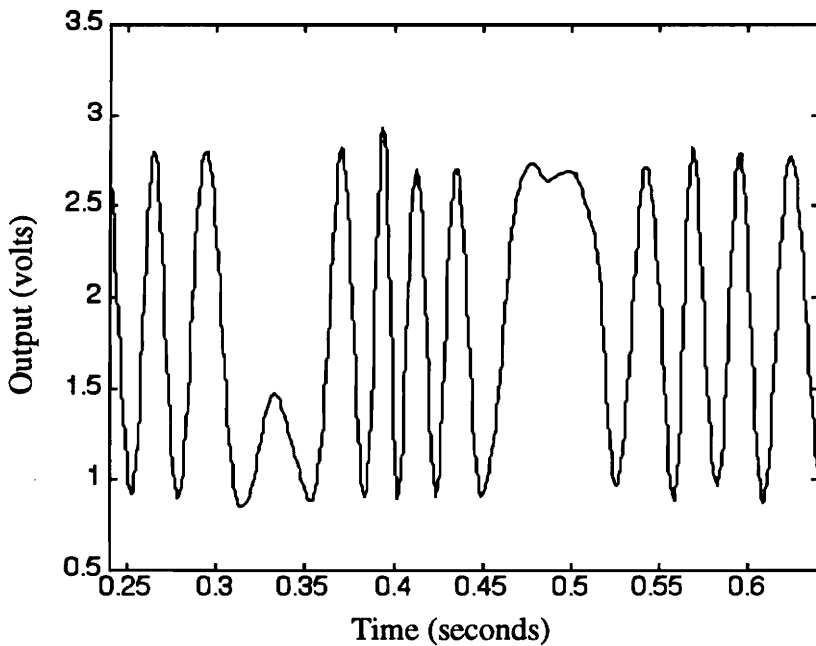


Figure 5.13 Reconstructed sensor output using interpolation with $L = 8$ for 1291.9 nm source. Actual data acquisition rate is 140 sps.

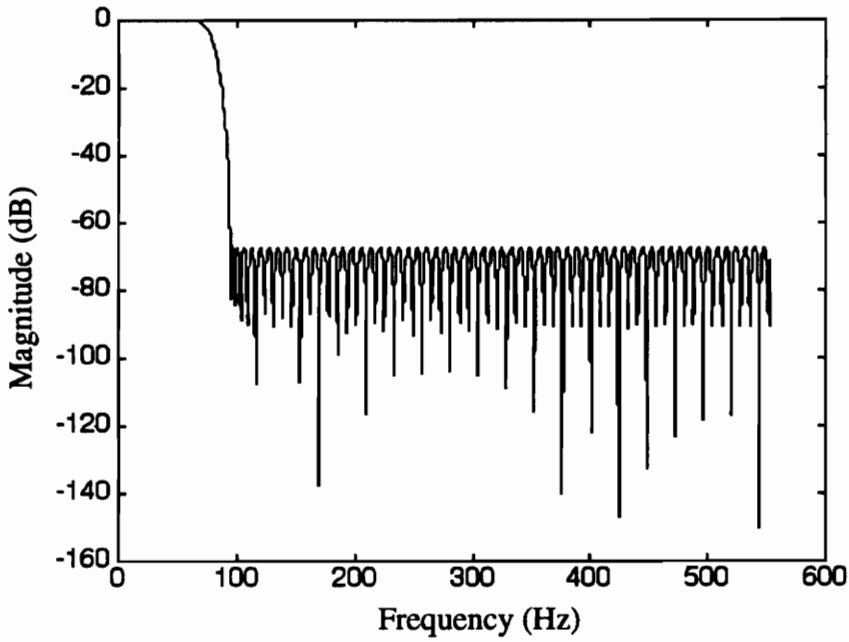


Figure 5.14 Frequency response of low pass filter used for interpolation.

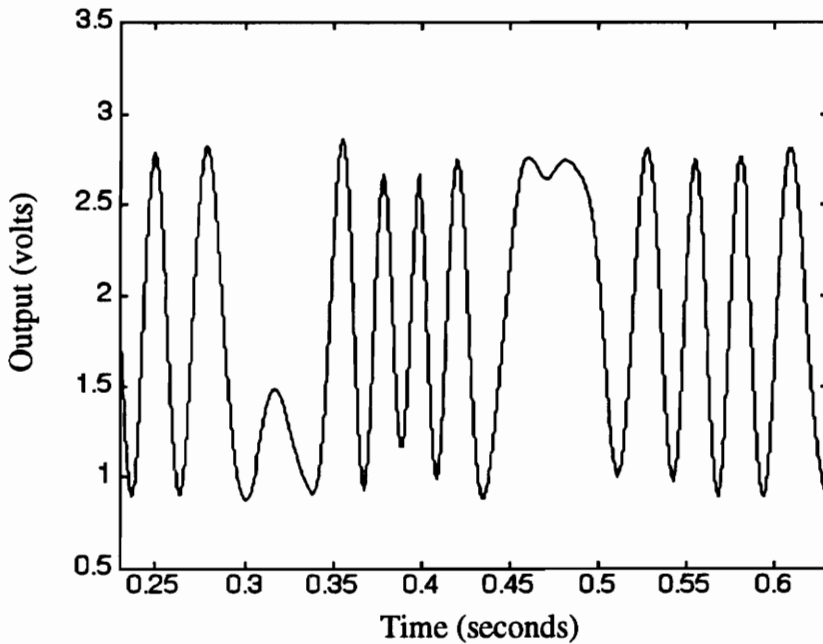


Figure 5.15 Filtered sensor output for 1291.9 nm source in response to sinusoidal strain function. Data acquisition rate is 833 sps.

1.53 μm . Using Equation (4.66), the theoretical strain rate was calculated to be 2.6×10^6 $\mu\text{E/s}$. The spectrum of the output signal can be seen in Figure 5.11. The bandwidth of the signal must be known to apply interpolation techniques and reconstruct the output signal using low acquisition rates. The bandwidth of the output signal was calculated to be around 50 Hz based on Equation (4.62). Thus, to properly apply the interpolation technique the acquisition rate had to be greater than 100 sps. We used different sampling rates above 100 sps and different interpolation factors to find the lowest acquisition rate that gives a satisfactory reconstruction of the oversampled output signal. For a sampling rate of 140 sps and interpolation factor of $L = 8$, the correlation between the reconstructed output and the oversampled output was very satisfactory. Figure 5.12 shows the output signal at 140 sps reconstructed by directly plotting the DAQ samples, while the interpolated output signal is shown in Figure 5.13. It can be seen that while the signal obtained by directly plotting the DAQ samples is extremely distorted than the oversampled signal, the interpolated reconstruction is very similar. The frequency response of the discrete-time low pass filter used in the interpolation method is shown in Figure 5.14.

According to Equation (4.67), the strain resolution of the system for an acquisition rate of 140 sps and interpolation factor of 8 is 2.6 μE . Let us now consider reconstructing the output signal directly from the DAQ samples. Using Equations (4.37) and (4.38), it can be shown that we need to acquire data at a rate of 1000 sps to achieve a similar resolution. Figure 5.15 illustrates the sensor output recovered by directly plotting the DAQ samples at an acquisition rate of 833 sps. Comparing Figures (5.13) and (5.15), it can be seen that the signal reconstructed through interpolation has a better resolution, although the acquisition rate is nearly six times smaller. Thus, the method of interpolation significantly improves the strain rate measurement capability of the system without compromising strain resolution.

Chapter 6 - Conclusions and Future Directions

In this thesis, we successfully demonstrated how dual wavelength interferometry can be used to overcome the directional ambiguity of the extrinsic Fabry-Perot interferometer (EFPI). The design and implementation of a dual wavelength EFPI strain sensing system has been presented. The system relies on alternately pulse modulating two laser diodes which are closely spaced in wavelength. The strain rate measurement capability of the system was significantly improved by employing digital signal processing techniques. The present system is capable of interrogating the Fabry-Perot cavity and acquiring data at a rate of 15 kHz. This rate can be extended to 100 kHz with further modifications of the data acquisition software.

At present, we have to rely on visually inspecting the output fringe pattern to detect turn around points, manually counting the number of fringes, and post processing the sensor output to convert the acquired data into useful strain information. At present, the system cannot be used for real time strain measurements due to the lack of real time fringe counting and phase detection algorithms. Therefore, any future work on the system must entail developing these algorithms.

References

1. E. Udd, Fiber Optic Sensors: An introduction for Engineers and Scientists, John Wiley and Sons, NY, 1991.
2. J. Dakin and B. Culshaw, Optical Fiber Sensors: Principles and Components, Artech House, MA, 1988.
3. V. Bhatia, "Signal processing techniques for optical fiber sensors using white light interferometry," *Master's Thesis*, Virginia Polytechnic Institute and State University, Blacksburg, VA, 1993.
4. R. Dhawan, "The split-cavity cross-coupled extrinsic fiber interferometer," *Master's Thesis*, Virginia Polytechnic Institute and State University, Blacksburg, VA, 1994.
5. R. O. Claus, M.F. Gunther, A. Wang, and K.A. Murphy, "Extrinsic Fabry-Perot sensor for strain and crack opening displacement measurements from -200 to 900 °C," *Smart Materials and Structures*, vol. 1, pp. 237-242, 1992.
6. C. Koob, "High temperature fiber optic strain sensing," *Master's Thesis*, Virginia Polytechnic Institute and State University, Blacksburg, VA, 1991.
7. M. Born and E. Wolf, Principles of Optics, Pergamon Press, NY 1985.
8. J. Sanderson, "Epoxy matrix composite strain sensing and cure monitoring," *Master's Thesis*, Virginia Polytechnic Institute and State University, Blacksburg, VA, 1994.
9. J. L. Santos, A.P. Leite, and D.A. Jackson, "Optical fiber sensing with a low-finesse Fabry-Perot cavity," *Applied Optics*, vol. 31, pp. 7361, 1992.
10. K. A. Murphy, M.F. Gunther, A. M. Vengsarkar, and R.O. Claus, "Quadrature phase-shifted, extrinsic Fabry Perot optical fiber sensors," *Optics Letters*, vol. 16, pp. 273-275, 1991.

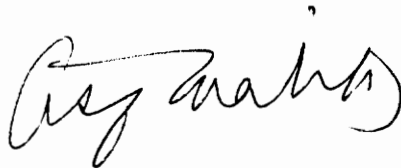
11. P. M. Schindler, "Corrosion detection using metal coatings on fiber optic sensors," *Master's Thesis*, Virginia Polytechnic Institute and State University, Blacksburg, VA, 1995.
12. M. Johnson, "White light interferometry," *Proceedings of the SPIE Conference on Fiber Optics.*, vol. 1314, pp. 307-314, September 1990.
13. B. R. Fogg, A. Wang, M. S. Miller, K. A. Murphy, and R. O. Claus, "Optical Fiber Sensor for absolute measurement," *FEORC Fiber Optics Review Conference*, Blacksburg, VA, 1992.
14. Y. Ishii and R. Onodera, "Two-wavelength laser-diode interferometry that uses phase-shifting techniques," *Optics Letters*, vol. 16, no. 19, pp. 1523-1525, 1991.
15. D. N. Wang *et al.*, "Characteristics of synthesized light sources for white-light interferometric systemd," *Optics Letters*, vol. 18, no. 22, pp. 1884-1886, 1991.
16. A. D. Kersey and A. Dandridge, "Two-wavelength interferometric fiber temperature sensor," *Proc. OFC'87*, Reno, NV, January 1987.
17. L. W. Couch II, Digital and Analog Communication Systems, Macmillan Publishing Company, 1992.
18. Acknowledgements to Paul Duncan and Shah Musa.
19. G. P. Agrawal, Fiber Optic Communications Systems, Wiley Series in Microwave and Optical Engineering, 1992.
20. Class Notes, EE 5984, Professor Ira Jacobs, Fall 1993.
21. K. C. Ravikumar, "Spread spectrum techniques for Distributed multimeasurand optical fiber sensors," *Master's Thesis*, Virginia Polytechnic Institute and State University, Blacksburg, VA, 1993.

22. F. G. Stremler, Introduction to Communication Systems, Addison-Wesley Publishing Company, 1990.
23. A. J. Plante, "Photoinduced fresnel reflectors in germanium-doped optical fibers," *Master's Thesis*, Virginia Polytechnic Institute and State University, Blacksburg, VA, 1994.
24. L. B. Jackson, Digital Filters and Signal Processing, Kluwer Academic Publishers, MA, 1993.
25. A. V. Oppenheim and R. W. Schafer, Discrete-Time Signal Processing, Prentice Hall, NJ, 1989.
26. Class Notes, EE 4624, Professor J. H. Reed, Fall 1994.
27. D. Roddy and J. Coolen, Electronic Communications, Prentice Hall of India, New Delhi, 1989.

Vita

Asif Malik was born in Dhaka, Bangladesh on July 7, 1970. He earned a Bachelor of Science degree in Electrical Engineering from Virginia Tech, Blacksburg, VA in May 1993. In July 1993, he joined the Fiber & Electro-Optics Research Center at Virginia Tech as a Graduate Research Assistant. He earned his Master of Science degree in Electrical Engineering from Virginia Tech in April 1996.

Asif Malik is currently working for Ericsson Inc. in Lynchburg, VA.

A handwritten signature in black ink, appearing to read "Asif Malik". The signature is written in a cursive style with a prominent loop at the end.